PERIDYNAMIC MODELING OF HYPERELASTIC MATERIALS

by

Dongjun Bang

_____

A Dissertation Submitted to the Faculty of the

DEPARTMENT OF AEROSPACE AND MECHANICAL ENGINEERING

In Partial Fulfillment of the Requirements
For the Degree of

DOCTOR OF PHILOSOPHY

WITH A MAJOR IN MECHANICAL ENGINEERING

In the Graduate College

THE UNIVERSITY OF ARIZONA

2016

THE UNIVERSITY OF ARIZONA
GRADUATE COLLEGE

As members of the Dissertation Committee, we certify that we have read the dissertation prepared by Dongjun Bang, titled Peridynamic Modeling of Hyperelastic Materials and recommend that it be accepted as fulfilling the dissertation requirement for the Degree of Doctor of Philosophy.

_____ Date: 12/02/2015
Erdogan Madenci

_____ Date: 12/02/2015
Samy Missoum

_____ Date: 12/02/2015
Xiaoyi Wu

_____ Date: 12/02/2015
George N. Frantziskonis

Final approval and acceptance of this dissertation is contingent upon the candidate's submission of the final copies of the dissertation to the Graduate College.

I hereby certify that I have read this dissertation prepared under my direction and recommend that it be accepted as fulfilling the dissertation requirement.

_____ Date: 12/02/2015
Dissertation Director: Erdogan Madenci

STATEMENT BY AUTHOR

This dissertation has been submitted in partial fulfillment of the requirements for an advanced degree at the University of Arizona and is deposited in the University Library to be made available to borrowers under rules of the Library.

Brief quotations from this dissertation are allowable without special permission, provided that an accurate acknowledgement of the source is made. Requests for permission for extended quotation from or reproduction of this manuscript in whole or in part may be granted by the head of the major department or the Dean of the Graduate College when in his or her judgment the proposed use of the material is in the interests of scholarship. In all other instances, however, permission must be obtained from the author.

SIGNED: Dongjun Bang

ACKNOWLEGEMENTS

DEDICATION

Dedicated to my mother, Bonghwa An

TABLE OF CONTENTS

TABLE OF CONTENTS – Continued

LIST OF FIGURES

LIST OF FIGURES – Continued

LIST OF FIGURES – Continued

LIST OF FIGURES – Continued

LIST OF FIGURES – Continued

LIST OF FIGURES – Continued

LIST OF FIGURES – Continued

LIST OF FIGURES – Continued

ABSTRACT

This study concerns the development of the peridynamic strain energy density function for a Neo-Hookean type membrane under equibiaxial, planar and uniaxial loading conditions. The material parameters for each loading case are determined by equating the peridynamic strain energy to those of the classical continuum mechanics. Therefore, the peridynamic equations of motion are derived based on the Neo-Hookean model under the assumption of incompressibility. Numerical results concern the deformation of a membrane without and with a defect in the form of a hole, an inclusion and a crack under equibiaxial, planar and uniaxial loading conditions. As part of the verification process, the peridynamic predictions are compared with those of finite element analysis. For all defect types and loading conditions, the comparisons indicate excellent agreement.

1. INTRODUCTION

Rubbery type materials are used commonly in many engineering applications because of their resilience, toughness, isotropy and elasticity. Such applications range from tires, engine mountings, vibration isolators, medical devices and structural bearings. However, they present nonlinear elastic behavior; thus, the deformation analysis become rather complex. Many hyperelastic material models were developed to describe the behavior of rubbery materials. For elastic and isotropic rubbery materials, these material models are expressed by the strain energy density function in terms of strain invariants I_i ($i = 1, 2, 3$). The first mathematical model to describe the large deformation of rubber was introduced by Mooney [1]. This model suitable for hyperelastic deformation under the assumption of incompressibility was expressed by Rivlin [2] as

$$W = C_1 (I_1 - 3) + C_2 (I_2 - 3), \tag{1}$$

where C_1, C_2 are the material constant. This Mooney-Rivlin material model uses only linear functions of the strain invariants. Also, it recovers the Neo-Hookean model introduced by Treloar [3] by retaining only the first invariant as

$$W = C_1 (I_1 - 3), \tag{2}$$

where C_1 is the material constant. In order to achieve better accuracy in the presence of very large strains, Ogden [4] and Yeoh [5] proposed their own models in the form of power series. Ogden model is expressed in terms of the principal stretches, λ_i ($i = 1, 2, 3$) as

$$W = \sum_{i=1}^{N} \frac{\mu_i}{\alpha_i} \left(\lambda_1^{\alpha_i} + \lambda_2^{\alpha_i} + \lambda_3^{\alpha_i} - 3 \right), \tag{3}$$

where N, μ_i and α_i are the material constants. Yeoh model can be considered as a general form of the Mooney-Rivlin model. It includes the third strain invariant in the form

$$W = \sum_{i=1}^{3} C_i \left(I_1 - 3 \right)^i, \tag{4}$$

where C_i are the material constants. Among the molecular models, Arruda and Boyce [6] suggested the eight-chain model retaining two molecular material parameters as

$$W = \mu \left[\begin{array}{c} \dfrac{1}{2}(I_1 - 3) + \dfrac{1}{20\lambda_L^2}\left(I_1^2 - 9\right) + \dfrac{11}{1050\lambda_L^4}\left(I_1^3 - 27\right) \\[3mm] + \dfrac{19}{7000\lambda_L^6}\left(I_1^4 - 81\right) + \dfrac{519}{673750\lambda_L^8}\left(I_1^5 - 243\right) \end{array} \right] \tag{5}$$

where μ is the initial shear modulus of material, λ_L is limiting network stretch. As the parameter λ_L goes to infinity, this model is identical to the Neo-Hookean model. Gent [7]

proposed a model containing a singular behavior; it is described by the first invariant only in the form

$$W = -\frac{\mu J_m}{2} \ln\left(1 - \frac{I_1 - 3}{J_m}\right),$$ (6)

where μ is the shear modulus, and J_m is the constant limiting value for $I_1 - 3$. This model recovers the Neo-Hookean model when the variable J_m in the denominator goes to infinity. Recently, Amin [8] proposed another model for natural rubber and high damping rubber. It is expressed in terms of the first invariant as

$$W = C_5\left(I_1 - 3\right) + \frac{C_3}{N+1}\left(I_1 - 3\right)^{N+1} + \frac{C_4}{M+1}\left(I_1 - 3\right)^{M+1},$$ (7)

where C_3, C_4, C_5, M and N are the material parameters.

All of these models require material constants that are measured by performing simple tests such as the equibiaxial tension, uniaxial tension and pure shear [11]. Among these material models, the most commonly used one is the Mooney-Rivlin model. Although this model is based on a simple form of strain energy density, its simplicity makes it convenient to utilize. However, it does not show consistent deformations for different loadings. Therefore, it requires additional approaches such as interpolation method. The Neo-Hookean model designed by Treloar [3], whose mathematical form is analogous to that of

an ideal gas. This model can be used to represent the Helmholtz free energy of a molecular network with Gaussian chain-length distribution. An advantage of the Ogden model is that it can be efficiently fitted to nonlinear material behavior because many sets of experimental date are used for the determination of material constants, and its form contains exponential parameters. The Mooney-Rivlin and the Ogden model make use of different material constants for tension and compression. However, the Arruda-Boyce model uses only one material coefficient. Although each of these models presents a particular advantage, Yeoh model provides the best agreement with experimental results as shown in Fig. 1.1.
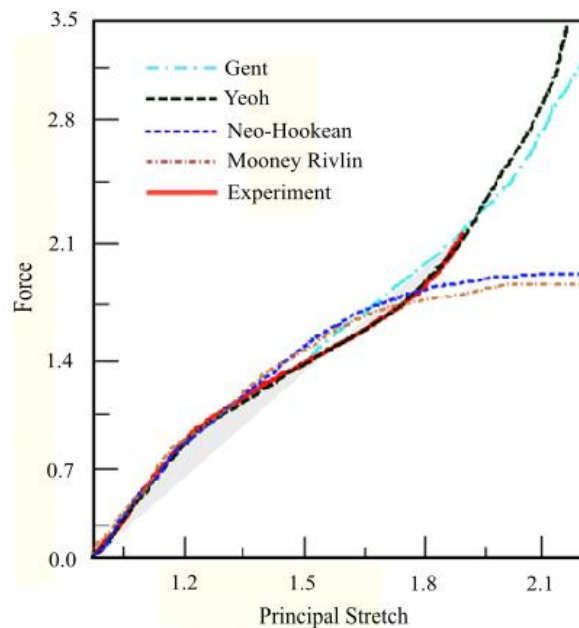
Figure 1.1. Comparison of hyperelastic material models to experimental measurement

Consequently, all of these models are available in the commercially available programs of the Finite Element Analysis (FEA) such as ABAQUS and ANSYS to predict the behavior of components of rubber-like materials. By performing FEA, Podnos et al. [9] investigated

the deformation of silicone rubber prosthesis for the metacarpophalangeal joint of hand. They selected and calibrated the material model by incorporating the test data. Montella et al. [10] examined the large deformations of a Tire Derived Material. They employed four classical hyperelastic models in the FEA of the railway track mat. Duncan et al. [11] evaluated usability of several hyperelastic material models and input data to obtain the force-extension response of lap joint bonded with a flexible adhesive. They modelled the lap joint specimen by using FEA to predict the force-extension response, and compared them to the experimental results. Vavourakis et al. [12] presented a procedure for the simulation of complex biological muscular motion such as the octupus arm bending at several different conditions. They validated the FEA model by comparing the results with experimental data for the squid arm extension. Gagnon et al. [13] simulated the behavior of a carbon black rubber at less than 25% engineering strain. They simplified the data obtained from experiments by assuming a perfectly elastic material, and they fitted them to hyperelastic models in the FEA. Also, Samad et al. [14] made an attempt to predict the fatigue life of the rubber components for the car jounce bumper. They performed a FEA to obtain the parameters which are required to predict cyclic loading. Ramachandran et al. [15] investigated the prediction of deformations of the engine mount with FEA. They determined the design variables of the mount element properties by optimizing the geometry of the structural components, and they simulated the rubber mounting with the FEA. Guo and Sluys [16] also simulated the rubber-like materials by utilizing the FEA. To simulate the ideal Mullins effect, they used both the concept of a continuum damage mechanics and a pseudo-elastic law. They verified the constitutive models by comparing the results with the experimental data. Kyriacou et al. [17] obtained axisymmetric and non-

axisymmetric solutions of the finite deformations of nonlinear orthotropic membranes by using the FEA. To validate their approach, they compared the numerical results to analytical solutions of two boundary value problems. Daly et al. [18] investigated the hyperelastic behavior of the cardiovascular tissue. They made use of Mooney-Rivlin model to simulate the anisotropic nonlinear elasticity of vessel under high strains.

Although these FEA analyses provide the deformation of response of rubber-like materials very accurately, the predictions with the traditional elements become more challenging in the presence of cracks or defects. To overcome this shortcoming, several approaches were proposed. In particular, the eXtended Finite Element Method (XFEM) can be applied to address crack growth [19-20]. However, the element distortion and appearance of singularities in the isoparametric mapping of the element cause numerical difficulties for large deformations. Therefore, the arbitrary Lagrangian-Eulerian (ALE) finite element formulation was introduced [21-26]. With this method, the element shapes for large deformations can be optimized by arbitrarily moving the mesh inside of the material and moving the mesh along the material on the boundaries and interfaces. Also, the meshless FEM was introduced [27-30] to remove excessive element distortion. In addition, the fine mesh and remeshing are utilized to investigate discontinuities experiencing large deformations [31-36].

Even with those approaches, the fundamental problem cannot be resolved. A different analysis approach is necessary for each case. Therefore, Silling [37] introduced the Peridynamic theory to address failure prediction in a unified manner. The significant

characteristics of the peridynamics (PD) is that it is formulated based on the integral equation. Since there is no derivative of the displacement in its formulation, it can be applied to anywhere including the mathematical singularities such as cracks. Especially, without using any special treatment of crack propagation, with only one equation, we can predict structural deformation with or without cracks.

The original formulation proposed by Silling [37] is "bond-based peridynamics". This formulation does not distinguish the volumetric and distortional part of strain energy density. Thus, the two independent material constants reduce to one with a constraint on the Poisson's ratio. For this reason, Silling et al. [38] introduced the more general formulation, coined "state-based" PD theory. This formulation removed the constraint on the Poisson's ratio, and accounts for the separation of the volumetric and distortional part of the strain energy density. This distinction disappears if the material model has one independent constant such as the Neo-Hookean material model.

The behavior of rubber-like materials with the PD theory was considered by Silling and Bobaru [39]. They described a constitutive model to explain the behavior of rubbery materials. The strain energy density function was constructed in terms of the principal stretches, $\lambda_1, \lambda_2, \lambda_3$. They performed the simulation of stretching and tearing of a membrane for only the planar loading case. This study concerns the deformation of rubber-like materials with PD theory under different loading cases. The PD equation of motion is based on the Neo-Hookean model. Under the assumption of incompressibility, Poisson's ratio being equal to 0.5., three different loading cases of equibiaxial, planar and uniaxial

are considered as shown in Fig. 1.2. The equibiaxial and planar loadings result in extension only; however, uniaxial loading presents both extension and contraction simultaneously.
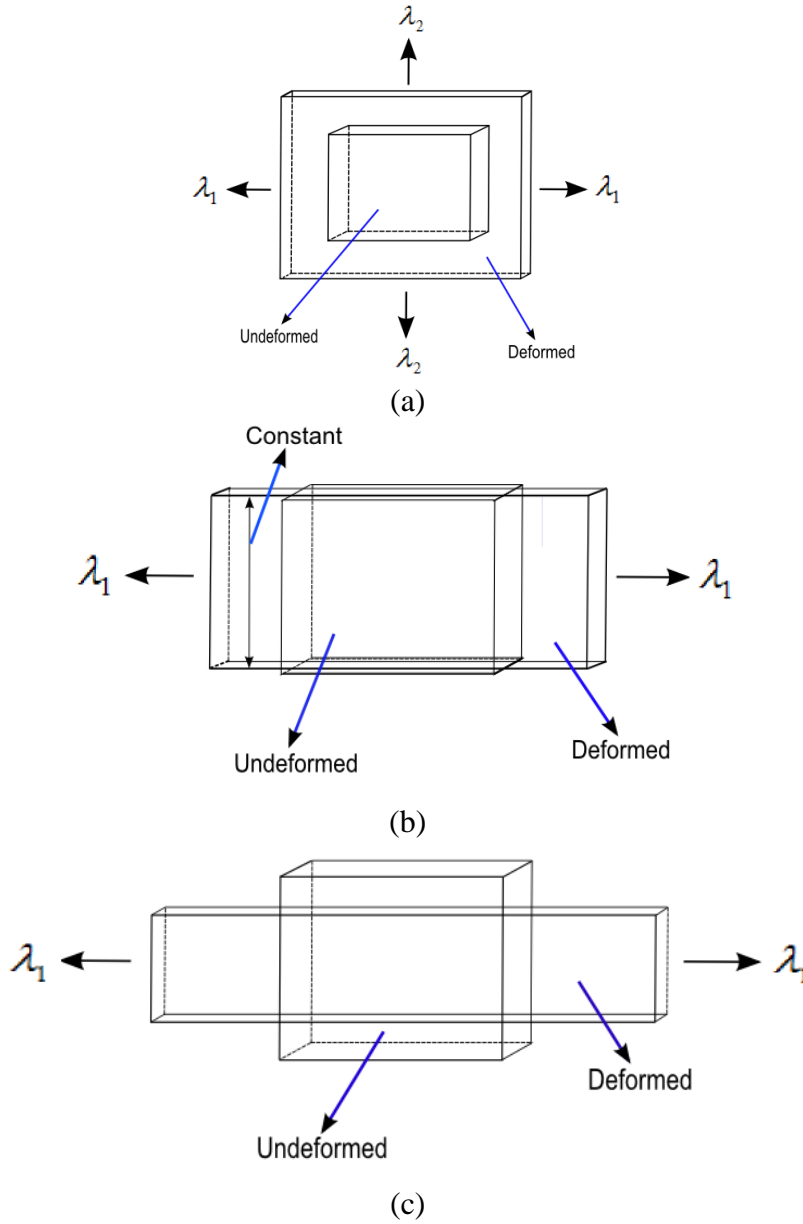
Figure 1.2. Loading conditions: (a) equibiaxial, (b) planar, and (c) uniaxial

In chapter 2, the PD concept, kinematics and strain energy density (SED) are described. The PD SED is expressed in terms of the summation of the micropotentials. The PD

equation of motion is constructed in general form in terms of the force density vector. However, its determination requires the explicit form of the SED function. In chapter 3, PD strain energy density functions, and the PD parameters for Neo-Hookean material behavior are constructed for equibiaxial, planar and uniaxial loading conditions. In chapter4, the numerical solution of the PD equation of motion along with the imposition of the boundary conditions are discussed. In Chapter 5, the numerical results are discussed for a membrane without and with a defect in the form of a hole, a crack and a solid inclusion under equibiaxial, planar and uniaxial loading conditions. In Chapter 6, the dissertation is summarized, and plans for future work is shared.

2. PERIDYNAMICS FOR HYPERELASTIC DEFORMATION

The original formulation introduced by Silling [37], and later generalized Silling et al. [38] can be extended to account for hyperelastic deformation. In this chapter, the kinematics and constitutive relations and equations of motion for hyperelastic materials are described. The following sections 2.1- 2.3 can be found in more detail in [40]

2.1. Kinematics

As shown in Fig. 2.1, the material points, $\mathbf{x}_{(k)}$ and $\mathbf{x}_{(j)}$ interact with other material points in their families defined by $H_{x_{(k)}}$ and $H_{x_{(j)}}$, respectively. Therefore, they are influenced by the collective deformation of all the material points in their families. The relative position vector $\mathbf{x}_{(j)} - \mathbf{x}_{(k)}$ represents the position vector of the two material points $\mathbf{x}_{(k)}$ and $\mathbf{x}_{(j)}$ in the undeformed state, and the current position vector $\mathbf{y}_{(j)} - \mathbf{y}_{(k)}$ represents the position vector of the two material points $\mathbf{y}_{(k)}$ and $\mathbf{y}_{(j)}$ after displaced by the displacement vector $\boldsymbol{u}_{(k)}$ and $\boldsymbol{u}_{(j)}$ in the deformed state. Therefore, the PD stretch between the material points, $\mathbf{x}_{(k)}$ and $\mathbf{x}_{(j)}$ for a large deformation can be defined as

$$\lambda_{(k)(j)} = \frac{\left|\mathbf{y}_{(j)} - \mathbf{y}_{(k)}\right|}{\left|\mathbf{x}_{(j)} - \mathbf{x}_{(k)}\right|}.$$

(8)
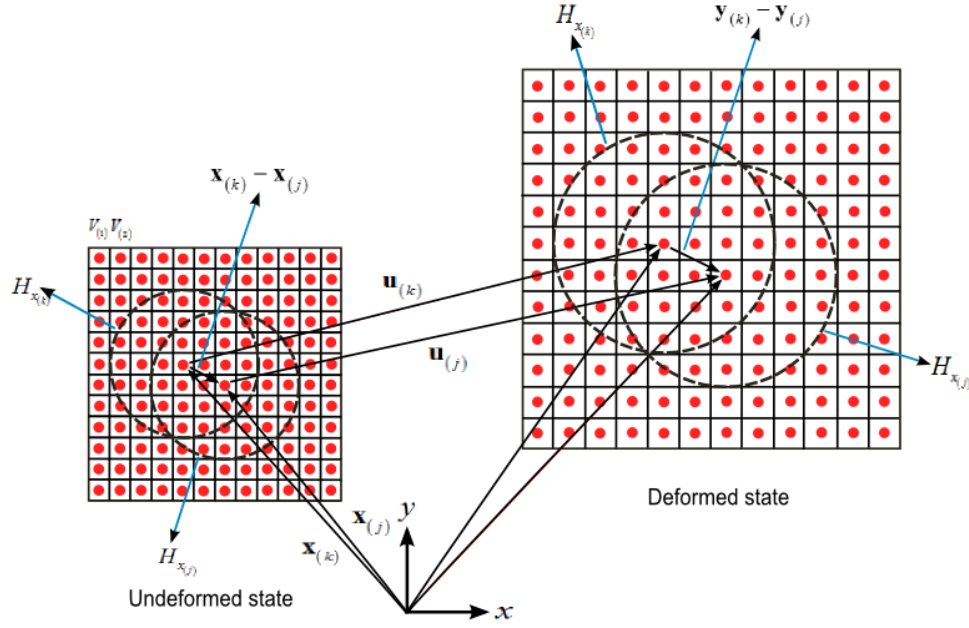
Figure 2.1. Kinematics of PD material points $\mathbf{x}_{(k)}$ and $\mathbf{x}_{(j)}$

2.2. Constitutive relations

A material point $\mathbf{x}_{(k)}$ interacts with the other material points $\mathbf{x}_{(j)}$ within a horizon. These interactions result from the exertion of the forces between the two material points $\mathbf{x}_{(k)}$ and $\mathbf{x}_{(j)}$ arising from their collective deformation. A force density can be expressed as $\boldsymbol{t}_{(k)(j)}$ or $\boldsymbol{t}_{(j)(k)}$, with the subscripts k and j indicating the sequence force exertion. For example, $\boldsymbol{t}_{(k)(j)}$ denotes the force acting at the material point k, exerted by the material point j, and $\boldsymbol{t}_{(j)(k)}$ denotes the force acting at the material point j, exerted by the material point k. As derived by Madenci and Oterkus [40], these force density vectors are defined as

$$\mathbf{t}_{(k)(j)}\left(\mathbf{u}_{(j)}-\mathbf{u}_{(k)},\mathbf{x}_{(j)}-\mathbf{x}_{(k)},t\right)=\frac{1}{2}\frac{1}{V_{(j)}}\left(\sum_{i=1}^{N}\frac{\partial\omega_{(k)(i)}}{\partial\left(\mathbf{y}_{(j)}-\mathbf{y}_{(k)}\right)}V_{(i)}\right) \tag{9a}$$

and

$$\mathbf{t}_{(j)(k)}\left(\mathbf{u}_{(k)}-\mathbf{u}_{(j)},\mathbf{x}_{(k)}-\mathbf{x}_{(j)},t\right)=\frac{1}{2}\frac{1}{V_{(j)}}\left(\sum_{i=1}^{N}\frac{\partial\omega_{(i)(k)}}{\partial\left(\mathbf{y}_{(k)}-\mathbf{y}_{(j)}\right)}V_{(i)}\right), \tag{9b}$$

in which $\omega_{(k)(j)}$ and $\omega_{(j)(k)}$ represent the micropotentials between the interaction of two

material points $\mathbf{x}_{(k)}$ and $\mathbf{x}_{(j)}$. The micropotentials $\omega_{(k)(j)}$, $\omega_{(j)(k)}$ can be expressed as

$$\omega_{(k)(j)}=\omega_{(k)(j)}\left(\mathbf{y}_{(1^{k})}-\mathbf{y}_{(k)},\mathbf{y}_{(2^{k})}-\mathbf{y}_{(k)},\cdots\right), \tag{10a}$$

and

$$\omega_{(j)(k)}=\omega_{(j)(k)}\left(\mathbf{y}_{(1^{j})}-\mathbf{y}_{(j)},\mathbf{y}_{(2^{j})}-\mathbf{y}_{(j)},\cdots\right), \tag{10b}$$

where $\mathbf{y}_{(k)}$ is the position vector which indicates the material point $\mathbf{x}_{(k)}$ in the deformed

configuration, and $\mathbf{y}_{(1^{k})}$ is the first position vector which interacts to the material point $\mathbf{x}_{(k)}$

in its family. Similarly, $\mathbf{y}_{(j)}$ is the position vector which indicates the material point $\mathbf{x}_{(j)}$

in the deformed configuration, and $\mathbf{y}_{(1^{j})}$ is the first position vector which interacts to the

material point $\mathbf{x}_{(j)}$.

The strain energy density, $W_{(k)}$ at the material point $\mathbf{x}_{(k)}$ can be obtained through a summation of the micropotentials of all interactions of material points, $\mathbf{x}_{(k)}$ and $\mathbf{x}_{(j)}$ within a horizon. Therefore, the strain energy density can be expressed in terms of micropotentials $\omega_{(k)(j)}$, $\omega_{(j)(k)}$ as

$$W_{(k)} = \frac{1}{2}\sum_{j=1}^{\infty}\frac{1}{2}\left(\omega_{(k)(j)}\left(\mathbf{y}_{(1^k)}-\mathbf{y}_{(k)},\mathbf{y}_{(2^k)}-\mathbf{y}_{(k)},\cdots\right)+\omega_{(j)(k)}\left(\mathbf{y}_{(1^j)}-\mathbf{y}_{(j)},\mathbf{y}_{(2^j)}-\mathbf{y}_{(j)},\cdots\right)\right)V_{(j)}$$

, (11)

where $\omega_{(k)(j)}$, $\omega_{(j)(k)}$ are zero when k is equal to j.

As derived by Madenci and Oterkus [40], the force density vectors, $\boldsymbol{t}_{(k)(j)}$ or $\boldsymbol{t}_{(j)(k)}$ can be expressed in terms of the strain energy density at material points k and j as

$$\mathbf{t}_{(k)(j)}\left(\mathbf{u}_{(j)}-\mathbf{u}_{(k)},\mathbf{x}_{(j)}-\mathbf{x}_{(k)},t\right)=\frac{1}{V_{(j)}}\frac{\partial W_{(k)}}{\partial\left(\left|\mathbf{y}_{(j)}-\mathbf{y}_{(k)}\right|\right)}\frac{\mathbf{y}_{(j)}-\mathbf{y}_{(k)}}{\left|\mathbf{y}_{(j)}-\mathbf{y}_{(k)}\right|}, \tag{12a}$$

and

$$\mathbf{t}_{(j)(k)}\left(\mathbf{u}_{(k)}-\mathbf{u}_{(j)},\mathbf{x}_{(k)}-\mathbf{x}_{(j)},t\right)=\frac{1}{V_{(k)}}\frac{\partial W_{(j)}}{\partial\left(\left|\mathbf{y}_{(k)}-\mathbf{y}_{(j)}\right|\right)}\frac{\mathbf{y}_{(k)}-\mathbf{y}_{(j)}}{\left|\mathbf{y}_{(k)}-\mathbf{y}_{(j)}\right|}, \tag{12b}$$

in which $\left(\mathbf{y}_{(j)}-\mathbf{y}_{(k)}\right)/\left|\mathbf{y}_{(j)}-\mathbf{y}_{(k)}\right|$ and $\left(\mathbf{y}_{(k)}-\mathbf{y}_{(j)}\right)/\left|\mathbf{y}_{(k)}-\mathbf{y}_{(j)}\right|$ are unit vectors representing the direction of the force densities $\boldsymbol{t}_{(k)(j)}$ and $\boldsymbol{t}_{(j)(k)}$.

2.3. Equation of motion

The PD equation of motion at the material point $\mathbf{x}$ can be derived as [38]

$$\rho(\mathbf{x})\ddot{\mathbf{u}}(\mathbf{x},t) = \int_H \left(\mathbf{t}(\mathbf{u}'-\mathbf{u},\mathbf{x}'-\mathbf{x},t) - \mathbf{t}'(\mathbf{u}-\mathbf{u}',\mathbf{x}-\mathbf{x}',t) \right) dH + \mathbf{b}(\mathbf{x},t), \tag{13}$$

in which ρ mass density in the reference configuration, $\mathbf{u}$ is the displacement vector, $\mathbf{b}$ is a prescribed body force density, and H is a neighborhood of the material point $\mathbf{x}$.

If the force density vectors $\mathbf{t}$ and $\mathbf{t}'$ aligned with the direction of ($\mathbf{y}_{(j)} - \mathbf{y}_{(k)}$), the balance of angular momentum [37] is automatically satisfied. As shown in Fig. 2.2, they act as a pairwise force if they are defined as

$$\mathbf{t}'(\mathbf{u}-\mathbf{u}',\mathbf{x}-\mathbf{x}',t) = -\frac{1}{2}\mathbf{f}(\mathbf{u}-\mathbf{u}',\mathbf{x}-\mathbf{x}',t), \tag{14b}$$

and

$$\mathbf{t}(\mathbf{u}'-\mathbf{u},\mathbf{x}'-\mathbf{x},t) = \frac{1}{2}\mathbf{f}(\mathbf{u}'-\mathbf{u},\mathbf{x}'-\mathbf{x},t), \tag{14a}$$

where the magnitude of the force density vectors $\mathbf{f}$ and $\mathbf{f}'$ are identical. Substituting from Eq. (14) into the PD equation of motion results in

$$\rho(\mathbf{x})\ddot{\mathbf{u}}(\mathbf{x},t) = \int_H \mathbf{f}(\mathbf{u}'-\mathbf{u},\mathbf{x}'-\mathbf{x},t)\, dH + \mathbf{b}(\mathbf{x},t). \tag{15}$$

This case is regarded as the bond-based PD formulation. The unit of force density $\mathbf{f}$ is the force per unit volume squared. As suggested by Silling [37], the pairwise force density vector can also be expressed as

$$\mathbf{f}_{(k)(j)}\left(\mathbf{u}_{(j)} - \mathbf{u}_{(k)}, \mathbf{x}_{(j)} - \mathbf{x}_{(k)}, t\right) = \frac{\partial \omega_{(k)(i)}}{\partial\left(\left|\mathbf{y}_{(j)} - \mathbf{y}_{(k)}\right|\right)} \frac{\mathbf{y}_{(j)} - \mathbf{y}_{(k)}}{\left|\mathbf{y}_{(j)} - \mathbf{y}_{(k)}\right|} \tag{16a}$$

and

$$\mathbf{f}_{(k)(j)}\left(\mathbf{u}_{(j)} - \mathbf{u}_{(k)}, \mathbf{x}_{(j)} - \mathbf{x}_{(k)}, t\right) = \left\{\frac{\partial \omega_{(k)(j)}}{\partial \lambda_{(k)(j)}} \frac{\partial \lambda_{(k)(j)}}{\partial\left(\left|\mathbf{y}_{(j)} - \mathbf{y}_{(k)}\right|\right)}\right\} \frac{\mathbf{y}_{(j)} - \mathbf{y}_{(k)}}{\left|\mathbf{y}_{(j)} - \mathbf{y}_{(k)}\right|}. \tag{16b}$$
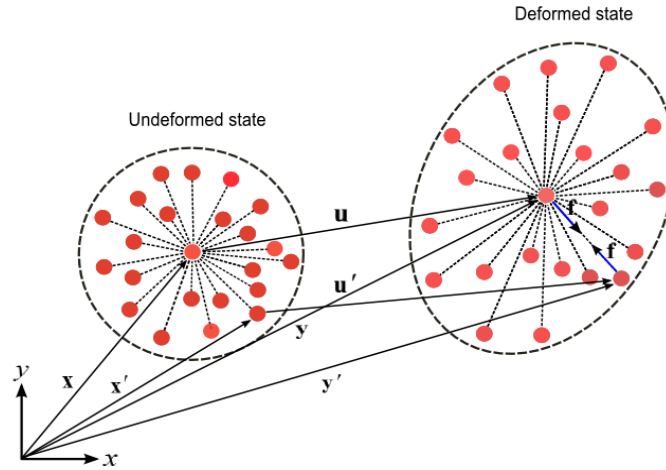
Figure 2.2. Deformation of PD material points $\mathbf{x}, \mathbf{x}'$ and pairwise force densities

It is worth noting that determination of the force density vectors requires the explicit form of the micropotential or the strain energy density function. Based on the derivation given by Madenci and Oterkus [40] for linear elastic materials, the peridynamic strain energy density function can be constructed for the Neo-Hookean material model.

3. PERIDYNAMIC STRAIN ENERGY FUNCTIONS

Based on the classical continuum mechanics, the strain energy density function at material

point $\mathbf{x}_{(k)}$ can be expressed as

$$W_{(k)} = C_1\left(I_{1(k)} - 3\right) = C_1(\lambda_{x(k)}^2 + \lambda_{y(k)}^2 + \lambda_{z(k)}^2 - 3), \tag{17}$$

in which λ_x, λ_y, λ_z are the principal stretches in the x, y and z direction respectively.

The incompressibility conditions requires that $\lambda_x\lambda_y\lambda_z = 1$. The material constant, C_1 is

related to the shear modulus, μ as $C_1 = \mu/2$. Also, the Biot stress components are related

to the strain energy density function in the form

$$\sigma_x = \frac{\partial W}{\partial \lambda_x} = 2C_1\lambda_x , \quad \sigma_y = \frac{\partial W}{\partial \lambda_y} = 2C_1\lambda_y , \quad \sigma_z = \frac{\partial W}{\partial \lambda_z} = 2C_1\lambda_z . \tag{18}$$

Substituting from Eq. (18) into Eq. (17), the strain energy density for the material point at

$\mathbf{x}_{(k)}$ can be rewritten as

$$W_{(k)} = \frac{1}{4C_1}(\sigma_{x(k)}^2 + \sigma_{y(k)}^2 + \sigma_{z(k)}^2) - 3C_1, \tag{19a}$$

or

$$W_{(k)} = \frac{1}{4C_1} \left\{ \begin{array}{c} \frac{1}{2}\left(\sigma^2_{xx(k)(k+1)} + \sigma^2_{xx(k)(k-1)}\right) + \frac{1}{2}\left(\sigma^2_{yy(k)(k+m)} + \sigma^2_{yy(k)(k-m)}\right) \\ + \frac{1}{2}\left(\sigma^2_{zz(k)(k+n)} + \sigma^2_{zz(k)(k-n)}\right) \end{array} \right\} - 3C_1 \qquad (19b)$$

where the subscripts identify the contributions arising from the internal forces exerted by material points $(k+1)$, $(k-1)$, $(k+m)$, $(k-m)$, $(k+n)$ and $(k-n)$ on material point k as shown in Fig. 3.1.
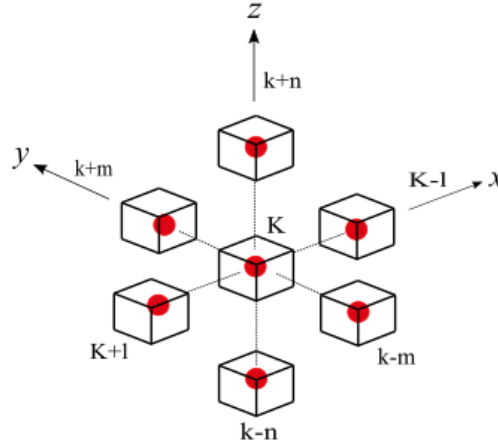
Figure 3.1. Material point interacting with others in its immediate vicinity

Also, the strain energy density function can be expressed in terms of the force density vectors as [40]

$$W_{(k)} = \frac{1}{4C_1} \sum_{\substack{j=k-l, \\ k+l, \\ k-m, \\ k+m, \\ k-n, \\ k+n}} \left(\mathbf{f}_{(k)(j)} \cdot \left(\mathbf{x}_{(j)} - \mathbf{x}_{(k)}\right)V_{(j)}\right)^2 - 3C_1. \qquad (20)$$

However, its explicit form requires the determination of the force density vector, $\mathbf{f}$ for each loading case of equibiaxial, planar and uniaxial.

3.1. Equibiaxial Loading

Under equibiaxial loading, in order to satisfy the condition of incompressibility, each principal stretch is expressed as

$$\lambda_x = \lambda, \qquad \lambda_y = \lambda, \qquad \lambda_z = \frac{1}{\lambda^2}, \tag{21}$$

in which λ is the applied stretch. After substituting from Eq. (21) into Eq. (17), the strain energy density function becomes

$$W_{(k)} = C_1 \left(2\lambda^2 + \frac{1}{\lambda^4} - 3 \right). \tag{22}$$

Based on this form of the strain energy function, the micropotential, $\omega_{(k)(j)}$ for an interaction between material points $\mathbf{x}_{(k)}$ and $\mathbf{x}_{(j)}$ can be defined as

$$\omega_{(k)(j)} = c(2\lambda_{(k)(j)}^2 + \frac{1}{\lambda^4_{(k)(j)}} - 3), \tag{23}$$

in which $\lambda_{(k)(j)}$ is the PD stretch, c is a PD material parameter. With this form, Eq. (16) leads to the explicit expression for the force densities $\mathbf{f}$ as

$$\mathbf{f}_{(k)(j)}\left(\mathbf{u}_{(j)}-\mathbf{u}_{(k)},\mathbf{x}_{(j)}-\mathbf{x}_{(k)},t\right)=\left\{4c\left(\lambda_{(k)(j)}-\frac{1}{\lambda_{(k)(j)}^{5}}\right)\frac{1}{\left|\mathbf{x}_{(j)}-\mathbf{x}_{(k)}\right|}\right\}\frac{\mathbf{y}_{(j)}-\mathbf{y}_{(k)}}{\left|\mathbf{y}_{(j)}-\mathbf{y}_{(k)}\right|}. \qquad (24)$$

In accordance with Eq. (20), the PD strain energy density function can be obtained in terms

of the PD stretch $\lambda_{(k)(j)}$ in the form

$$W_{(k)}=\frac{4c^{2}}{C_{1}}\sum_{\substack{j=k-l,\\k+l,\\k-m,\\k+m,\\k-n,\\k+n}}\left(\lambda_{(k)(j)}-\frac{1}{\lambda_{(k)(j)}^{5}}\right)^{2}\Lambda_{(k)(j)}^{2}V_{(j)}^{2}-3C_{1}, \qquad (25)$$

where $\Lambda_{(k)(j)}$ is defined as

$$\Lambda_{(k)(j)}=\left(\frac{\mathbf{x}_{(j)}-\mathbf{x}_{(k)}}{\left|\mathbf{x}_{(j)}-\mathbf{x}_{(k)}\right|}\right)\cdot\left(\frac{\mathbf{y}_{(j)}-\mathbf{y}_{(k)}}{\left|\mathbf{y}_{(j)}-\mathbf{y}_{(k)}\right|}\right). \qquad (26)$$

After expanding Eq. (25) and considering the interactions of material $\mathbf{x}_{(k)}$ with other points

within its horizon, the PD strain energy function can be constructed as

$$W_{(k)} = A_e \sum_{j=1}^{N} w_{(k)(j)} \lambda_{(k)(j)}^2 \Lambda_{(k)(j)}^2 V_{(j)} + B_e \sum_{j=1}^{N} w_{(k)(j)} \frac{1}{\lambda_{(k)(j)}^4} \Lambda_{(k)(j)}^2 V_{(j)} +$$

$$D_e \sum_{j=1}^{N} w_{(k)(j)} \frac{1}{\lambda_{(k)(j)}^{10}} \Lambda_{(k)(j)}^2 V_{(j)} + E_e \sum_{j=1}^{N} w_{(k)(j)} V_{(j)} \tag{27}$$

where N is the number of the material points inside its horizon, and the PD material parameters are defined as A_e, B_e, D_e and E_e. Also, the nondimensional influence (weight) function is defined as $w_{(k)(j)} = \delta / |\mathbf{x}_{(j)} - \mathbf{x}_{(k)}| = \delta / \xi$.

Under equibiaxial applied stretch, λ, leading to $\lambda_{(k)(j)} \geq 1$, this expression can be simplified by disregarding the third term as

$$W_{(k)} = A_e \sum_{j=1}^{N} w_{(k)(j)} \lambda_{(k)(j)}^2 \Lambda_{(k)(j)}^2 V_{(j)} + B_e \sum_{j=1}^{N} w_{(k)(j)} \frac{1}{\lambda_{(k)(j)}^4} \Lambda_{(k)(j)}^2 V_{(j)} + E_e \sum_{j=1}^{N} w_{(k)(j)} V_{(j)}, \tag{28a}$$

or

$$W_{(k)} = A_e \sum_{j=1}^{N} \frac{\delta}{|\mathbf{x}_{(j)} - \mathbf{x}_{(k)}|} \left(\frac{|\mathbf{y}_{(j)} - \mathbf{y}_{(k)}|}{|\mathbf{x}_{(j)} - \mathbf{x}_{(k)}|} \right)^2 \Lambda_{(k)(j)}^2 V_{(j)} +$$

$$B_e \sum_{j=1}^{N} \frac{\delta}{|\mathbf{x}_{(j)} - \mathbf{x}_{(k)}|} \frac{1}{\left(\frac{|\mathbf{y}_{(j)} - \mathbf{y}_{(k)}|}{|\mathbf{x}_{(j)} - \mathbf{x}_{(k)}|} \right)^4} \Lambda_{(k)(j)}^2 V_{(j)} + E_e \sum_{j=1}^{N} \frac{\delta}{|\mathbf{x}_{(j)} - \mathbf{x}_{(k)}|} V_{(j)} \tag{28b}$$

In accordance with Eqs. (12) and (14), the PD force density can be obtained as

$$\mathbf{f}_{(k)(j)}\left(\mathbf{u}_{(j)}-\mathbf{u}_{(k)},\mathbf{x}_{(j)}-\mathbf{x}_{(k)},t\right)=\frac{4\delta\Lambda^{2}_{(k)(j)}}{\left|\mathbf{x}_{(j)}-\mathbf{x}_{(k)}\right|^{2}}\left(A_{e}\lambda_{(k)(j)}-\frac{2B_{e}}{\lambda^{5}_{(k)(j)}}\right)\frac{\mathbf{y}_{(j)}-\mathbf{y}_{(k)}}{\left|\mathbf{y}_{(j)}-\mathbf{y}_{(k)}\right|}. \tag{29a}$$

The PD material parameters A_{e}, B_{e} and E_{e} can be determined by equating the PD strain energy density to that of classical continuum mechanics under a specified equibiaxial stretch of λ. For this loading, depicted in Fig. 3.2, the relative position vectors, $\mathbf{x}_{(j)}-\mathbf{x}_{(k)}$ and $\mathbf{y}_{(j)}-\mathbf{y}_{(k)}$, in the reference and deformed states, respectively, can be written as

$$\boldsymbol{\xi}=\mathbf{x}_{(j)}-\mathbf{x}_{(k)}=\left(\xi\cos\theta\right)\boldsymbol{i}+\left(\xi\sin\theta\right)\boldsymbol{j}, \tag{30a}$$

$$\boldsymbol{\eta}=\mathbf{y}_{(j)}-\mathbf{y}_{(k)}=\left(\lambda\xi\cos\theta\right)\boldsymbol{i}+\left(\lambda\xi\sin\theta\right)\boldsymbol{j}, \tag{30b}$$
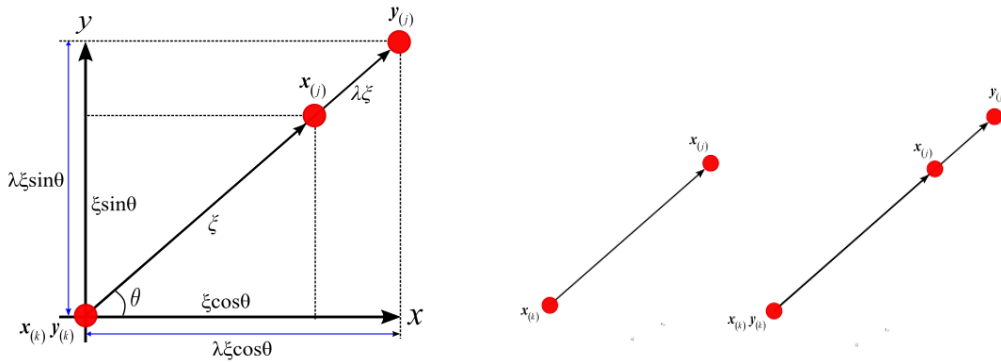
Figure 3.2. Two dimensional position vector of material points for equibiaxial loading

The direction cosines between these relative position vectors is determined as

$$\Lambda_{(k)(j)} = \frac{\mathbf{x}_{(j)} - \mathbf{x}_{(k)}}{\left|\mathbf{x}_{(j)} - \mathbf{x}_{(k)}\right|} \cdot \frac{\mathbf{y}_{(j)} - \mathbf{y}_{(k)}}{\left|\mathbf{y}_{(j)} - \mathbf{y}_{(k)}\right|} = 1 \, . \tag{31}$$

Also, the PD stretch $\lambda_{(k)(j)}$ is determined in terms of λ as

$$\lambda_{(k)(j)} = \frac{\left|\mathbf{y}_{(j)} - \mathbf{y}_{(k)}\right|}{\left|\mathbf{x}_{(j)} - \mathbf{x}_{(k)}\right|} = \lambda \, . \tag{32}$$

After substituting from Eq. (31) and Eq. (32) into Eq. (28), it can be rewritten in integral form in terms of polar coordinates, (ξ, θ) as

$$W_{(k)} = h \left\{ A_e \int\limits_0^{2\pi} \int\limits_0^{\delta} \left(\frac{\delta}{\xi}\right) \lambda^2 \xi d\xi d\theta + B_e \int\limits_0^{2\pi} \int\limits_0^{\delta} \left(\frac{\delta}{\xi}\right) \frac{1}{\lambda^4} \xi d\xi d\theta + E_e \int\limits_0^{2\pi} \int\limits_0^{\delta} \left(\frac{\delta}{\xi}\right) \xi d\xi d\theta \right\}, \tag{33}$$

in which h is thickness of the membrane and δ is the radius of horizon. Its evaluation results in

$$W_{(k)} = 2\pi\delta^2 h \left(A_e \lambda^2 + \frac{B_e}{\lambda^4} + E_e \right). \tag{34}$$

By equating Eq. (34) to Eq. (22), the PD material parameters are determined as

$$A_e = \frac{C_1}{\pi \delta^2 h}, \quad B_e = \frac{C_1}{2\pi \delta^2 h}, \quad E_e = \frac{-3C_1}{2\pi \delta^2 h}, \tag{35}$$

which depend on one common parameter $C_1 / \pi \delta^2 h$. Therefore, the PD strain energy function can be rewritten as

$$W_{(k)} = C_1 \left(2\lambda^2 + \frac{1}{\lambda^4} - 3 \right). \tag{36}$$

The material parameters A_e, B_e and E_e are determined for a material point whose horizon is completely embedded in the material. However, in the case of a material point close to the surface, these parameters should be corrected.

The correction can be achieved by considering two simple loading conditions such as principal stretches λ_x and λ_y in the x and y directions. As a result of such loading conditions, the corresponding displacements can be expressed as

$$\mathbf{u}_1^T (\mathbf{x}) = \left\{ (\lambda_x - 1) x \quad (\lambda_x - 1) y \right\}, \tag{37a}$$

$$\mathbf{u}_2^T (\mathbf{x}) = \left\{ (\lambda_y - 1) x \quad (\lambda_y - 1) y \right\}, \tag{37b}$$

in which $\mathbf{u}_1^T (\mathbf{x})$, $\mathbf{u}_2^T (\mathbf{x})$ represent the displacement vectors in the x and y direction respectively.

Based on the classical continuum mechanics, the strain energy density resulting from these loading conditions can be readily obtained as

$$W_{(m)}^{CM}\left(\mathbf{x}_{(k)}\right) = C_1\left(2\lambda_m^2 + \frac{1}{\lambda_m^4} - 3\right), \tag{38}$$

with $\left(m = x, y\right)$.

Similarly, the PD strain energy density can be obtained by applying the displacement fields given by Eq. (37) in Eq. (28) as

$$W_{(m)}^{PD}\left(\mathbf{x}_{(k)}\right) = \frac{1}{2} A_e \left\{ 2\sum_{j=1}^{N} \frac{\delta}{\left|\mathbf{x}_{(j)} - \mathbf{x}_{(k)}\right|} \left(\lambda_{(k)(j)}\right)^2 \Lambda_{(k)(j)}^2 V_{(j)} + \sum_{j=1}^{N} \frac{\delta}{\left|\mathbf{x}_{(j)} - \mathbf{x}_{(k)}\right|} \frac{1}{\left(\lambda_{(k)(j)}\right)^4} \Lambda_{(k)(j)}^2 V_{(j)} \right. $$
$$\left. -3\sum_{j=1}^{N} \frac{\delta}{\left|\mathbf{x}_{(j)} - \mathbf{x}_{(k)}\right|} V_{(j)} \right\} \tag{39}$$

with $\left(m = x, y\right)$

Corresponding to these loading conditions, the strain energy density from classical continuum mechanics, $W_{(m)}^{CM}$ must be equal to those of PD theory, $W_{(m)}^{PD}$. Therefore, the correction factor can be defined as

$$S_{m(k)} = \frac{W_{(m)}^{CM}\left(\mathbf{x}_{(k)}\right)}{W_{(m)}^{PD}\left(\mathbf{x}_{(k)}\right)}$$

$$= \frac{C_1\left(2\lambda_m^2 + \dfrac{1}{\lambda_m^4} - 3\right)}{\dfrac{1}{2}A_e\left\{2\sum\limits_{j=1}^{N}\dfrac{\delta}{\left|\mathbf{x}_{(j)} - \mathbf{x}_{(k)}\right|}\Lambda_{(k)(j)}^2 V_{(j)} + \sum\limits_{j=1}^{N}\dfrac{\delta}{\left|\mathbf{x}_{(j)} - \mathbf{x}_{(k)}\right|}\dfrac{1}{\lambda_{(k)(j)}^4}\Lambda_{(k)(j)}^2 V_{(j)} - 3\sum\limits_{j=1}^{N}\dfrac{\delta}{\left|\mathbf{x}_{(j)} - \mathbf{x}_{(k)}\right|}V_{(j)}\right\}}$$

(40)

With Eq. (40), we can express a vector of correction factors for the PD parameters as

$$\mathbf{g}(\mathbf{x}_{(k)}) = \left\{S_{1(k)} \quad S_{2(k)}\right\}^T.$$

(41)

In general, the correction factors are different at material point $\mathbf{x}_{(k)}$ and $\mathbf{x}_{(j)}$. Thus, their mean values are used as correction factor

$$\overline{\mathbf{g}}_{(k)(j)} = \frac{\mathbf{g}_{(k)} + \mathbf{g}_{(j)}}{2}.$$

(42)

These correction factors are valid for the material points interacting in the x and y directions. For arbitrary directions, the correction factors are determined based on the assumption that the correction factors in the x and y direction serve as principal axis of an ellipse as shown in Fig. 3.3.

Therefore, the correction factors in any directions can be obtained as

$$G_{(k)(j)} = \cfrac{1}{\sqrt{\left(\cfrac{n_x}{\bar{g}_{x(k)(j)}}\right)^2 + \left(\cfrac{n_y}{\bar{g}_{y(k)(j)}}\right)^2}} \,, \tag{43}$$

in which, n_x and n_y are components of an unit vector of the relative position vector,

$\mathbf{n} = \left(\mathbf{x}_{(j)} - \mathbf{x}_{(k)}\right)\big/\left|\mathbf{x}_{(j)} - \mathbf{x}_{(k)}\right|$. Also, $\bar{g}_{x(k)(j)}$ and $\bar{g}_{y(k)(j)}$ are components of a vector of

correction factor $\bar{\mathbf{g}}_{(k)(j)}$.
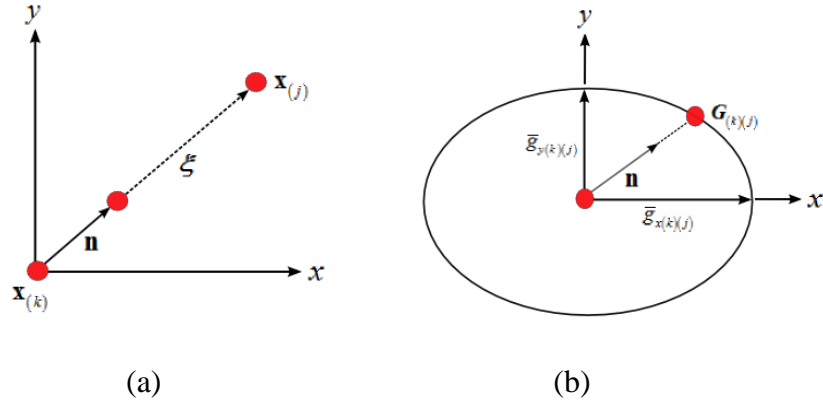
Figure 3.3. (a) The peridynamic interaction between material points $\mathbf{x}_{(k)}$ and $\mathbf{x}_{(j)}$, and (b) the ellipsoid for surface correction factors

Finally, the PD force density vector in the PD equation of motion can be rewritten as

$$\mathbf{f}_{(k)(j)} = A_e G_{(k)(j)} \frac{4\delta \Lambda_{(k)(j)}^2}{\left|\mathbf{x}_{(j)} - \mathbf{x}_{(k)}\right|^2} \left\{ \lambda_{(k)(j)} - \frac{1}{\lambda_{(k)(j)}^5} \right\} \frac{\mathbf{y}_{(j)} - \mathbf{y}_{(k)}}{\left|\mathbf{y}_{(j)} - \mathbf{y}_{(k)}\right|} \tag{44}$$

3.2. Planar Loading

Under planar loading, in order to satisfy the condition of incompressibility, each principal

stretch is expressed as

$$\lambda_x = \lambda, \qquad \lambda_y = 1, \qquad \lambda_z = \frac{1}{\lambda}, \tag{45}$$

in which λ is the applied stretch. It is worth noting that there is no deformation in the y

direction.

As substituting from Eq. (45) into Eq. (17), the strain energy density function becomes

$$W_{(k)} = C_1 \left(\lambda^2 + \frac{1}{\lambda^2} - 2 \right). \tag{46}$$

Based on this form of the strain energy function, the micropotential, $\omega_{(k)(j)}$ for an

interaction between material points $\mathbf{x}_{(k)}$ and $\mathbf{x}_{(j)}$ can be defined as [39]

$$\omega_{(k)(j)} = c(\lambda_{(k)(j)}^2 + \frac{1}{\lambda_{(k)(j)}^2} - 2) , \tag{47}$$

in which $\lambda_{(k)(j)}$ is the PD stretch, c is a PD material parameter. With this form, Eq. (16)

leads to the explicit expression for the force density, $\mathbf{f}_{(k)(j)}$ as

$$\mathbf{f}_{(k)(j)}\left(\mathbf{u}_{(j)}-\mathbf{u}_{(k)},\mathbf{x}_{(j)}-\mathbf{x}_{(k)},t\right)=2c\left(\lambda_{(k)(j)}-\frac{1}{\lambda_{(k)(j)}^{3}}\right)\left(\frac{1}{\left|\mathbf{x}_{(j)}-\mathbf{x}_{(k)}\right|}\right)\frac{\mathbf{y}_{(j)}-\mathbf{y}_{(k)}}{\left|\mathbf{y}_{(j)}-\mathbf{y}_{(k)}\right|}. \tag{48}$$

In accordance with Eq. (20), the PD strain energy density function can be obtained in terms of the PD stretch $\lambda_{(k)(j)}$ in the form

$$W_{(k)}=\frac{c^{2}}{C_{1}}\sum_{\substack{j=k-l,\\k+l,\\k-m,\\k+m,\\k-n,\\k+n}}\left(\lambda_{(k)(j)}-\frac{1}{\lambda_{(k)(j)}^{3}}\right)^{2}\Lambda_{(k)(j)}^{2}V_{(j)}^{2}-3C_{1}. \tag{49}$$

After expanding Eq. (49) and considering the interactions of material $\mathbf{x}_{(k)}$ with other points within its horizon, the PD strain energy function can be constructed as

$$W_{(k)}=A_{p}\sum_{j=1}^{N}w_{(k)(j)}\lambda_{(k)(j)}^{2}\Lambda_{(k)(j)}^{2}V_{(j)}+B_{p}\sum_{j=1}^{N}w_{(k)(j)}\frac{1}{\lambda_{(k)(j)}^{2}}\Lambda_{(k)(j)}^{2}V_{(j)}+D_{p}\sum_{j=1}^{N}w_{(k)(j)}\frac{1}{\lambda_{(k)(j)}^{6}}\Lambda_{(k)(j)}^{2}V_{(j)}$$

$$+E_{p}\sum_{j=1}^{N}w_{(k)(j)}V_{(j)}, \tag{50}$$

where N is the number of the material points inside its horizon, and the PD material parameters are defined as A_{p}, B_{p}, D_{p} and E_{p}.

Under planar loading, the applied stretch, λ, leads to $\lambda_{(k)(j)}\geq 1$; thus, this expression can be simplified by disregarding the third term as

$$W_{(k)} = A_p \sum_{j=1}^{N} w_{(k)(j)} \lambda_{(k)(j)}^2 \Lambda_{(k)(j)}^2 V_{(j)} + B_p \sum_{j=1}^{N} w_{(k)(j)} \frac{1}{\lambda_{(k)(j)}^2} \Lambda_{(k)(j)}^2 V_{(j)} + E_p \sum_{j=1}^{N} w_{(k)(j)} V_{(j)} , \qquad (51a)$$

In accordance with Eqs. (12) and (14), the PD force density can be obtained as

$$\mathbf{f}_{(k)(j)} \left(\mathbf{u}_{(j)} - \mathbf{u}_{(k)}, \mathbf{x}_{(j)} - \mathbf{x}_{(k)}, t \right) = \frac{4 \delta \Lambda_{(k)(j)}^2}{\left| \mathbf{x}_{(j)} - \mathbf{x}_{(k)} \right|^2} \left(A_p \lambda_{(k)(j)} - B_p \frac{1}{\lambda_{(k)(j)}^3} \right) \frac{\mathbf{y}_{(j)} - \mathbf{y}_{(k)}}{\left| \mathbf{y}_{(j)} - \mathbf{y}_{(k)} \right|} . \qquad (52a)$$

The PD material parameters A_p, B_p and E_p can be determined by equating the PD strain energy density to that of classical continuum mechanics under a specified planar stretch of λ. For this loading, depicted in Fig. 3.4, the relative position vectors, $\mathbf{x}_{(j)} - \mathbf{x}_{(k)}$ and $\mathbf{y}_{(j)} - \mathbf{y}_{(k)}$, in the reference and deformed states, respectively, can be written as

$$\boldsymbol{\xi} = \mathbf{x}_{(j)} - \mathbf{x}_{(k)} = \left(\xi \cos \theta \right) \boldsymbol{i} + \left(\xi \sin \theta \right) \boldsymbol{j} , \qquad (53a)$$

$$\boldsymbol{\eta} = \mathbf{y}_{(j)} - \mathbf{y}_{(k)} = \left(\lambda \xi \cos \theta \right) \boldsymbol{i} + \left(\xi \sin \theta \right) \boldsymbol{j} . \qquad (53b)$$
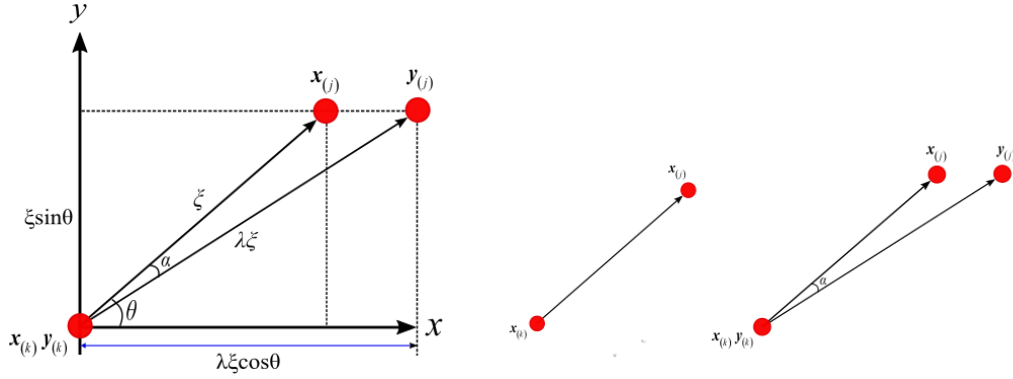
Figure 3.4 Two dimensional position vector of material points for planar loading

The direction cosines between these relative position vectors is determined as

$$\Lambda_{(k)(j)} = \frac{\mathbf{x}_{(j)} - \mathbf{x}_{(k)}}{\left|\mathbf{x}_{(j)} - \mathbf{x}_{(k)}\right|} \cdot \frac{\mathbf{y}_{(j)} - \mathbf{y}_{(k)}}{\left|\mathbf{y}_{(j)} - \mathbf{y}_{(k)}\right|} = \frac{\lambda \cos^2 \theta + \sin^2 \theta}{\sqrt{\lambda^2 \cos^2 \theta + \sin^2 \theta}} . \tag{54}$$

Also, the PD stretch $\lambda_{(k)(j)}$ is determined in terms of λ as

$$\lambda_{(k)(j)} = \frac{\left|\mathbf{y}_{(j)} - \mathbf{y}_{(k)}\right|}{\left|\mathbf{x}_{(j)} - \mathbf{x}_{(k)}\right|} = \sqrt{\lambda^2 \cos^2 \theta + \sin^2 \theta} . \tag{55}$$

After substituting from Eq. (54) and Eq. (55) into Eq. (51), it can be rewritten in integral

form in terms of polar coordinates, (ξ, θ) as

$$W_{(k)} = h \left\{ A_p \int_0^{2\pi} \int_0^\delta \left(\frac{\delta}{\xi}\right)\left(\lambda\cos^2\theta + \sin^2\theta\right)^2 \xi d\xi d\theta + B_p \int_0^{2\pi}\int_0^\delta \left(\frac{\delta}{\xi}\right)\frac{\left(\lambda\cos^2\theta + \sin^2\theta\right)^2}{\left(\lambda^2\cos^2\theta + \sin^2\theta\right)^2}\xi d\xi d\theta \right.$$

$$\left. + E_p \int_0^{2\pi}\int_0^\delta \left(\frac{\delta}{\xi}\right)\xi d\xi d\theta \right\} \tag{56}$$

in which h is thickness of the membrane and δ is the radius of horizon. Its evaluation results in

$$W_{(k)} = h\delta^2\pi\left\{ \frac{A_p}{4}\left(3\lambda^2 + 2\lambda + 3\right) + \frac{B_p\left(\lambda^2 + 6\lambda + 1\right)}{\lambda\left(\lambda+1\right)^2} + 2E_p \right\}. \tag{57}$$

The PD material parameters A_p, B_p and E_p can be determined by equating the PD strain energy density and that of classical continuum mechanics at three different values of stretch, $\lambda = 1$, $\lambda = 2$ and $\lambda = 4$ as

$$A_p = \frac{31}{25}\frac{C_1}{\pi h\delta^2}, \quad B_p = \frac{89}{81}\frac{C_1}{\pi h\delta^2}, \quad E_p = -\frac{138}{59}\frac{C_1}{\pi h\delta^2}, \tag{58}$$

which depend on one common parameter $C_1/\pi\delta^2 h$. Therefore, the PD strain energy function can be rewritten as

$$W_{(k)} = C_1\left\{ \frac{31}{100}\left(3\lambda^2 + 2\lambda + 3\right) + \frac{89}{81}\frac{\left(\lambda^2 + 6\lambda + 1\right)}{\lambda\left(\lambda+1\right)^2} - \frac{276}{59} \right\}. \tag{59}$$

Similar to the equibiaxial loading, the correction can be achieved by considering two simple loading conditions such as principal stretches λ_x and λ_y in the x and y directions. However, in the planar loading case, only the x direction component needs to be corrected because the deformation does not happen in the y direction. Therefore, as a result of such loading conditions, the corresponding displacements in the x direction can be expressed as

$$\mathbf{u}_1^T(\mathbf{x}) = \left\{ (\lambda_x - 1)x \quad 0 \right\}, \tag{60}$$

in which $\mathbf{u}_1^T(\mathbf{x})$ represents the displacement vector in the x direction.

Based on the classical continuum mechanics, the strain energy density in the x direction resulting from these loading conditions can be readily obtained as

$$W_{(x)}^{CM}(\mathbf{x}_{(k)}) = C_1\left(2\lambda_x^2 + \frac{1}{\lambda_x^2} - 2\right), \tag{61}$$

Similarly, the PD strain energy density in the same direction can be obtained by applying the displacement fields given by Eq. (60) in Eq. (51) as

$$W_{(x)}^{PD}(\mathbf{x}_{(k)}) = \frac{1}{2}A_p\left\{\sum_{j=1}^{N}\frac{\delta}{\left|\mathbf{x}_{(j)} - \mathbf{x}_{(k)}\right|}\lambda_{(k)(j)}^2\Lambda_{(k)(j)}^2 V_{(j)} + \frac{31}{35}\sum_{j=1}^{N}\frac{\delta}{\left|\mathbf{x}_{(j)} - \mathbf{x}_{(k)}\right|}\frac{1}{\lambda_{(k)(j)}^2}\Lambda_{(k)(j)}^2 V_{(j)}\right.$$

$$\left. - \frac{66}{35}\sum_{j=1}^{N}\frac{\delta}{\left|\mathbf{x}_{(j)} - \mathbf{x}_{(k)}\right|}V_{(j)}\right\}, \tag{62}$$

Corresponding to these loading conditions, the strain energy density from classical continuum mechanics, $W_{(x)}^{CM}$ must be equal to that of PD theory, $W_{(x)}^{PD}$. Therefore, the correction factor in the x direction can be defined as

$$S_{x(k)} = \frac{W_{(x)}^{CM}\left(\mathbf{x}_{(k)}\right)}{W_{(x)}^{PD}\left(\mathbf{x}_{(k)}\right)} \tag{63}$$

$$= \frac{C_1\left(2\lambda_x^2 + \dfrac{1}{\lambda_x^2} - 2\right)}{\dfrac{1}{2}A_p\left\{\displaystyle\sum_{j=1}^{N}\frac{\delta}{\left|\mathbf{x}_{(j)} - \mathbf{x}_{(k)}\right|}\lambda_{(k)(j)}^2\Lambda_{(k)(j)}^2 V_{(j)} + \frac{31}{35}\displaystyle\sum_{j=1}^{N}\frac{\delta}{\left|\mathbf{x}_{(j)} - \mathbf{x}_{(k)}\right|}\frac{1}{\lambda_{(k)(j)}^2}\Lambda_{(k)(j)}^2 V_{(j)} - \frac{66}{35}\displaystyle\sum_{j=1}^{N}\frac{\delta}{\left|\mathbf{x}_{(j)} - \mathbf{x}_{(k)}\right|}V_{(j)}\right\}}$$

Also, in the y direction, the surface correction factor should be equal to 1, i.e. $S_{y(k)} = 1$ because parameter does not need to be corrected in this direction.

Finally, the PD force density vector in the PD equation of motion can be rewritten as

$$\mathbf{f}_{(k)(j)}\left(\mathbf{u}_{(j)} - \mathbf{u}_{(k)}, \mathbf{x}_{(j)} - \mathbf{x}_{(k)}, t\right) = A_p G_{(k)(j)}\frac{4\delta\Lambda_{(k)(j)}^2}{\left|\mathbf{x}_{(j)} - \mathbf{x}_{(k)}\right|^2}\left\{\lambda_{(k)(j)} - \frac{31}{35}\frac{1}{\lambda_{(k)(j)}^3}\right\}\frac{\mathbf{y}_{(j)} - \mathbf{y}_{(k)}}{\left|\mathbf{y}_{(j)} - \mathbf{y}_{(k)}\right|} \tag{64}$$

3.3. Uniaxial Loading

Under uniaxial loading, in order to satisfy the condition of incompressibility, each principal stretch is expressed as

$$\lambda_x = \lambda, \qquad \lambda_y = \frac{1}{\sqrt{\lambda}}, \qquad \lambda_z = \frac{1}{\sqrt{\lambda}}, \tag{65}$$

in which λ is the applied stretch. It is worth noting that deformation exhibits both extension and contraction simultaneously.

As substituting from Eq. (65) into Eq. (17), the strain energy density function becomes

$$W_{(k)} = C_1 \left(\lambda^2 + \frac{2}{\lambda} - 3 \right). \tag{66}$$

Based on this form of the strain energy function, the micropotential, $\omega_{(k)(j)}$ for an interaction between material points $\mathbf{x}_{(k)}$ and $\mathbf{x}_{(j)}$ can be defined as

$$\omega_{(k)(j)} = c \left(\lambda^2_{(k)(j)} + \frac{2}{\lambda_{(k)(j)}} - 3 \right), \tag{67}$$

in which $\lambda_{(k)(j)}$ is the PD stretch, c is a PD material parameter. With this form, Eq. (16) leads to the explicit expression for the force densities $\mathbf{f}$ as

$$\mathbf{f}_{(k)(j)} \left(\mathbf{u}_{(j)} - \mathbf{u}_{(k)}, \mathbf{x}_{(j)} - \mathbf{x}_{(k)}, t \right) = 2c \left(\lambda_{(k)(j)} - \frac{1}{\lambda^2_{(k)(j)}} \right) \frac{1}{\left| \mathbf{x}_{(j)} - \mathbf{x}_{(k)} \right|} \frac{\mathbf{y}_{(j)} - \mathbf{y}_{(k)}}{\left| \mathbf{y}_{(j)} - \mathbf{y}_{(k)} \right|}. \tag{68}$$

In accordance with Eq. (20), the PD strain energy density function can be obtained in terms of the PD stretch $\lambda_{(k)(j)}$ in the form

$$W_{(k)} = \frac{c^2}{C_1} \sum_{\substack{j=k-l, \\ k+l, \\ k-m, \\ k+m, \\ k-n, \\ k+n}} \left(\lambda_{(k)(j)} - \frac{1}{\lambda_{(k)(j)}^2} \right)^2 \Lambda_{(k)(j)}^2 V_{(j)}^2 - 3C_1 . \tag{69}$$

In order to account for the interactions of material $\mathbf{x}_{(k)}$ with other points within its horizon, the PD strain energy function can be constructed as

$$W_{(k)} = A_u \sum_{j=1}^{N} w_{(k)(j)} \lambda_{(k)(j)}^2 \Lambda_{(k)(j)}^2 V_{(j)} + B_u \sum_{j=1}^{N} w_{(k)(j)} \frac{1}{\lambda_{(k)(j)}} \Lambda_{(k)(j)}^2 V_{(j)}$$
$$+ D_u \sum_{j=1}^{N} w_{(k)(j)} \frac{1}{\lambda_{(k)(j)}^4} \Lambda_{(k)(j)}^2 V_{(j)} + E_u \sum_{j=1}^{N} w_{(k)(j)} V_{(j)} \tag{70a}$$

where N is the number of the material points inside its horizon, and the PD material parameters are defined as A_u, B_u, D_u and E_u.

In accordance with Eqs. (12) and (14), the PD force density can be obtained as

$$\mathbf{f}_{(k)(j)} = \frac{2\delta \Lambda_{(k)(j)}^2}{\left| \mathbf{x}_{(j)} - \mathbf{x}_{(k)} \right|^2} \left(2A_u \lambda_{(k)(j)} - B_u \frac{1}{\lambda_{(k)(j)}^2} - 4D_u \frac{1}{\lambda_{(k)(j)}^5} \right) \frac{\mathbf{y}_{(j)} - \mathbf{y}_{(k)}}{\left| \mathbf{y}_{(j)} - \mathbf{y}_{(k)} \right|} \tag{71}$$

The PD material parameters A_u, B_u, D_u and E_u can be determined by equating the PD strain energy density to that of classical continuum mechanics under a specified planar stretch of λ. For this loading, depicted in Fig. 3.5, the relative position vectors, $\mathbf{x}_{(j)} - \mathbf{x}_{(k)}$ and $\mathbf{y}_{(j)} - \mathbf{y}_{(k)}$, in the reference and deformed states, respectively, can be written as
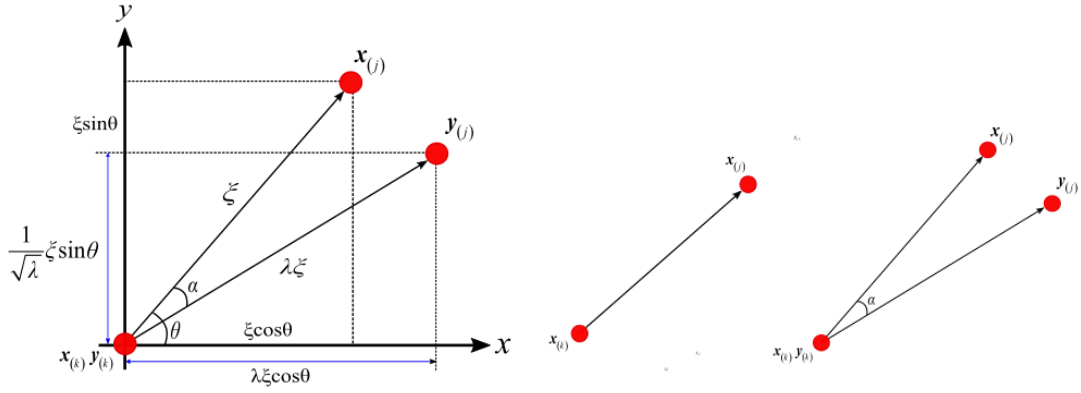
Figure 3.5 Two dimensional position vector of material points for uniaxial loading

$$\boldsymbol{\xi} = \mathbf{x}_{(j)} - \mathbf{x}_{(k)} = \left(\xi\cos\theta\right)\boldsymbol{i} + \left(\xi\sin\theta\right)\boldsymbol{j}, \tag{72a}$$

$$\boldsymbol{\eta} = \mathbf{y}_{(j)} - \mathbf{y}_{(k)} = \left(\lambda\xi\cos\theta\right)\boldsymbol{i} + \left(\frac{1}{\sqrt{\lambda}}\xi\sin\theta\right)\boldsymbol{j}. \tag{72b}$$

The direction cosine between these relative position vectors is determined as

$$\Lambda_{(k)(j)} = \frac{\mathbf{x}_{(j)} - \mathbf{x}_{(k)}}{\left|\mathbf{x}_{(j)} - \mathbf{x}_{(k)}\right|} \cdot \frac{\mathbf{y}_{(j)} - \mathbf{y}_{(k)}}{\left|\mathbf{y}_{(j)} - \mathbf{y}_{(k)}\right|} = \frac{\lambda\cos^2\theta + \dfrac{1}{\sqrt{\lambda}}\sin^2\theta}{\sqrt{\lambda^2\cos^2\theta + \dfrac{1}{\lambda}\sin^2\theta}}. \tag{73}$$

Also, the PD stretch $\lambda_{(k)(j)}$ is determined in terms of λ as

$$\lambda_{(k)(j)} = \frac{\left| \mathbf{y}_{(j)} - \mathbf{y}_{(k)} \right|}{\left| \mathbf{x}_{(j)} - \mathbf{x}_{(k)} \right|} = \sqrt{\lambda^2 \cos^2 \theta + \frac{1}{\lambda} \sin^2 \theta} \ . \tag{74}$$

After substituting from Eq. (73) and Eq. (74) into Eq. (70), it can be rewritten in integral

form in terms of polar coordinates, (ξ, θ) as

$$W_{(k)} = h \left\{ A_u \int_0^{2\pi} \int_0^{\delta} \left(\frac{\delta}{\xi} \right) \left(\lambda \cos^2 \theta + \frac{1}{\sqrt{\lambda}} \sin^2 \theta \right)^2 \xi d\xi d\theta + B_u \int_0^{2\pi} \int_0^{\delta} \left(\frac{\delta}{\xi} \right) \frac{\left(\lambda \cos^2 \theta + \frac{1}{\sqrt{\lambda}} \sin^2 \theta \right)^2}{\left(\lambda^2 \cos^2 \theta + \frac{1}{\lambda} \sin^2 \theta \right)^{\frac{3}{2}}} \xi d\xi d\theta \right.$$

$$\left. + D_u \int_0^{2\pi} \int_0^{\delta} \left(\frac{\delta}{\xi} \right) \frac{\left(\lambda \cos^2 \theta + \frac{1}{\sqrt{\lambda}} \sin^2 \theta \right)^2}{\left(\lambda^2 \cos^2 \theta + \frac{1}{\lambda} \sin^2 \theta \right)^3} \xi d\xi d\theta + E_u \int_0^{2\pi} \int_0^{\delta} \left(\frac{\delta}{\xi} \right) \xi d\xi d\theta \right\}, \tag{75}$$

in which h is thickness of the membrane and δ is the radius of horizon. Its evaluation

results in

$$W_{(k)} = h\delta^2 \left[A_u \frac{\pi}{4} \left(3\lambda^2 + \frac{3}{\lambda} + 2\sqrt{\lambda} \right) + B_u \frac{8 \left\{ \lambda^2 E \left(1 - \frac{1}{\lambda^3} \right) + \lambda^{1/2} K \left(1 - \frac{1}{\lambda^3} \right) \right\}}{\left(\lambda^{3/2} + 1 \right)^2} \right.$$

$$\left. + D_u \frac{3}{4} \pi \left(\frac{1}{\lambda^{2.5}} + \frac{2}{3\lambda} + \sqrt{\lambda} \right) + 2\pi E_u \right], \tag{76}$$

in which E and K in the second term denote a complete elliptical integral of the first and

second kind respectively.

The PD material parameters A_u, B_u, D_u and E_u can be determined by equating the PD strain energy density and that of classical continuum mechanics. However, these parameters need to be determined separately under tension and compression loads. Accordingly, the parameters A_u^t, B_u^t, D_u^t and E_u^t for representing the tensile load can be obtained by considering four different values of stretch, $\lambda = 1$, $\lambda = 2$, $\lambda = 3$ and $\lambda = 4$, and the parameters A_u^c, B_u^c, D_u^c and E_u^c for representing the compression load can be determined in the least square sense for the stretch range of 0.4 to 1 as

$$A_u^t = \frac{64}{49}\frac{C_1}{\pi h \delta^2}, \quad B_u^t = \frac{3}{4}\frac{C_1}{\pi h \delta^2}, \quad D_u^t = \frac{8}{17}\frac{C_1}{\pi h \delta^2}, \quad E_u^t = -\frac{48}{19}\frac{C_1}{\pi h \delta^2}, \tag{77a}$$

and

$$A_u^c = -\frac{109}{14}\frac{C_1}{\pi h \delta^2}, \quad B_u^c = -\frac{239}{16}\frac{C_1}{\pi h \delta^2}, \quad D_u^c = \frac{5}{18}\frac{C_1}{\pi h \delta^2}, \quad E_u^c = \frac{202}{9}\frac{C_1}{\pi h \delta^2} \tag{77b}$$

which depend on one common parameter $C_1 / \pi \delta^2 h$.

Similar to the previous loading cases, the correction factors can be achieved by considering two simple loading conditions such as principal stretches λ_x and λ_y in the x and y directions. As a result of such loading conditions, the corresponding displacements can be expressed as

$$\mathbf{u}_1^T(\mathbf{x}) = \left\{ (\lambda_x - 1)x \quad \left(\frac{1}{\sqrt{\lambda_x}} - 1 \right)y \right\}, \tag{78a}$$

$$\mathbf{u}_2^T(\mathbf{x}) = \left\{ \left(\frac{1}{\sqrt{\lambda_y}} - 1 \right)x \quad (\lambda_y - 1)y \right\}, \tag{78b}$$

in which $\mathbf{u}_1^T(\mathbf{x})$, $\mathbf{u}_2^T(\mathbf{x})$ represent the displacement vectors in the x and y direction respectively.

Based on the classical continuum mechanics, the strain energy density resulting from these loading conditions can be readily obtained as

$$W_{(m)}^{CM}(\mathbf{x}_{(k)}) = C_1 \left(\lambda_m^2 + \frac{2}{\lambda_m} - 3 \right), \tag{79}$$

with $(m = x, y)$.

Similarly, the PD strain energy density can be obtained by applying the displacement fields given by Eq. (78) in Eq. (70) as

$$W_{(m)}^{PD}(\mathbf{x}_{(k)}) = A_u^t \left\{ \sum_{j=1}^N \frac{\delta}{\left| \mathbf{x}_{(j)} - \mathbf{x}_{(k)} \right|} \lambda_{(k)(j)}^2 \Lambda_{(k)(j)}^2 V_{(j)} + \frac{27}{47} \sum_{j=1}^N \frac{\delta}{\left| \mathbf{x}_{(j)} - \mathbf{x}_{(k)} \right|} \frac{1}{\lambda_{(k)(j)}} \Lambda_{(k)(j)}^2 V_{(j)} \right.$$

$$\left. + \frac{9}{25} \sum_{j=1}^N \frac{\delta}{\left| \mathbf{x}_{(j)} - \mathbf{x}_{(k)} \right|} \frac{1}{\lambda_{(k)(j)}^4} \Lambda_{(k)(j)}^2 V_{(j)} - \frac{29}{15} \sum_{j=1}^N \frac{\delta}{\left| \mathbf{x}_{(j)} - \mathbf{x}_{(k)} \right|} V_{(j)} \right\}, \tag{80}$$

with $(m = x, y)$

Corresponding to these loading conditions, the strain energy density from classical continuum mechanics, $W_{(m)}^{CM}$ must be equal to those of PD theory, $W_{(m)}^{PD}$. Therefore, the correction factor can be defined as

$$
S_{m(k)} = \frac{W_{(m)}^{CM}\left(\mathbf{x}_{(k)}\right)}{W_{(m)}^{PD}\left(\mathbf{x}_{(k)}\right)}
$$

$$
= \frac{C_1\left(\lambda_m^2 + \dfrac{2}{\lambda_m} - 3\right)}{A_u^t\left\{\displaystyle\sum_{j=1}^{N}\frac{\delta}{\left|\mathbf{x}_{(j)} - \mathbf{x}_{(k)}\right|}\lambda_{(k)(j)}^2\Lambda_{(k)(j)}^2 V_{(j)} + \frac{27}{47}\displaystyle\sum_{j=1}^{N}\frac{\delta}{\left|\mathbf{x}_{(j)} - \mathbf{x}_{(k)}\right|}\frac{1}{\lambda_{(k)(j)}}\Lambda_{(k)(j)}^2 V_{(j)} \right. }
$$
$$
\left. + \frac{9}{25}\displaystyle\sum_{j=1}^{N}\frac{\delta}{\left|\mathbf{x}_{(j)} - \mathbf{x}_{(k)}\right|}\frac{1}{\lambda_{(k)(j)}^4}\Lambda_{(k)(j)}^2 V_{(j)} - \frac{29}{15}\displaystyle\sum_{j=1}^{N}\frac{\delta}{\left|\mathbf{x}_{(j)} - \mathbf{x}_{(k)}\right|}V_{(j)}\right\}
$$

(81)

Finally, the PD force density vector in the PD equation of motion can be rewritten as

$$
\mathbf{f}_{(k)(j)} = A_u^t G_{(k)(j)}\frac{2\delta\Lambda_{(k)(j)}^2}{\left|\mathbf{x}_{(j)} - \mathbf{x}_{(k)}\right|^2}\left(2\lambda_{(k)(j)} - \frac{27}{47}\frac{1}{\lambda_{(k)(j)}^2} - \frac{36}{25}\frac{1}{\lambda_{(k)(j)}^5}\right)\frac{\mathbf{y}_{(j)} - \mathbf{y}_{(k)}}{\left|\mathbf{y}_{(j)} - \mathbf{y}_{(k)}\right|}
$$

(82)

4. NUMERICAL ANALYSIS

The peridynamic equation of motion is in the form of an integro-differential equation. Therefore, its solution cannot be obtained with analytical approaches. This chapter concerns the numerical spatial and time integrations of the PD equation, and the approach for imposing boundary conditions as described in [40, 41, 47].

4.1 Spatial integration

The spatial integration in PD equation of motion can be performed by considering the concept of collocation (integration) points. After discretizing the domain of the material into the subdomain, collocation points are placed in the subdomain as shown in Fig. 4.1. Then, by summing up all volumes of each collocation point within a horizon, spatial integration of PD equation can be implemented.

For a particular material point k, an integral of PD equation in Eq. (13) can be approximated as

$$\rho\left(\mathbf{x}_{(k)}\right)\ddot{\mathbf{u}}\left(\mathbf{x}_{(k)},t\right) = \sum_{j=1}^{N} w_{(j)}\mathbf{f}\left(\mathbf{u}(\mathbf{x}_{(j)},t)-\mathbf{u}(\mathbf{x}_{(k)},t),\mathbf{x}_{(j)}-\mathbf{x}_{(k)}\right)V_{(j)} + \mathbf{b}\left(\mathbf{x}_{(k)},t\right), \tag{83}$$

in which N represents the number of subdomain inside its horizon. The vector $\mathbf{x}_{(k)}$ and $\mathbf{x}_{(j)}$ indicate the positions of the kth and j^{th} collocation points, respectively. The parameter $w_{(j)}$ is the influence (weight) function. The $V_{(j)}$ represents the volume of material point, and it has each cubic subdomain at material point j^{th}. In Eq. (83), the

truncation error has the order of $O(\Delta^2)$ for uniform spacing of Δ between the material points [42].
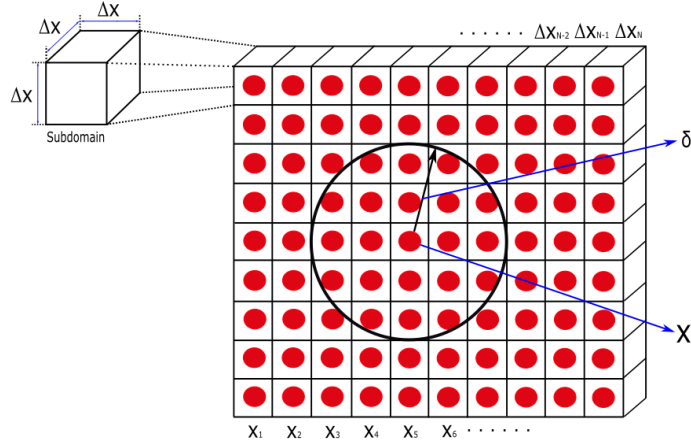
Figure 4.1. Discretization of the domain of interest for two dimensional region

As shown in Fig. 4.2, a one-dimensional rectangular bar is considered in order to explain the construction of the set of ordinary differential equations in Eq. (83). The bar is discretized into cubic subdomains, and each subdomain contains a collocation point. Also, the response function vanishes beyond its horizon size, δ as shown in Fig. 4.2.

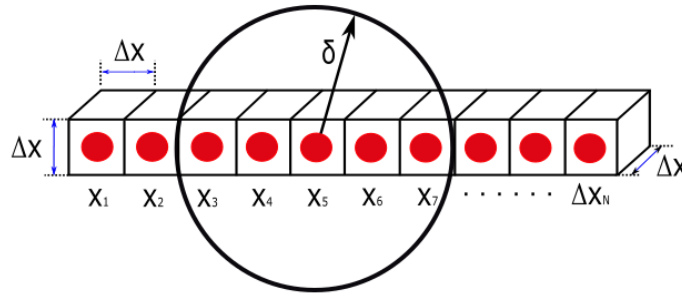As a result, for a material point at $\mathbf{x}_5$, the ordinary differential equations can be expressed as

$$\rho\ddot{\mathbf{u}}(\mathbf{x}_5,t) = \mathbf{f}(\boldsymbol{\xi}_{53},\boldsymbol{\eta}_{53})V_3 + \mathbf{f}(\boldsymbol{\xi}_{54},\boldsymbol{\eta}_{54})V_4 + \mathbf{f}(\boldsymbol{\xi}_{56},\boldsymbol{\eta}_{56})V_6 + \mathbf{b}(\mathbf{x}_5,t),$$

(84)

in which

$$\boldsymbol{\eta} = \mathbf{u} - \mathbf{u}' \tag{85a}$$

and

$$\boldsymbol{\xi} = \mathbf{x} - \mathbf{x}'. \tag{85b}$$

Figure 4.2. Discretization of rectangular bar

4.2 Time integration

Numerical time integration can be performed by using backward and forward difference explicit integration schemes. However, the PD equation of motion includes the inertial terms; it is not directly applicable to static and quasi-static problems. Therefore, a special treatment is required so that the system will converge to a static condition in a short amount of computational time. Although there are different techniques available for this purpose, adaptive dynamic relaxation (ADR) introduced by Kilic and Madenci [41] can be utilized. The static solution can be regarded as the steady-state solution of the total transient response of the PD equation. An artificial damping is included into the equation, and it

drives the solution into the steady-state solution in a faster way. However, it is not possible at all times to obtain the most appropriate damping coefficient. Hence, by using adaptive dynamic relaxation method introduced by Underwood [43], the damping coefficient can be changed at each time iteration. Then, the steady-state solution can be obtained with faster convergence.

The peridynamic equation of motion can be expressed as a set of ordinary differential equations for all material points by removing the acceleration term and introducing a fictitious diagonal density and damping matrix as

$$\mathbf{D}\ddot{\mathbf{U}}(\mathbf{X},t)+c\mathbf{D}\dot{\mathbf{U}}(\mathbf{X},t)=\mathbf{F}(\mathbf{U},\mathbf{U}',\mathbf{X},\mathbf{X}') \ , \tag{86}$$

in which $\mathbf{D}$ is the fictitious diagonal density matrix and c is the damping coefficient, and they are achieved by Greschgorin's theorem [43] and Rayleigh's quotient, respectively. The vectors $\mathbf{X}$ and $\mathbf{U}$ indicate the initial position and displacement of the collocation points, respectively, they can be written as

$$\mathbf{X}^{T}=\{\mathbf{x}_{1},\mathbf{x}_{2},\ldots,\mathbf{x}_{M}\} \tag{87a}$$

and

$$\mathbf{U}^{T}=\{\mathbf{u}(\mathbf{x}_{1},t),\mathbf{u}(\mathbf{x}_{2},t),\ldots,\mathbf{u}(\mathbf{x}_{M},t)\}, \tag{87b}$$

in which M is the total number of material points. As a result, the vector $\mathbf{F}$ consists of peridynamic interactions and body forces, and its component at i^{th} can be written as

$$\mathbf{F}_i = \sum_{j=1}^{N} \mathbf{f}_{(i)(j)}\left(\upsilon_{cj}V_{(j)}\right) + \mathbf{b}_{(i)} \tag{88}$$

By making use of central-difference explicit integration, displacements and velocities for the next iteration step can be achieved as

$$\dot{\mathbf{U}}^{n+1/2} = \frac{\left(\left(2-c^n\Delta t\right)\dot{\mathbf{U}}^{n-1/2} - 2\Delta t\mathbf{D}^{-1}\mathbf{F}^n\right)}{\left(2+c^n\Delta t\right)} \tag{89a}$$

and

$$\mathbf{U}^{n+1} = \mathbf{U}^{n} + \Delta t\, \dot{\mathbf{U}}^{n+1/2}, \tag{89b}$$

where n represents the nth iteration. However, due to the unknown velocity field at $t^{-1/2}$, Eq. (89a) and Eq. (89b) cannot be utilized for the first iteration process. By assuming that $\mathbf{U}^0 \neq 0$ and $\dot{\mathbf{U}}^0 = 0$, integration can be started by

$$\dot{\mathbf{U}}^{1/2} = -\Delta t\, \mathbf{D}^{-1}\mathbf{F}^0\big/2 \tag{90}$$

in which $\mathbf{F}, \mathbf{D}, c$ and Δt represent the force vector, density matrix, damping coefficient, and time step size, respectively. Among all of these, only physical term is the force vector, $\mathbf{F}$ and the other quantities are not physically meaningful. Therefore, they are selected to achieve faster convergence.

A time step size, $\Delta t = 1$ is useful in dynamic relaxation method. The diagonal elements of the density matrix $\mathbf{D}$ can be selected based on Greschgorin's theorem, and they can be expressed as

$$\lambda_{ii} \geq \frac{1}{4} \Delta t^2 \sum_j |K_{ij}|, \tag{91}$$

where K_{ij} is the stiffness matrix. In accordance with the stability condition given by Underwood [43], the inequality sign is determined in Eq. (91), and it ensures stability of the behavior of the system. As illustrated by Lovie and Metzger [44], since all of values in Eq. (91) are dependent upon absolute values of global stiffness matrix, those values are coordinate frame dependent. Hence, as proposed by Suave and Metzger [45], to make frame invariant, by selecting the values based on minimum dimension, an alternative approach can be performed. This method appears to diminish overshooting as compared to Greschgorin's theorem. Therefore, the present solutions of PD equations also use a frame Invariant density matrix.

By taking derivative of PD interaction forces with respect to the relative position vector, $\mathbf{\eta}+\mathbf{\xi}$, the stiffness matrix is constructed, and it can be approximated as

$$\sum_j \left|K_{ij}\right| = \sum_{j=1}^{N} \frac{\partial \mathbf{f}_{(i)(j)}}{\partial \left(\left|\mathbf{y}_{(j)} - \mathbf{y}_{(i)}\right|\right)} \cdot \mathbf{e}, \tag{92}$$

which leads to the specific expressions for the equibiaxial, planar and uniaxial loadings as

$$\sum_j \left|K_{ij}^e\right| = \sum_j \frac{\left|\left(\mathbf{\eta}_{(i)(j)} + \mathbf{\xi}_{(i)(j)}\right) \cdot \mathbf{e}\right|}{\left|\mathbf{\eta}_{(i)(j)} + \mathbf{\xi}_{(i)(j)}\right|} \frac{4\delta\Lambda_{(i)(j)}^2}{\left|\mathbf{\xi}_{(i)(j)}\right|^3} \left(A_e + \frac{10B_e}{\lambda_{(i)(j)}^6}\right) \tag{93a}$$

$$\sum_j \left|K_{ij}^p\right| = \sum_j \frac{\left|\left(\mathbf{\eta}_{(i)(j)} + \mathbf{\xi}_{(i)(j)}\right) \cdot \mathbf{e}\right|}{\left|\mathbf{\eta}_{(i)(j)} + \mathbf{\xi}_{(i)(j)}\right|} \frac{4\delta\Lambda_{(i)(j)}^2}{\left|\mathbf{\xi}_{(i)(j)}\right|^3} \left(A_p + \frac{3B_p}{\lambda_{(i)(j)}^4}\right) \tag{93b}$$

$$\sum_j \left|K_{ij}^u\right| = \sum_j \frac{\left|\left(\mathbf{\eta}_{(i)(j)} + \mathbf{\xi}_{(i)(j)}\right) \cdot \mathbf{e}\right|}{\left|\mathbf{\eta}_{(i)(j)} + \mathbf{\xi}_{(i)(j)}\right|} \frac{4\delta\Lambda_{(i)(j)}^2}{\left|\mathbf{\xi}_{(i)(j)}\right|^3} \left(A_u + \frac{B_u}{\lambda_{(i)(j)}^3} + 10D_u \frac{1}{\lambda_{(i)(j)}^6}\right) \tag{93c}$$

in which $\mathbf{e}$ is the unit vector along the x and y direction. The elements of stiffness matrix of each loading can be determined from the summation given in Eq. (93a), Eq. (93b) and Eq. (93c), respectively. Note that the densities associated with a specific material point are identical in all directions of the coordinate frame, and it makes them frame invariant.

As explained by Underwood [43], by utilizing the lowest frequency of the system, the damping coefficient can be achieved. Also, by using Rayleigh's quotient, the lowest frequency can be determined as

$$\omega = \sqrt{\dfrac{\mathbf{U}^T \mathbf{K} \mathbf{U}}{\mathbf{U}^T \mathbf{D} \mathbf{U}}} \; . \tag{94}$$

However, the values of density matrix in Eq. (91) could be large, and it makes it difficult to calculate the denominator of Eq. (94). This problem can be solved by rewriting at the nth iteration as

$$\ddot{\mathbf{U}}^n \left(\mathbf{X}, t^n \right) + c^n \dot{\mathbf{U}}^n \left(\mathbf{X}, t^n \right) = \mathbf{D}^{-1} \mathbf{F}^n \left(\mathbf{U}^n, \mathbf{U}'^n, \mathbf{X}, \mathbf{X}' \right). \tag{95}$$

The damping coefficient in Eq. (95) can be written by utilizing Eq. (94) for each time iteration as

$$c^n = 2 \sqrt{\left(\left(\mathbf{U}^n \right)^T {}^1\mathbf{K}^n \mathbf{U}^n \right) \Big/ \left(\left(\mathbf{U}^n \right)^T \mathbf{U}^n \right)} \; , \tag{96}$$

where ${}^1\mathbf{K}^n$ is the diagonal "local" stiffness matrix which is expressed as

$${}^1 K_{ii}^n = \left(F_i^n / \lambda_{ii} - F_i^{n-1} / \lambda_{ii} \right) \Big/ \left(\Delta t \, \dot{u}_i^{n-1/2} \right). \tag{97}$$

Another important concern when using a numerical technique is the convergence of the results. It is important to use optimum values of parameters to achieve sufficient accuracy within a suitable amount of computational time.

4.3 Boundary condition

In order to solve the peridynamic equation of motion, not only boundary conditions but also initial conditions on displacement and velocity are required. Since the PD equations of motion do not include any spatial derivatives, the boundary conditions are not necessary to obtain the solution of an integro-differential equation. In the peridynamic theory, the boundary conditions are imposed in the region of the fictitious boundary layers.

Macek and Silling [46] proposed that the extent of the fictitious boundary layer be determined equally to the horizon size, δ. By imposing constraints to the material points in the fictitious layer, the imposition of the displacement boundary conditions are implemented, and on the boundary surface, these conditions are satisfied explicitly. However, the value of the displacement in the fictitious layer can be approximated based on the linear extrapolation of the values in the real domain and the particular value of the boundary condition [47]. The imposition of the traction boundary conditions can be achieved through the use of body forces in the fictitious region, [40]. In the case of a two-dimensional analysis, the displacement constraints can be implemented by imposing a prescribed value of the displacement, U^* and V^* on the boundary. As shown in Fig. 4.3, along the boundary of the actual material region, $\mathcal{R}$, a fictitious boundary layer with depth δ is presented. Then, the boundary condition can be obtained through a fictitious region, $\mathcal{R}_f$.

The prescribed displacement boundary values of U^* and V^* can be imposed in the x and y direction in the fictitious region, $\mathcal{R}_f$ along the boundary of the material surface, $\mathcal{S}$ as

$$u_f(x_f, y_f, t+\Delta t) = 2U^*(x^*, y^*, t+\Delta t) - u(x, y, t) \ ,$$ (98a)

$$v_f(x_f, y_f, t+\Delta t) = 2V^*(x^*, y^*, t+\Delta t) - v(x, y, t) \ ,$$ (98b)

where, in the case of the prescribed values of $U^* = V^* = 0$ as shown in Fig. 4.3b, it represents the clamped boundary conditions. For instance, the displacement constraint U^* is only implemented, and in the other direction, there is no displacement $V^* = 0$ such as the case of planar loading. Then, the boundary condition can be imposed as

$$u_f(x_f, y_f, t+\Delta t) = 2U^*(x^*, y^*, t+\Delta t) - u(x, y, t) \ ,$$ (99a)

$$v_f(x_f, y_f, t+\Delta t) = v(x, y, t) \ ,$$ (99b)

As shown in Fig. 4.4, Eq. (99b) represents the roller support boundary conditions for the prescribed value, $U^* = 0$.
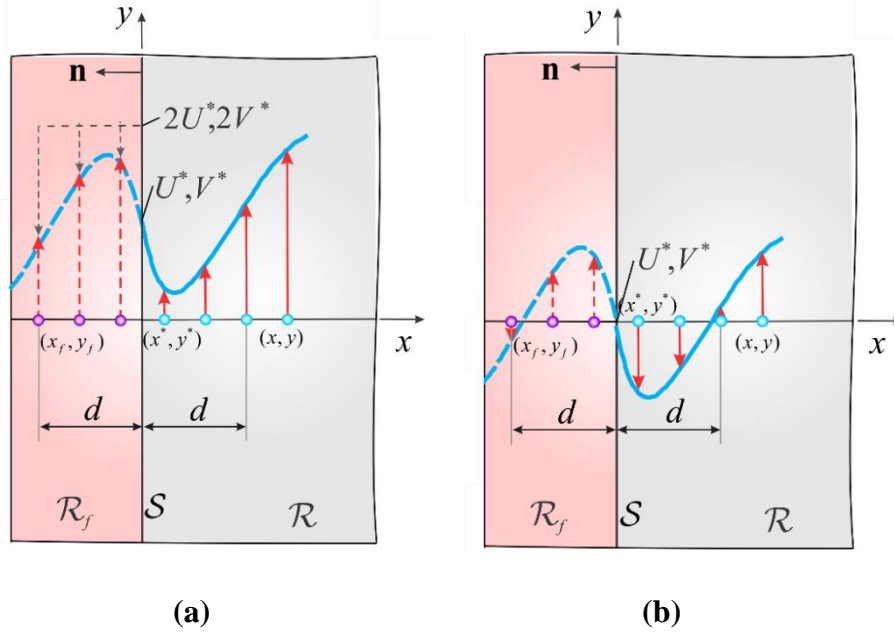
Figure 4.3. Imposing boundary condition on displacement components: (a) constant displacement components $u(x^*, y^*, t) = U^*$ and $v(x^*, y^*, t) = V^*$; (b) zero displacement components $u(x^*, y^*, t) = U^* = 0$ and $v(x^*, y^*, t) = V^* = 0$
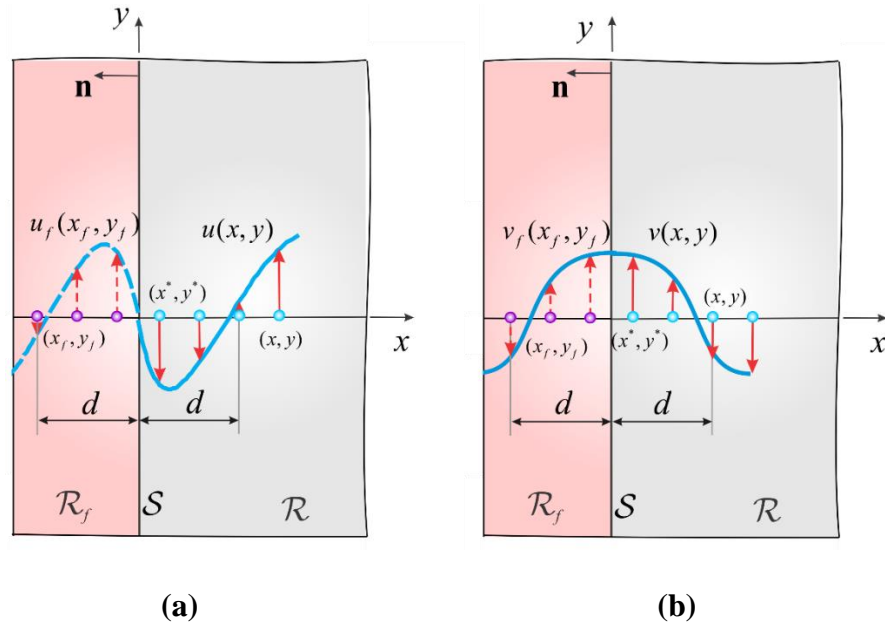
Figure 4.4. Imposing boundary condition on displacement components: (a) fixed in the normal direction $U^* = 0$; (b) free to move in the tangent direction

5. NUMERICAL RESULTS

In order to establish the validity of the PD force-stretch relations, Eqs. (44, 64, 82) for equibiaxial, planar and uniaxial loading conditions, first the deformation response of a square hyperelastic membrane is considered. The membrane is isotropic with Young's modulus and Possion's ratio of $E = 0.109$ GPa and $v = 0.5$, respectively. The PD force predictions for each loading condition are compared with finite element predictions by using ANSYS (a commercially available program) for a range of applied stretch ($\lambda = 1.5$, 2.0, 2.5 and 3.0). After verification, the same membrane is analyzed with a defect in the form a hole, rigid inclusion and a crack with a gap.

The geometry of the membrane is specified by its edge, $L = W = 0.5m$ and its thickness is $h = 0.01m$. The radius of a hole and a solid inclusion is $R = 0.08m$ and the crack length is $l = 0.16m$ with a gap of $w = 0.005m$. Convergence study is performed based on the grid size. For the analysis of equibiaxial and planar loading conditions, the PD model consists of 100 by 100 material (grid) points to discretize the membrane in the x- and y-directions, and a single layer of material points in the thickness direction. The spacing between the material points is $\Delta x = L/100$, and the corresponding horizon is specified as $\delta = 3.015\Delta x$. Also, the surface corrections are obtained by applying the stretch values $\lambda_x = 4$ and $\lambda_y = 4$ for equibiaxial, and $\lambda_x = 4$ and $\lambda_y = 1$ (no deformation) for planar loading in the x- and y- directions.

In the case of uniaxial loading, the membrane is discretized with 50 by 50 material points in the x- and y- directions resulting in $\Delta x = L/50$ spacing between thee material points.

Also, the horizon size is specified as $\delta = 9.015\Delta x$ in order to capture the presence of large contractions for which force densities at remote material points interact with each other. The number of material points is reduced in order to minimize the computational cost. The surface corrections are obtained by applying the stretch values $\lambda_x = 4$ and $\lambda_y = 4$ in the x- and y- directions.

The finite element discretization is achieved by 40 by 40, 50 by 50 and 15 by 15 for equibiaxial, planar and uniaxial loadings, respectively. The element, SHELL181 with Neo-Hookean material model is employed in the ANSYS model of the hyperelastic membrane. The force acting on the membrane is obtained by using the ANSYS command, PRNLD.

5.1. Equibiaxial loadings

As shown in Fig. 5.1, the membrane is subjected to equal stretch of $\lambda_1 = \lambda_2 = \lambda$ varying from 1.5 to 4 in increments of 0.5. The stretch is applied along the edge of the model in the x- and y- directions in the boundary regions. The resulting forces in the x- and y-directions are identical. Therefore, the PD force in the x- direction is compared with the ANSYS prediction as shown in Fig. 5.2. The maximum deviation between the PD and ANSYS predictions is about 3.0 %, for the applied stretch of $\lambda = 4.0$. The deviation decreases down to 1.75% for the applied stretch value of $\lambda = 1.5$.
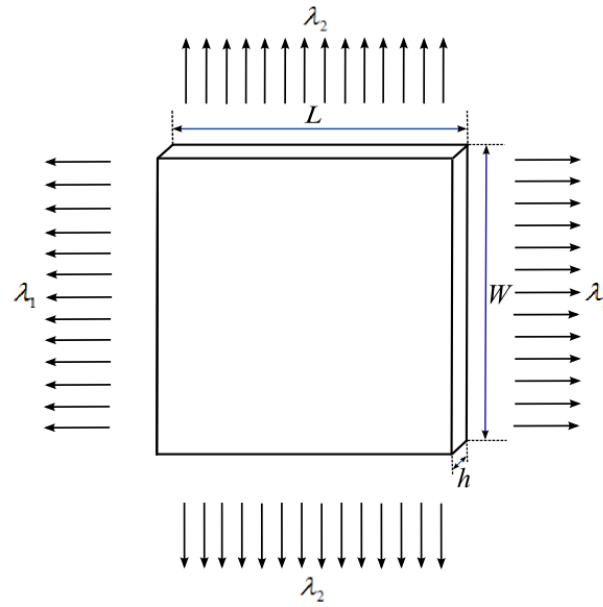
Figure 5.1. Geometric and loading for equibiaxial loading
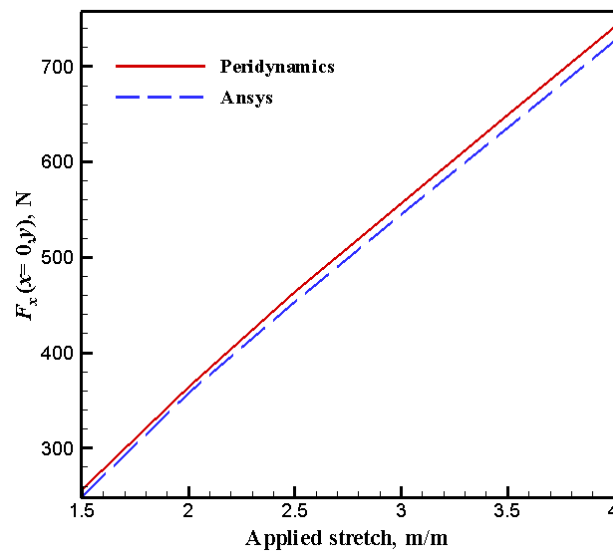
Figure 5.2. Force comparison of peridynamics and Ansys in the x direction for equibiaxial
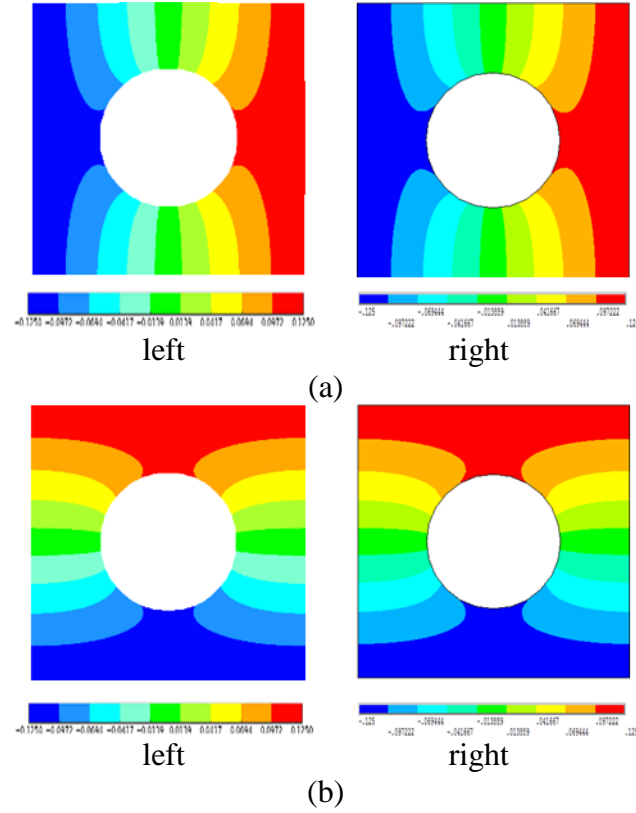
loading.

5.1.1 Membrane with a Hole

The hole is located at the center of the membrane as shown in Fig. 5.16. The stretch values

of $\lambda = 1.5$, 2.0, 2.5 and 3.0 are applied equally in the x- and y- directions. The

deformation contour plots are shown in Figs. 5.5 - 5.8. for each stretch value. As expected

by the definition of equibiaxial loading, the length and width increase while the thickness

decreases. Such deformation state satisfies incompressibility condition. Also, the radius

of the circle increases with increasing stretch value. Moreover, the shape of the circle

remains as circle in the deformed configurations. The peridynamics deformation contour

plots for all applied stretch values are in a good agreement with those of ANSYS as shown

in Figs. 5.5 - 5.8 .
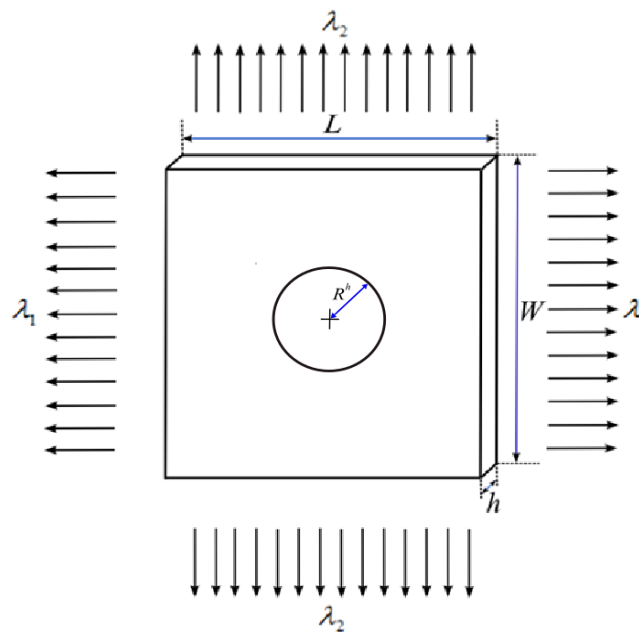
Figure 5.3. Geometric and loading with a hole for equibiaxial loading
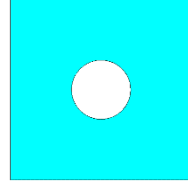
Figure 5.4. Undeformed membrane with a hole

left   right

(a)

left   right

(b)

Figure. 5.5. Displacement contours of membrane with a hole under equibiaxial loading for $\lambda = 1.5$ in deformed configuration: (a) x- directions, and (b) y-direction. (left: peridynamic and right: ANSYS)

<div align="center">left   right</div>
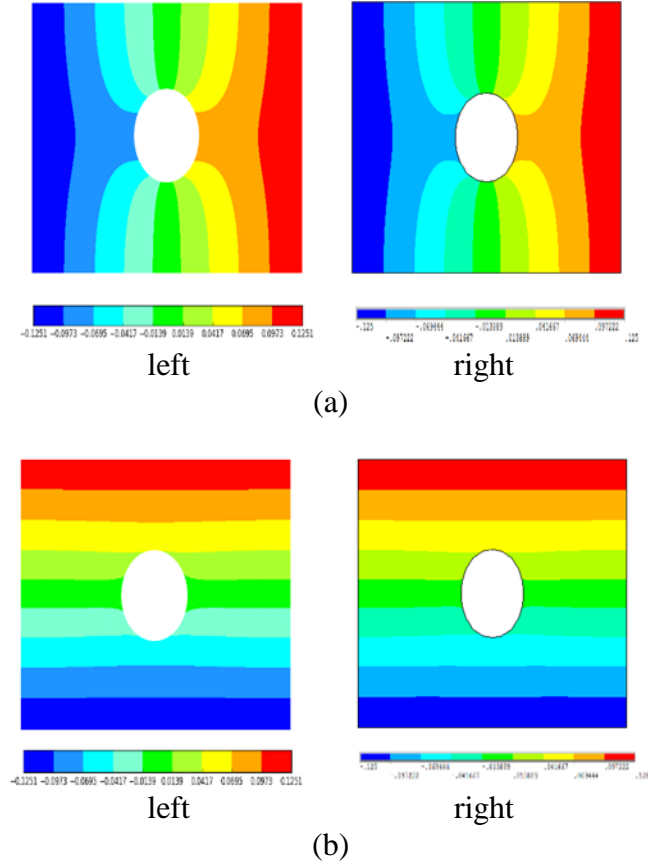
<div align="center">(a)</div>

<div align="center">left   right</div>

<div align="center">(b)</div>
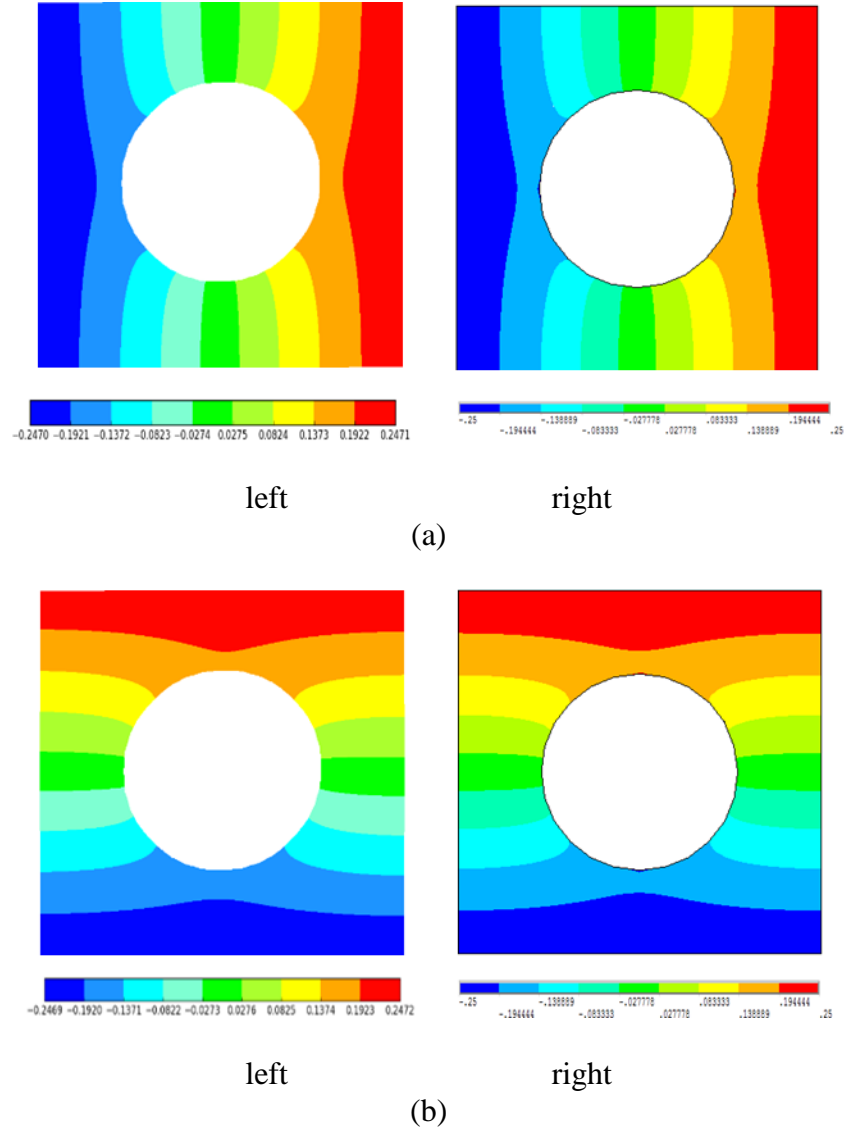
Figure 5.6. Displacement contours of membrane with a hole under equibiaxial loading for $\lambda = 2.0$ in deformed configuration: (a) x- directions, and (b) y-direction. (left: peridynamic and right: ANSYS)

left   right

(a)

left   right

(b)
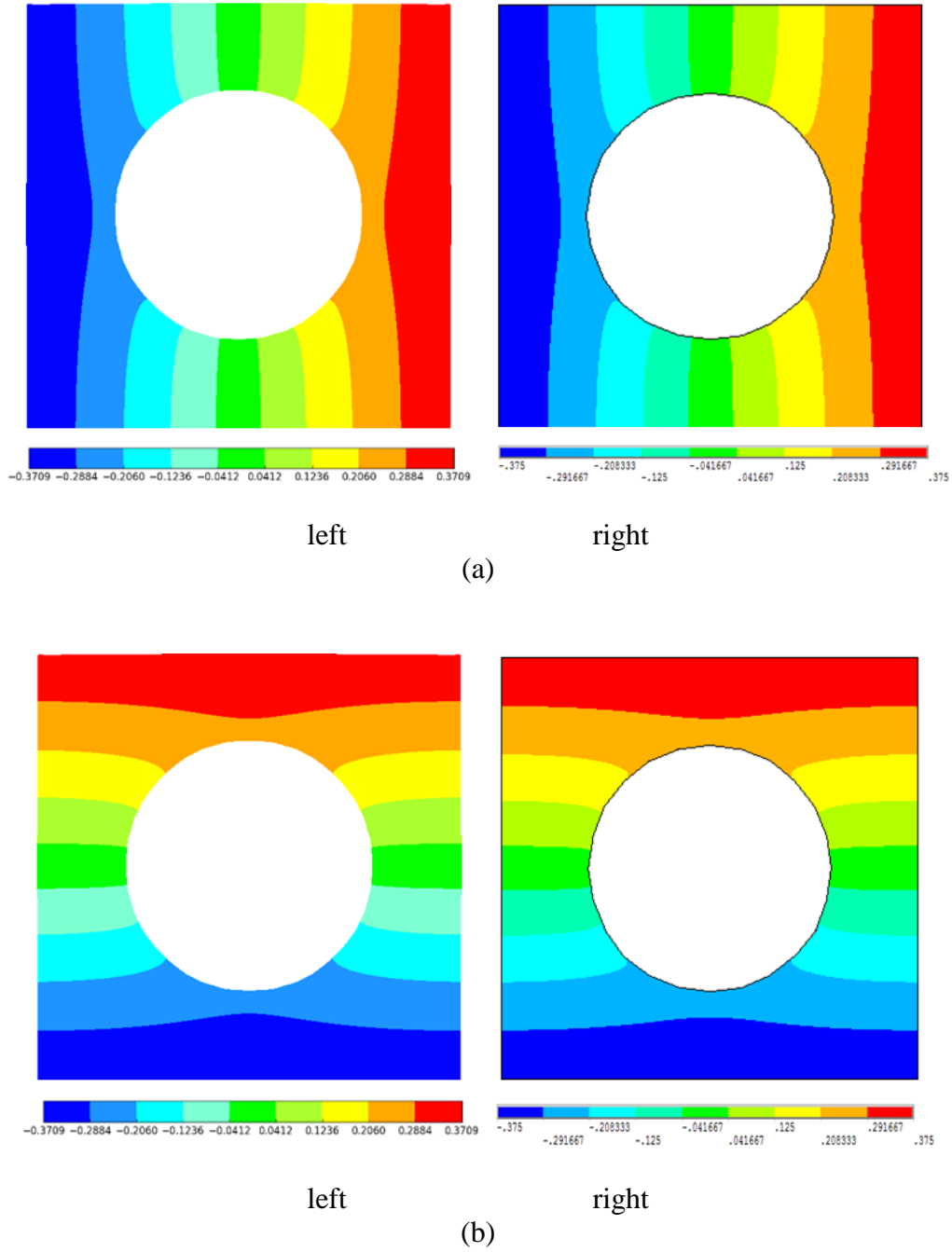
Figure 5.7. Displacement contours of membrane with a hole under equibiaxial loading for $\lambda = 2.5$ in deformed configuration: (a) x- directions, and (b) y-direction. (left: peridynamic and right: ANSYS)

left   right

(a)

left   right

(b)
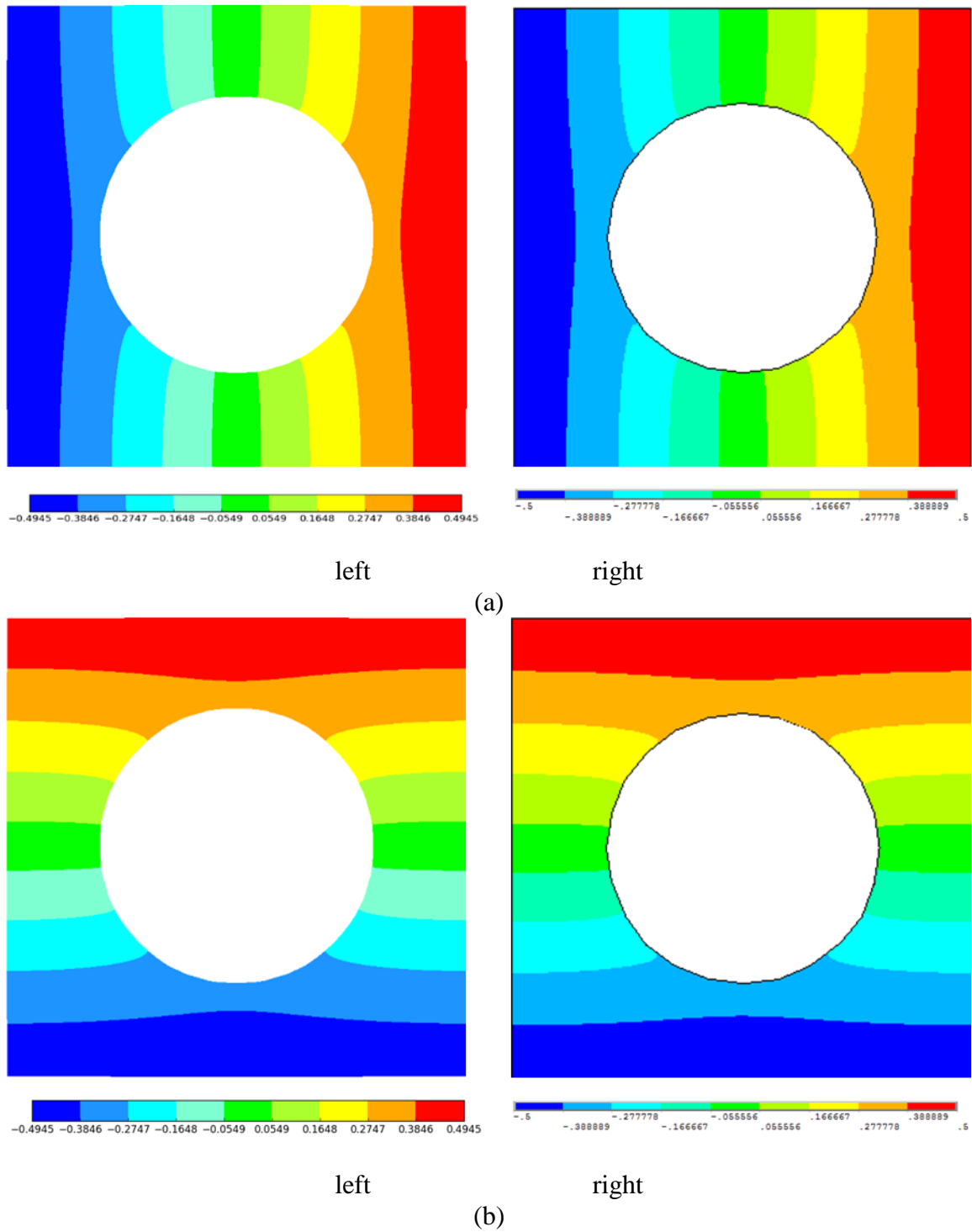
Figure 5.8. Displacement contours of membrane with a hole under equibiaxial loading for $\lambda = 3.0$ in deformed configuration: (a) x- directions, and (b) y-direction. (left: peridynamic and right: ANSYS)

5.1.2 Membrane with a Crack

The crack with a gap is located at the center of the membrane as shown in Fig. 5.9. The stretch values of $\lambda = 1.5,\ 2.0,\ 2.5$ and 3.0 are applied equally in the x- and y- directions. The deformation contour plots for each stretch value are shown in Figs. 5.11- 5.14. As expected, the length and width of the membrane increase while the thickness decreases in accordance with the incompressibility condition. Moreover, the crack gap increases with increasing applied stretch. The shape of the crack in the undeformed membrane is rectangular with a small width. However, after deformation, its shape becomes elliptical for the stretch values of $\lambda = 1.5,\ 2.0,\ 2.5$, and finally it becomes almost circular for the stretch value of $\lambda = 3.0$. ANSYS simulations also capture identical deformation patterns. As shown in Figs. 5.11 - 5.14, the displacement component in the y-direction appears to remain horizontal because the initial crack is aligned with the y-direction. However, the displacement component in the x-direction is affected by the local deformation of the crack surfaces. The peridynamic deformation contour plots compare well with those of ANSYS for all of the applied stretch values as shown in Fig. 5.11- 5.14.
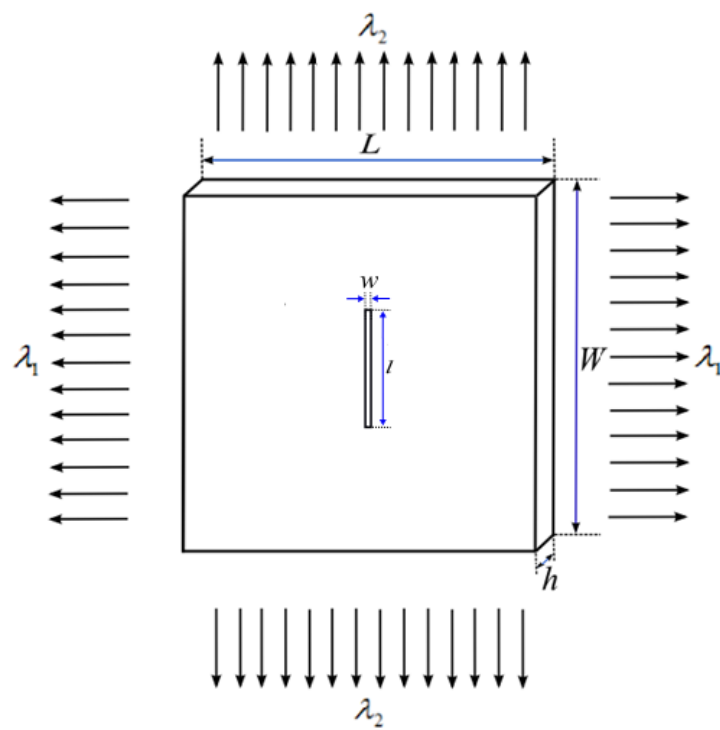
Figure 5.9. Geometric and loading with a Crack for equibiaxial loading
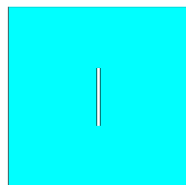
Figure 5.10. Undeformed membrane with a crack
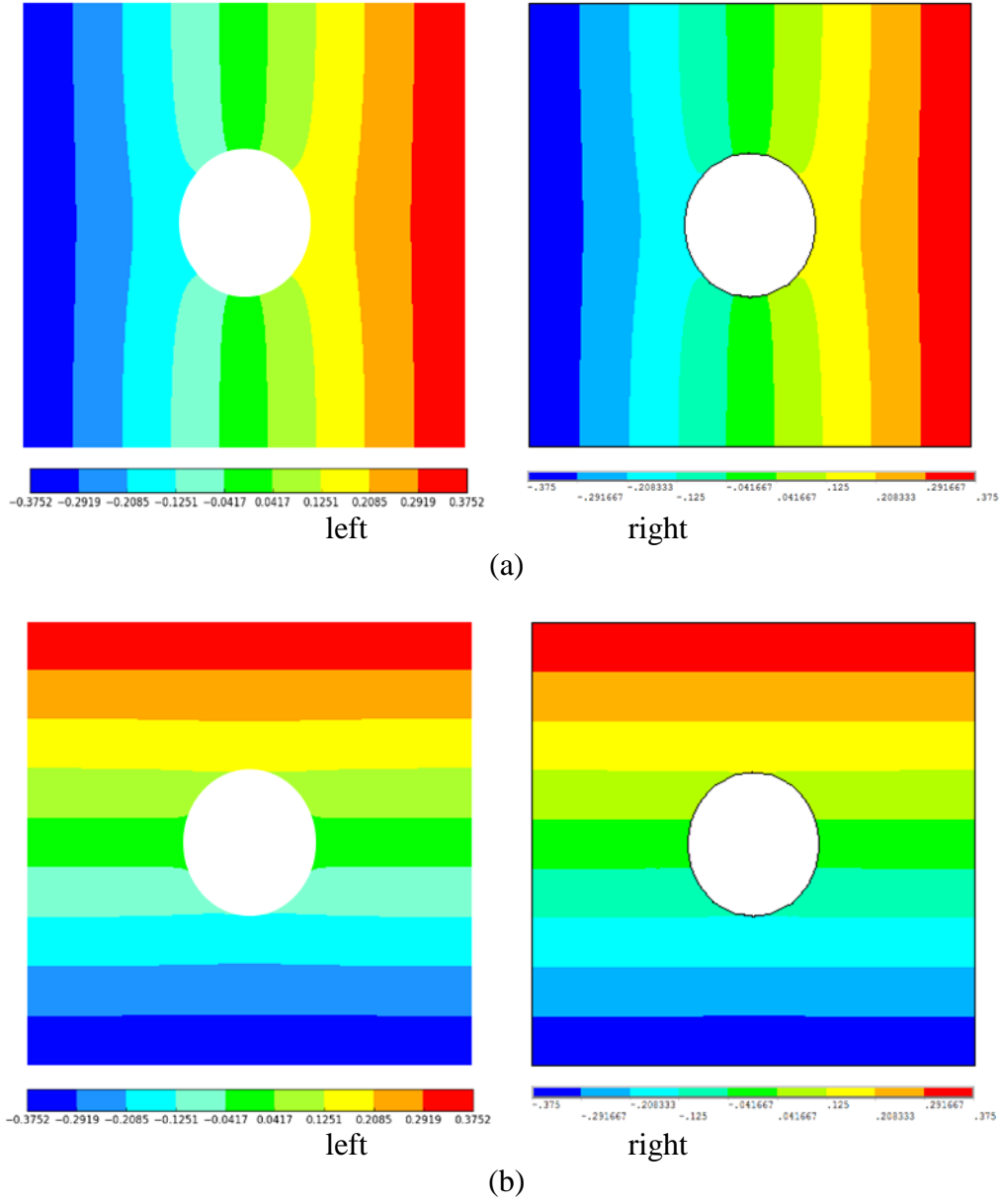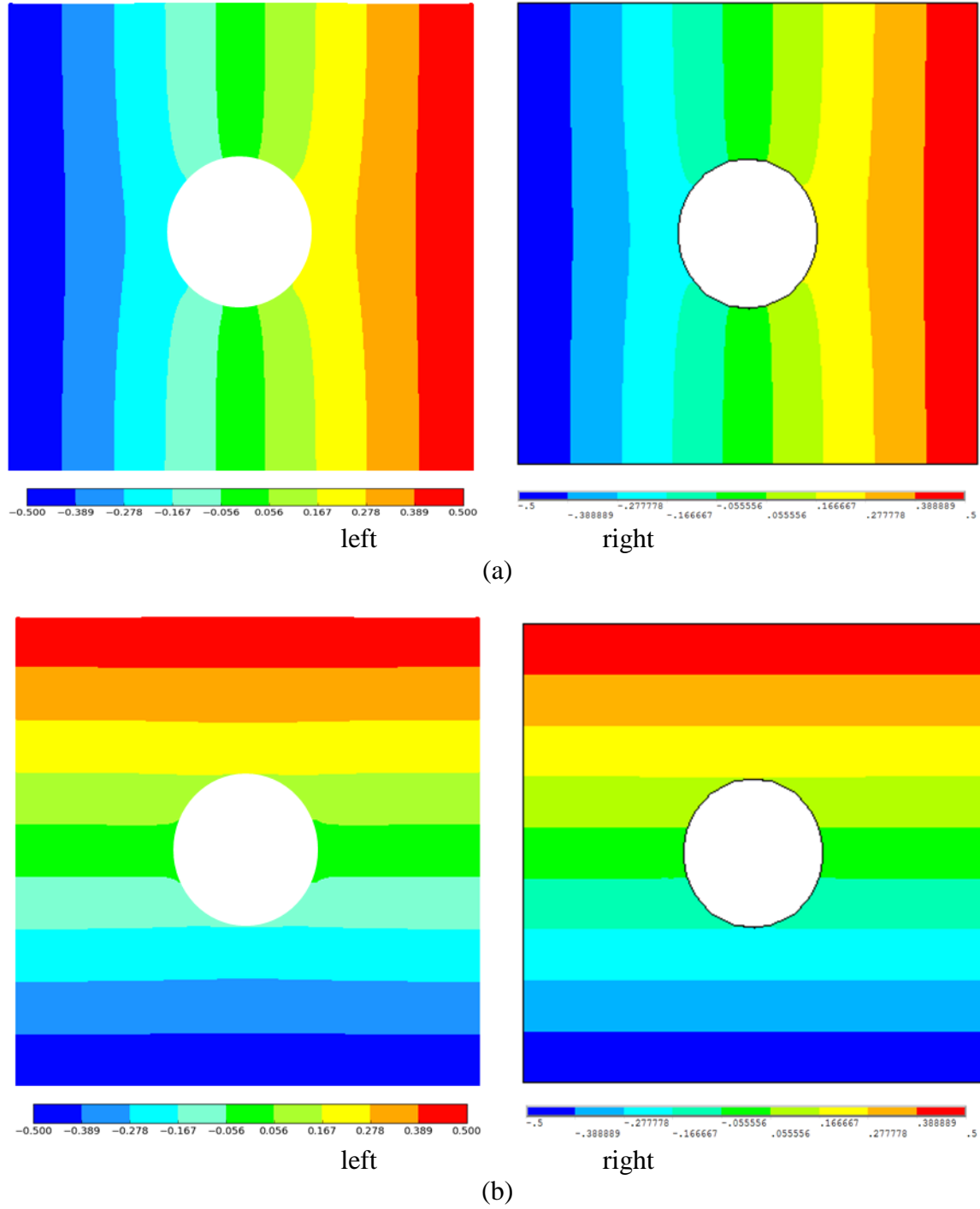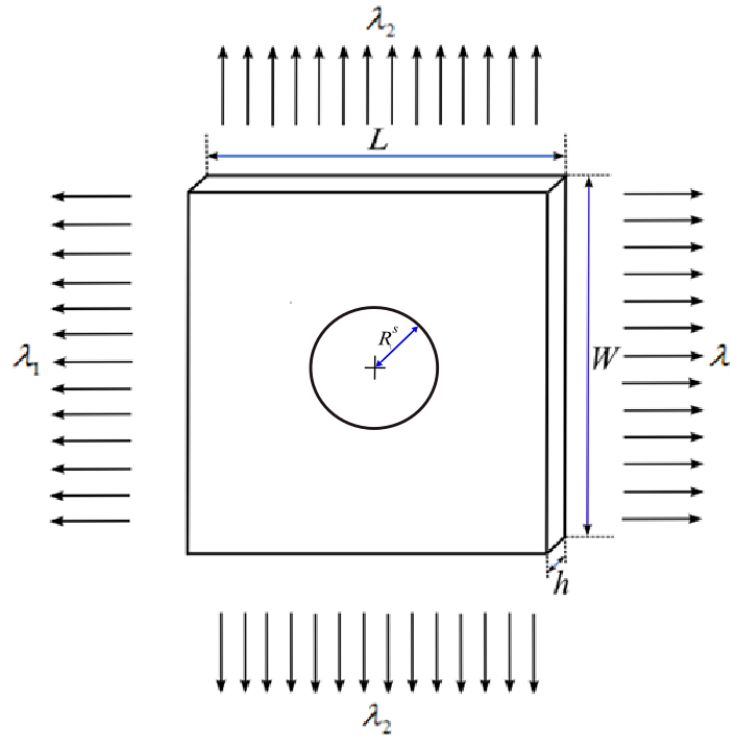
left right

(a)

left right

(b)

Figure 5.11. Displacement contours of membrane with a crack under equibiaxial loading for $\lambda = 1.5$ in deformed configuration: (a) x- directions, and (b) y-direction. (left: peridynamic and right: ANSYS)
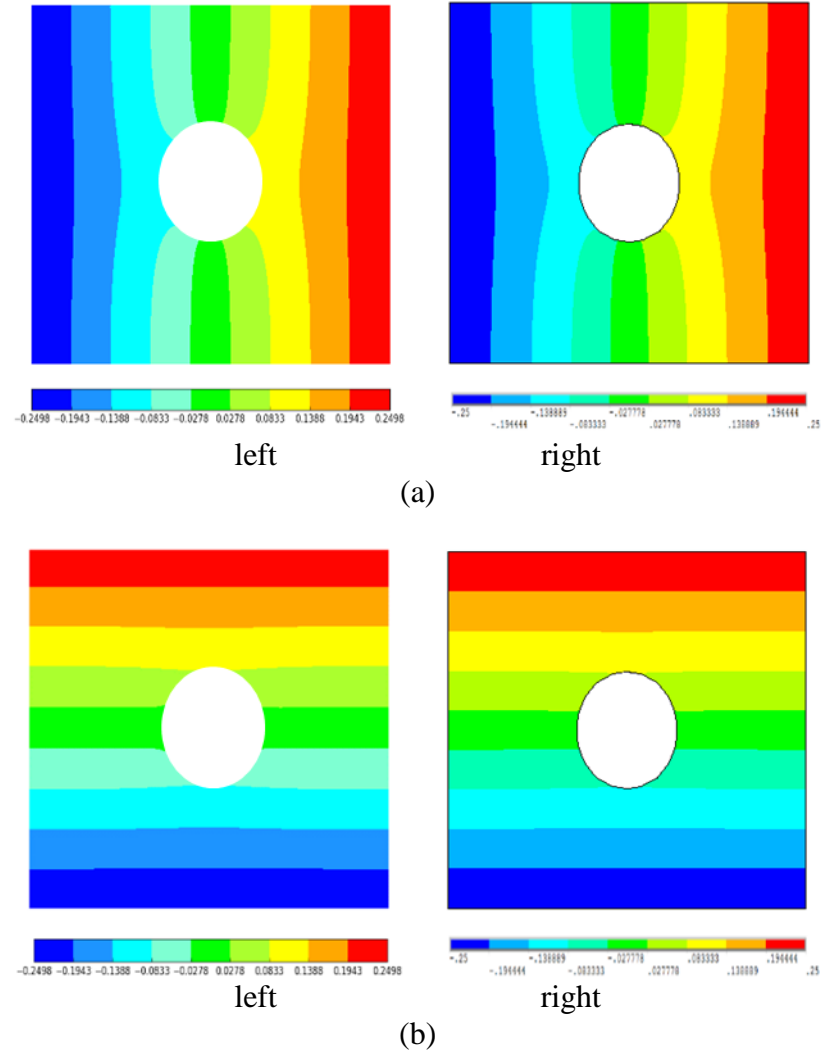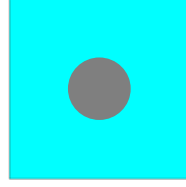
Figure 5.12 Displacement contours of membrane with a crack under equibiaxial loading for $\lambda = 2.0$ in deformed configuration: (a) x- directions, and (b) y-direction. (left: peridynamic and right: ANSYS)

left   right

(a)

left   right

(b)

Figure 5.13. Displacement contours of membrane with a crack under equibiaxial loading for $\lambda = 2.5$ in deformed configuration: (a) x- directions, and (b) y-direction. (left: peridynamic and right: ANSYS)

left   right

(a)

left   right

(b)

Figure 5.14. Displacement contours of membrane with a crack under equibiaxial loading for $\lambda = 3.0$ in deformed configuration: (a) x- directions, and (b) y-direction. (left: peridynamic and right: ANSYS)

5.1.3 Membrane with a Solid Inclusion

The solid inclusion with a radius of $R = 0.08m$ is located at the center of the plate as shown in Fig. 5.15. The stretch values of $\lambda = 1.5$, 2.0, 2.5 and 3.0 are applied equally in the x- and y- directions. The deformation contour plots are shown for each stretch value in Fig. 5.17-Fig. 5.20. Similar to the previous cases, the length and width of the membrane increase and the thickness decreases satisfying the incompressibility condition. Deformation contours indicate sharp gradients near the rigid inclusion. Because of the presence of symmetry, the deformation contours present the same variation in the x- and y- directions. As shown in Figs. 5.17 - 5.20, the comparisons of peridynamics predictions with those of ANSYS indicate good agreement for all values of applied stretch.

Figure 5.15. Geometric and loading with a solid inclusion for equibiaxial loading
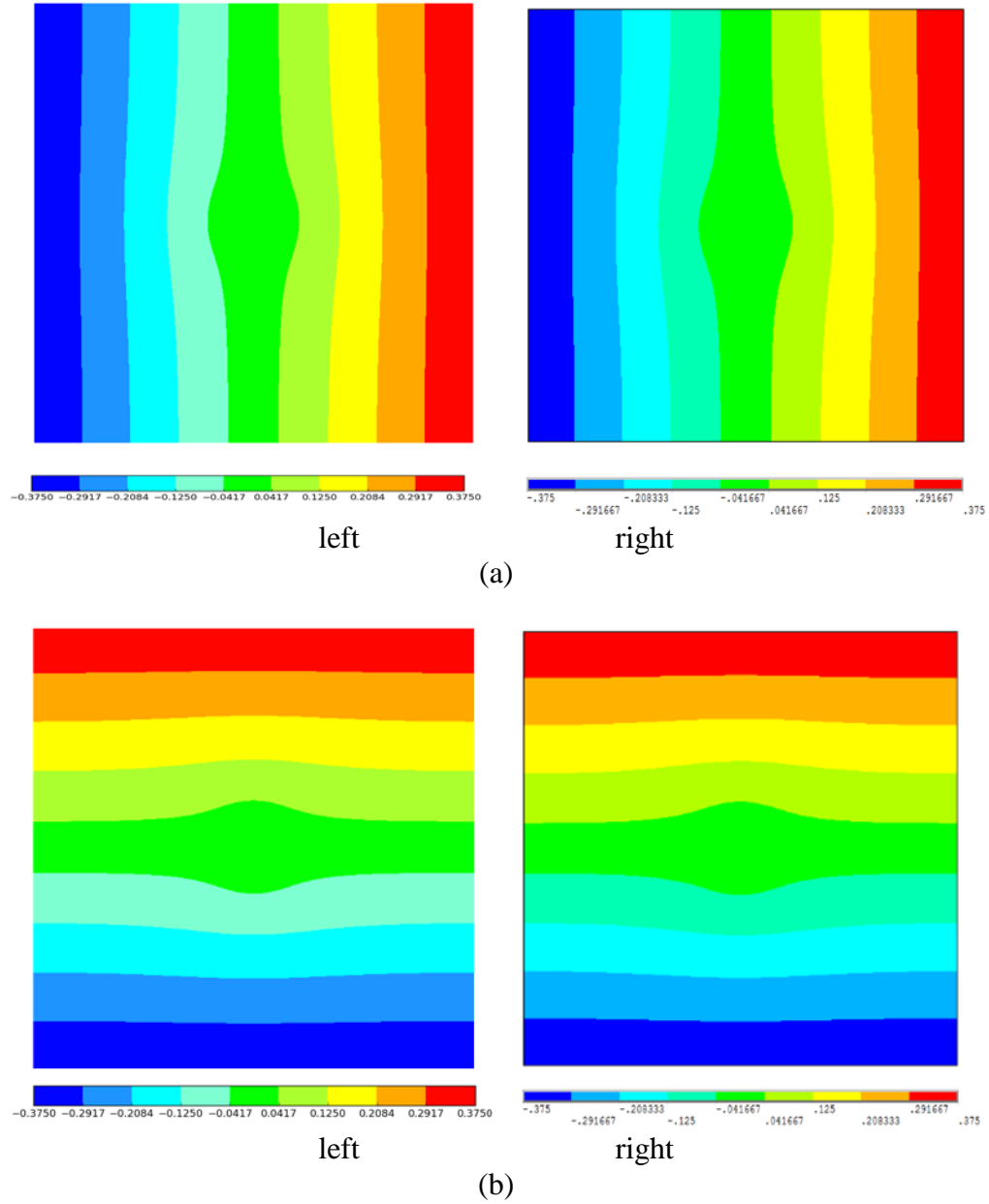
Figure 5.16. Undeformed membrane with a solid inclusion
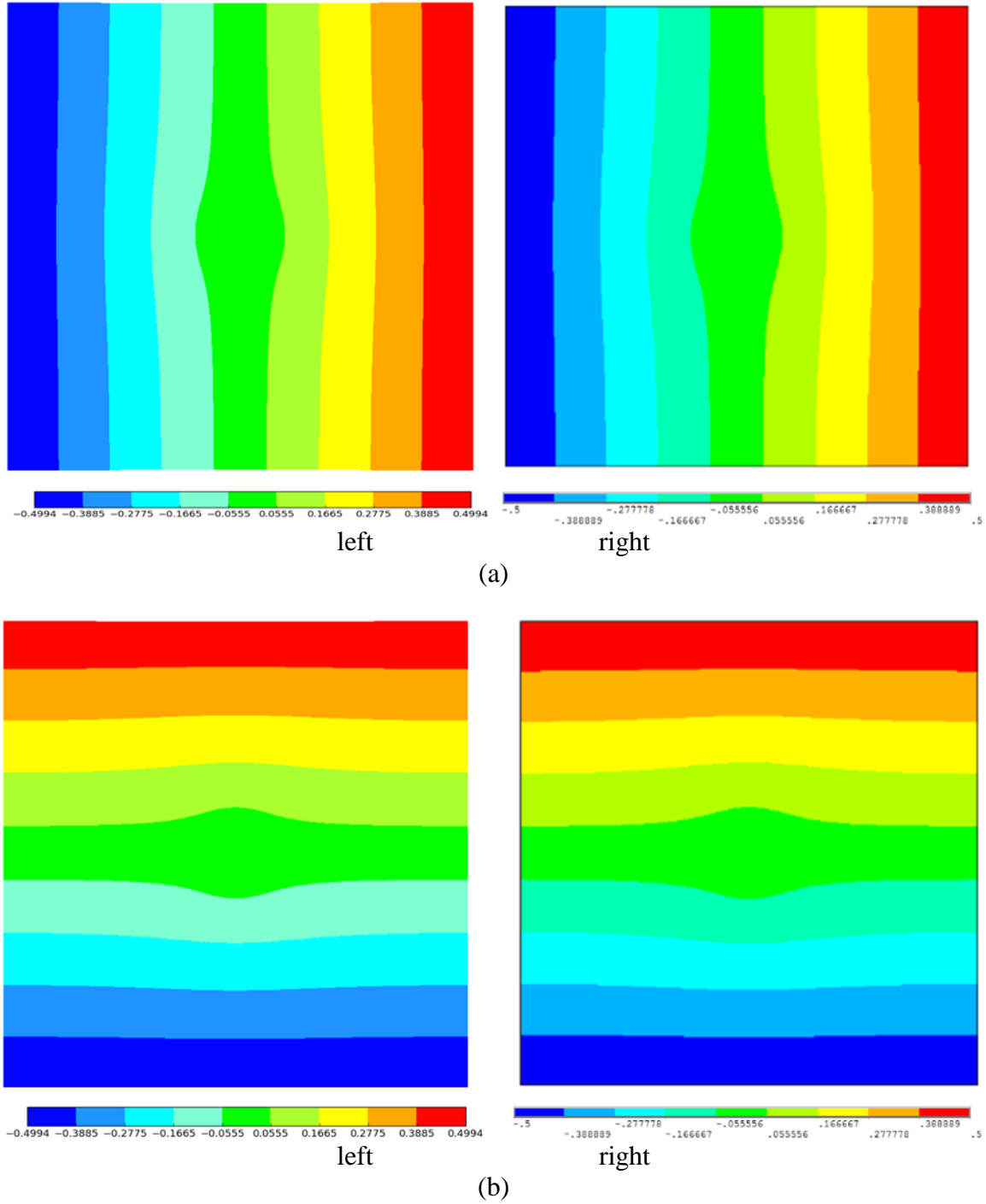

left right

(a)

left right

(b)
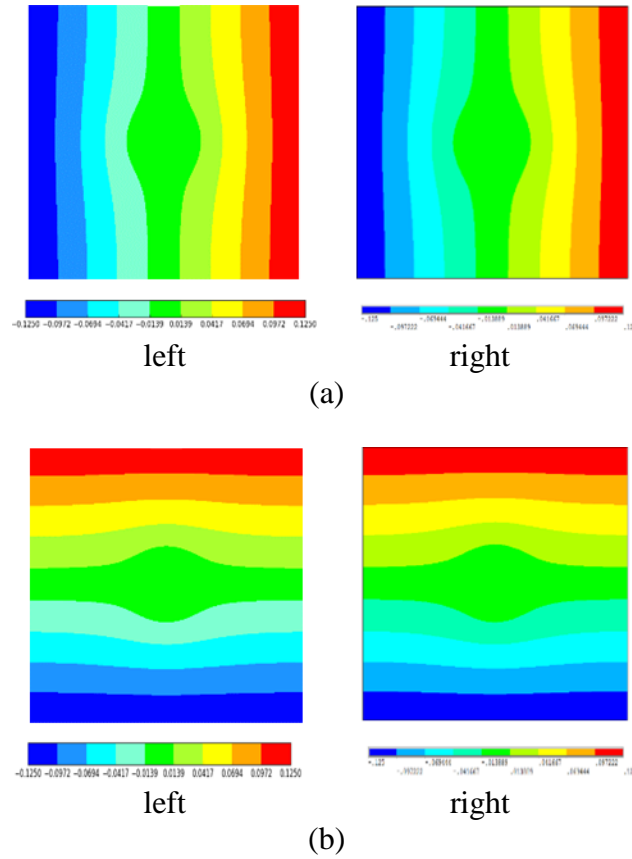
Figure 5.17. Displacement contours of membrane with a solid inclusion under equibiaxial loading for $\lambda = 1.5$ in deformed configuration: (a) x- directions, and (b) y-direction. (left: peridynamic and right: ANSYS)

left   right

(a)

left   right

(b)
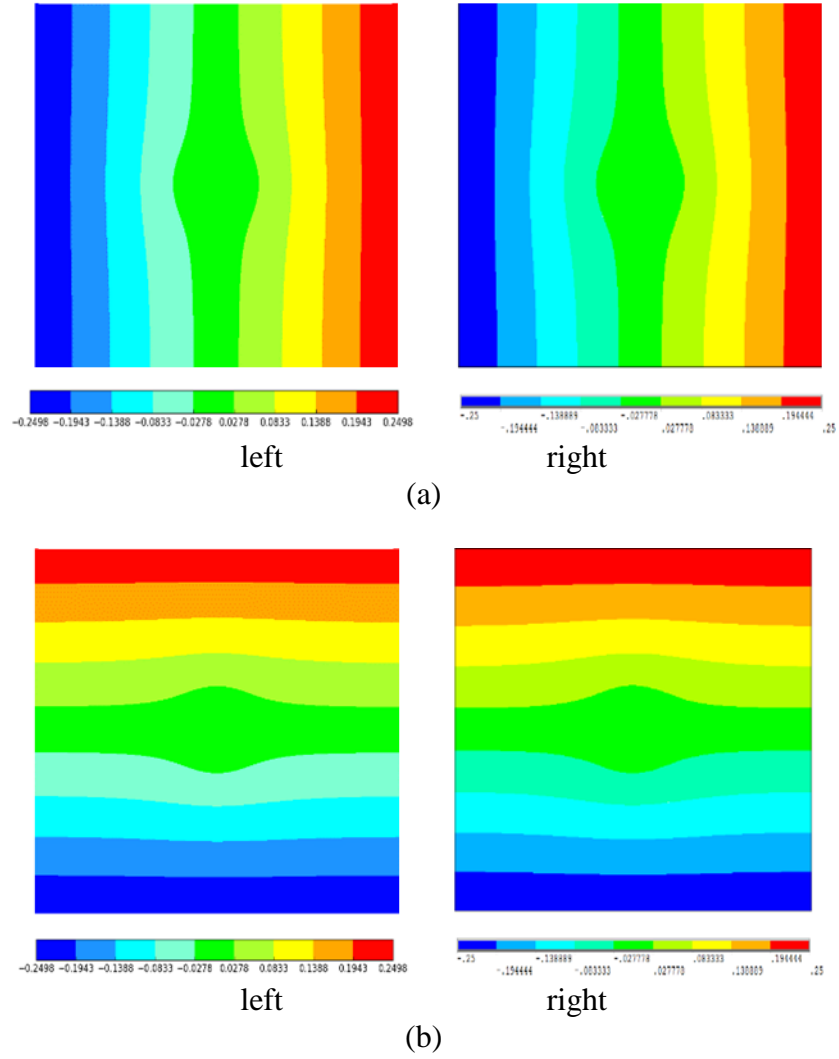
Figure 5.18. Displacement contours of membrane with a solid inclusion under equibiaxial loading for $\lambda = 2.0$ in deformed configuration: (a) x- directions, and (b) y-direction. (left: peridynamic and right: ANSYS)

left right

(a)

left right

(b)

Figure 5.19. Displacement contours of membrane with a solid inclusion under equibiaxial loading for $\lambda = 2.5$ in deformed configuration: (a) x- directions, and (b) y-direction. (left: peridynamic and right: ANSYS)

left   right

(a)

left   right

(b)

Figure 5.20. Displacement contours of membrane with a solid inclusion under equibiaxial loading for $\lambda = 3.0$ in deformed configuration: (a) x- directions, and (b) y-direction. (left: peridynamic and right: ANSYS)

5.2. Planar loadings

As shown in Fig. 5.21, the membrane is subjected to a stretch of λ in the x-direction, which is varied from 1.5 to 4 in increments of 0.5. These stretch values are applied along the right and left edges of the membrane. The upper and lower edges are on roller supports, thus constrained from deformation in the y-direction. The comparison of the PD and ANSYS force predictions in the x- direction is shown in Fig. 5.22, and the deviation remains about 5% .
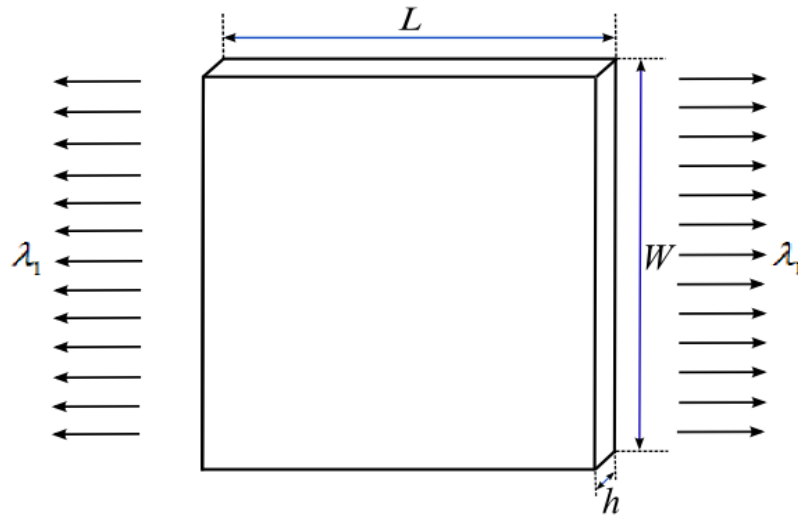
Figure 5.21. Geometric and loading for planar loading
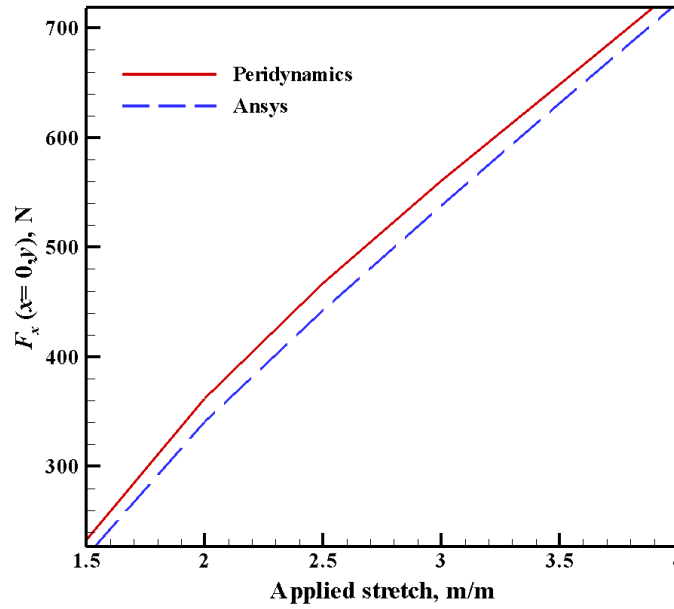
Figure 5.22. Force comparison of peridynamics and Ansys in the x direction for planar loading.

5.2.1 Membrane with a Hole

The stretch values of $\lambda = 1.5$, 2.0, 2.5 and 3.0 are applied in the x-direction. The deformation contour plots are shown each stretch value in Figs. 5.25 - 5.28. As expected with the planar loading conditions and constraints, the length increases and the thickness decreases. The thickness decreases inversely proportional to the length because there is no deformation in the width direction. Therefore, the deformation contours plots are presented only in the x-direction as shown in Figs. 5.25 - 5.28. Moreover, the hole becomes an ellipse whose major axis increases with increasing applied stretch. As shown in Figs. 5.25- 5.28, the peridynamics predictions of displacement variations are in good agreement with those of ANSYS for all values of applied stretch.
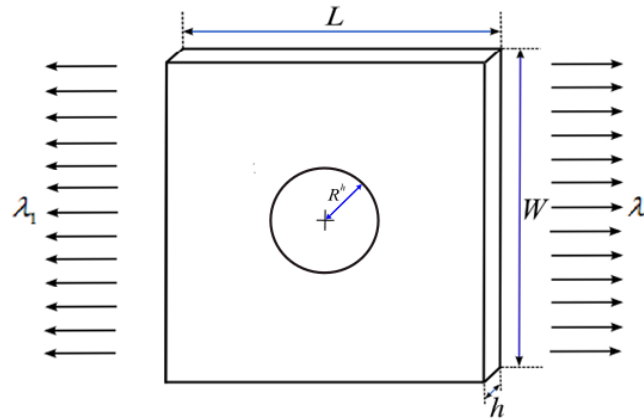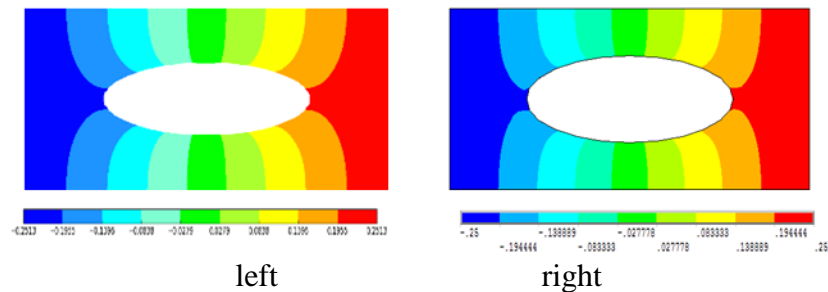
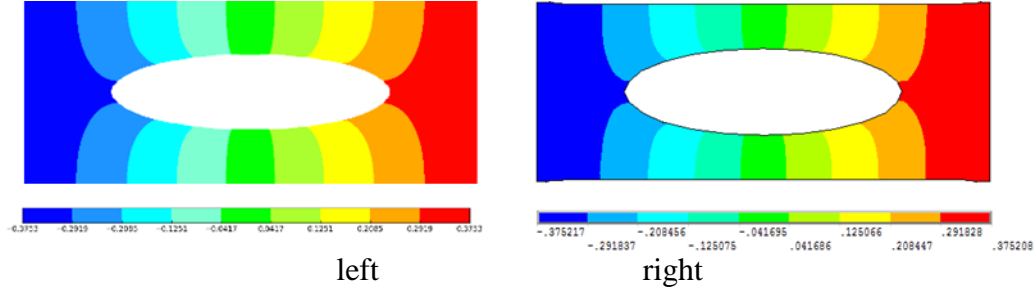**Figure 5.23.** Geometric and loading with a hole under planar loading
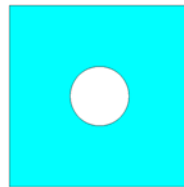
Figure 5.24. Undeformed membrane with a hole

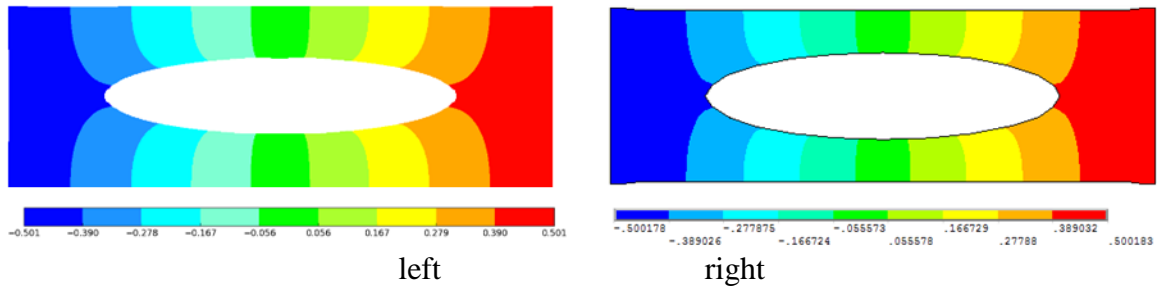left   right
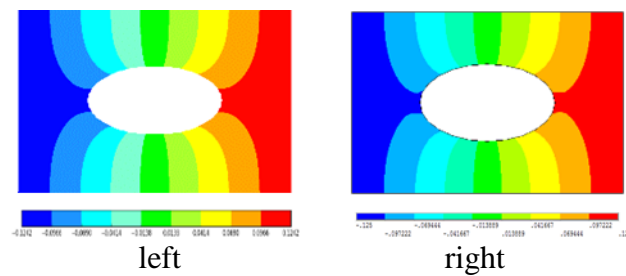
Figure 5.25. Displacement contours in the x- directions of membrane with a hole under planar loading for $\lambda = 1.5$ in deformed configuration(left: peridynamic and right: ANSYS)

left   right

Figure 5.26. Displacement contours in the x- directions of membrane with a hole under planar loading for $\lambda = 2.0$ in deformed configuration(left: peridynamic and right: ANSYS)
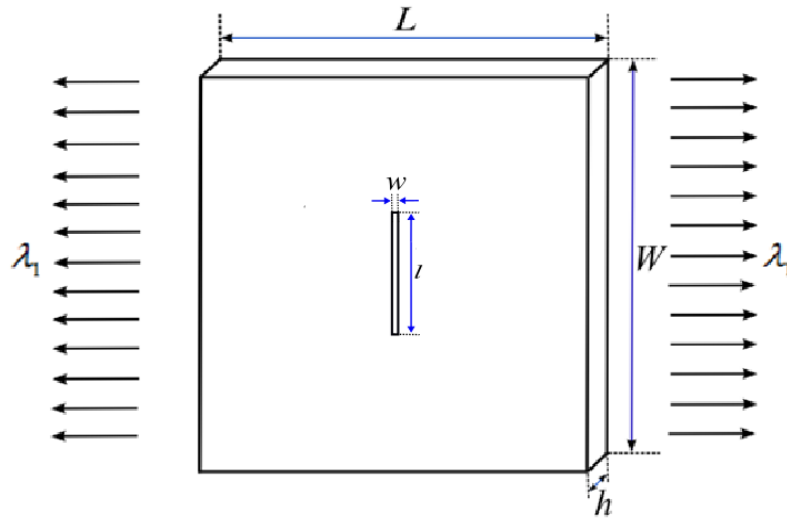
left   right

Figure 5.27. Displacement contours in the x- directions of membrane with a hole under planar loading for $\lambda = 2.5$ in deformed configuration(left: peridynamic and right: ANSYS)
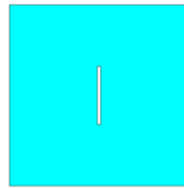

left   right

Figure 5.28. Displacement contours in the x- directions of membrane with a hole under planar loading for $\lambda = 3.0$ in deformed configuration(left: peridynamic and right: ANSYS)

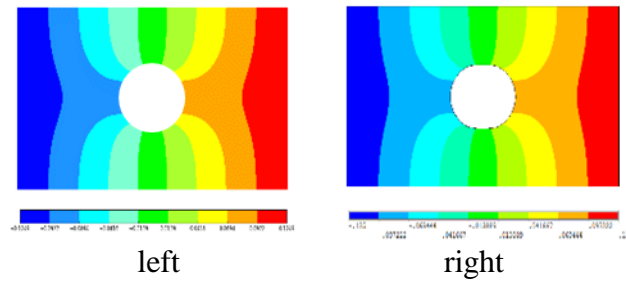### 5.2.2 Membrane with a Crack

For stretch values of $\lambda = 1.5,\ 2.0,\ 2.5$ and 3.0 applied in the x- direction, the deformation contour plots are shown in Figs. 5.31 - 5.34. Similar to the case of a hole, the thickness decreases inversely proportional to the length of the membrane. Also, the gap increases as the larger stretch is applied. However, in the planar loading, unlike the equibiaxial loading, crack shape becomes elliptical for increasing stretch values. Both PD and ANSYS predict similar deformations, and their comparison indicate good agreement as shown in Figs. 5.31- 5.34.
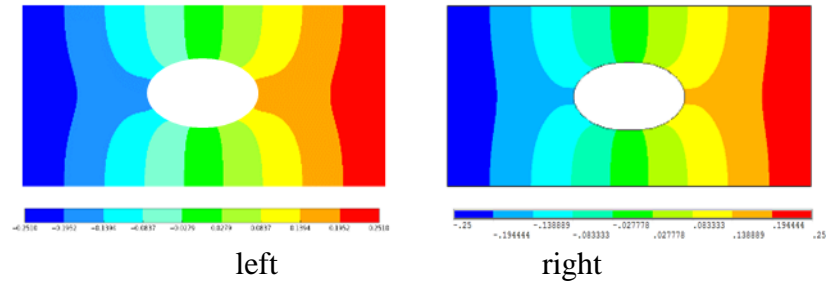
**Figure 5.29.** Geometric and loading with a crack for planar loading

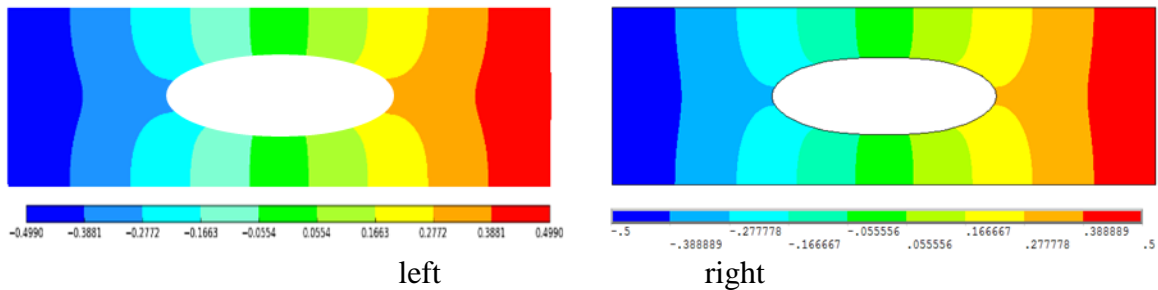**Figure 5.30.** Undeformed membrane with a crack

left   right

Figure 5.31. Displacement contours in the x- directions of membrane with a crack under planar loading for $\lambda = 1.5$ in deformed configuration(left: peridynamic and right: ANSYS)

<center>left   right</center>

Figure 5.32. Displacement contours in the x- directions of membrane with a crack under planar loading for $\lambda = 2.0$ in deformed configuration(left: peridynamic and right: ANSYS

<center>left   right</center>
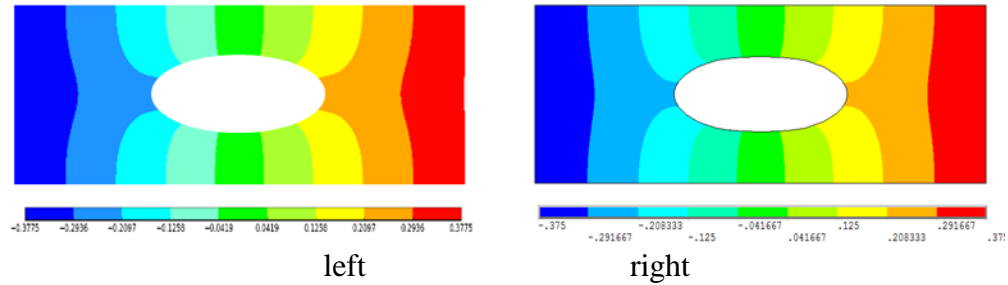
Figure 5.33. Displacement contours in the x- directions of membrane with a crack under planar loading for $\lambda = 2.5$ in deformed configuration(left: peridynamic and right: ANSYS
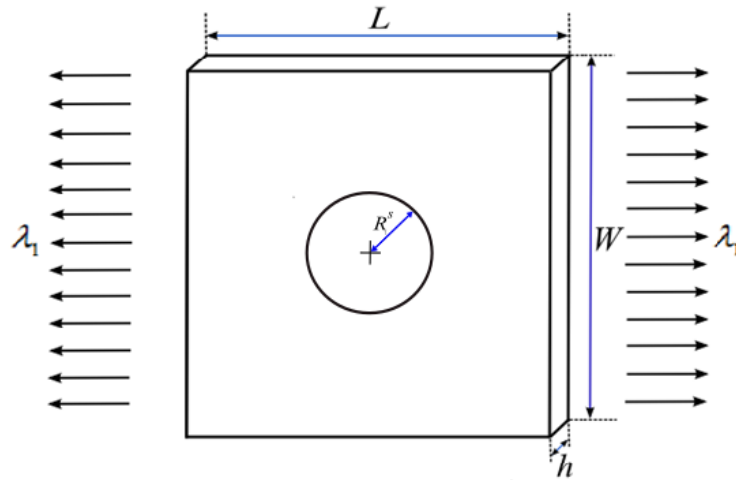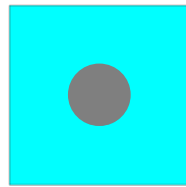

<center>left   right</center>

Figure 5.34. Displacement contours in the x- directions of membrane with a crack under planar loading for $\lambda = 3.0$ in deformed configuration(left: peridynamic and right: ANSYS
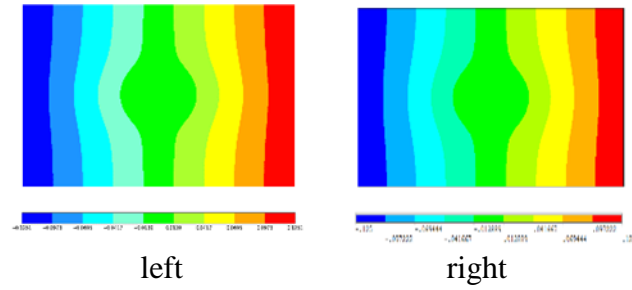
5.2.3 Membrane with a Solid Inclusion

The stretch values of $\lambda = 1.5$, 2.0, 2.5 and 3.0 are applied in the x- direction. The deformation contour plots are shown for each stretch values in Figs. 5.37- 5.40. The thickness decreases inversely proportional to the length due to the incompressibility condition. As expected, the deformation contour lines present a nonlinear behavior in the x-direction, there exists no deformation in the y-direction. As shown in Figs. 5.37- 5.40, the peridynamics deformation contour plots compare well those of ANSYS predictions.

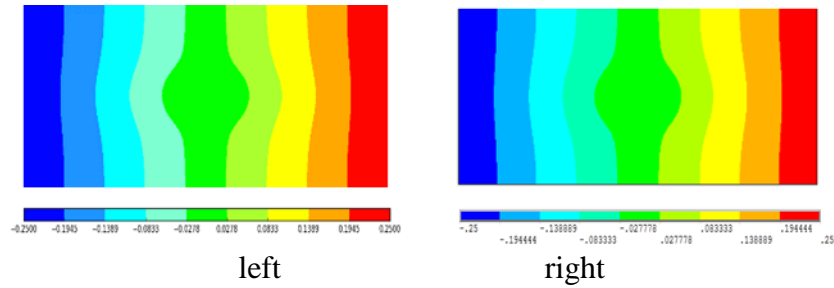**Figure 5.35.** Geometric and loading with a crack for planar loading

Figure 5.36. Undeformed membrane with a solid inclusion

left   right

Figure 5.37. Displacement contours in the x- directions of membrane with a rigid inclusion under planar loading for $\lambda = 1.5$ in deformed configuration (left: peridynamic and right: ANSYS

left   right

Figure 5.38. Displacement contours in the x- directions of membrane with a rigid inclusion under planar loading for $\lambda = 2.0$ in deformed configuration (left: peridynamic and right: ANSYS

left   right
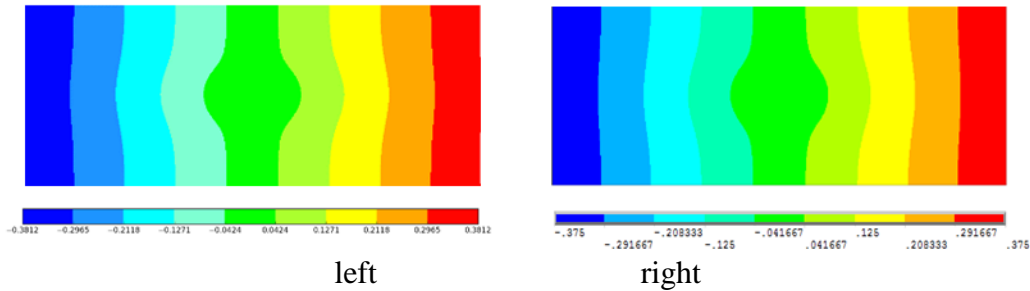
Figure 5.39. Displacement contours in the x- directions of membrane with a rigid inclusion under planar loading for $\lambda = 2.5$ in deformed configuration (left: peridynamic and right: ANSYS

left   right

Figure 5.40. Displacement contours in the x- directions of membrane with a rigid inclusion under planar loading for $\lambda = 3.0$ in deformed configuration (left: peridynamic and right: ANSYS
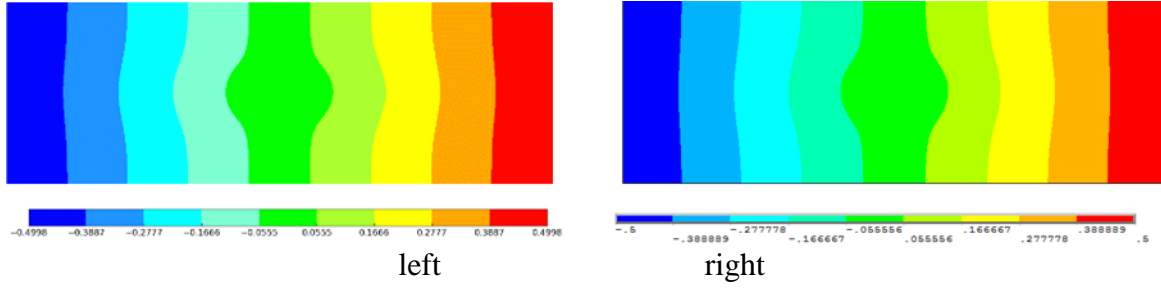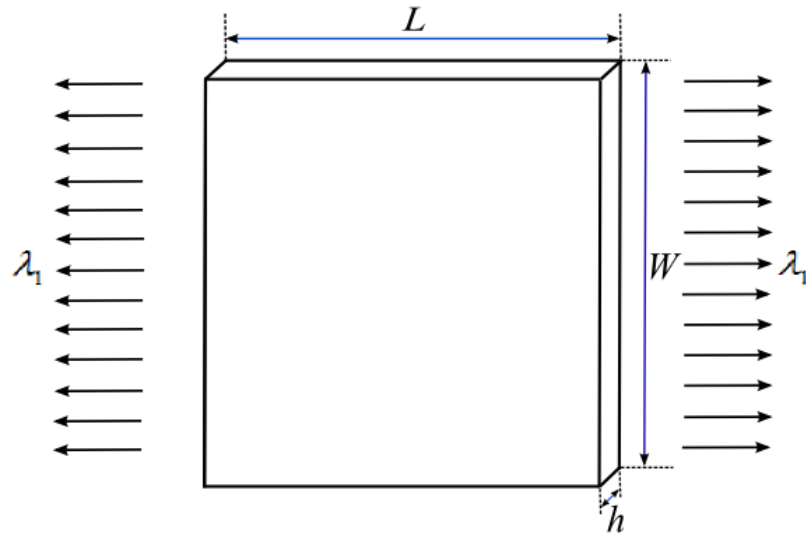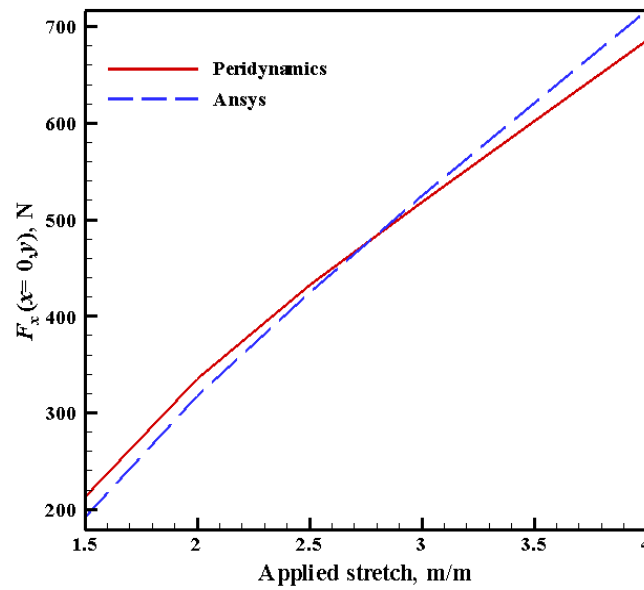
5.3. Uniaxial loadings

As shown in Fig. 5.41, the membrane is subjected to a stretch of λ in the x- direction, which is varied from 1.5 to 4 in increments of 0.5. Similar to the planar loading case, these stretch values are applied along the left and right edges of the membrane. The membrane is not constrained in the y-direction. As a result, the force in the y- direction is zero. Also, the membrane width and thickness contract simultaneously as expected because of the incompressibility condition. The PD force prediction in the x-direction is compared with ANSYS as shown in Fig. 5.42. The comparison indicates good agreement, and the deviation between the two varies between 1.5 % to 10 %. The PD force prediction is slightly larger than ANSYS predictions for stretch values less than 3, and higher subsequent values.
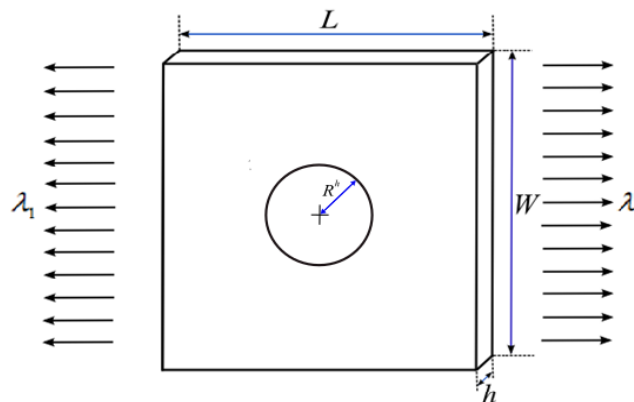
Figure 5.41. Geometric and loading for uniaxial loading

Figure 5.42. Force comparison of peridynamics and Ansys in the x direction for uniaxial loading.

5.3.1 Membrane with a Hole

For applied stretch values of $\lambda = 1.5,\ 2.0,\ 2.5$ and 3.0 in the x- direction, the deformation contour plots are shown in Figs. 5.45 - 5.48. As expected, the circular hole becomes elliptical in shape for increasing stretch values. The comparison of PD deformation contours with those of ANSYS indicates good agreement. It captures the effect interaction of free surface of the hole and unloaded edges on the deformation field.

Figure 5.43. Geometric and loading with a hole for uniaxial loading
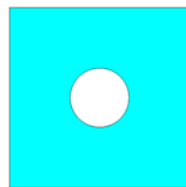
Figure 5.44. Undeformed membrane with a hole

left   right

(a)

left   right

(b)
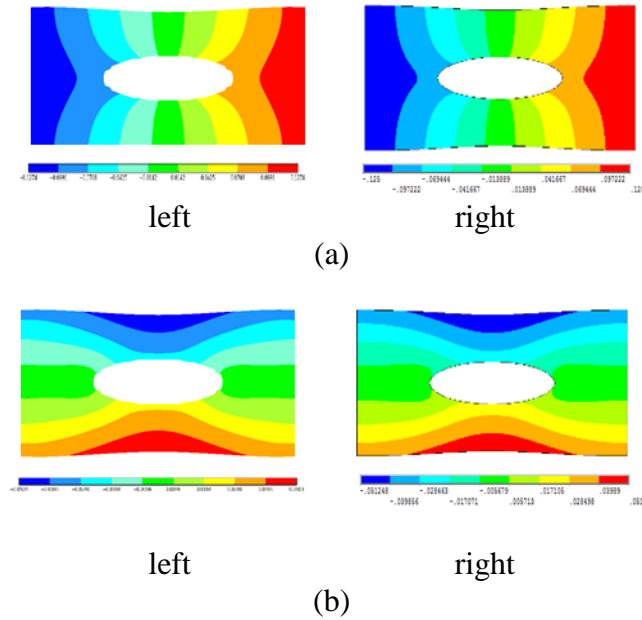
Figure 5.45. Displacement contours of membrane with a hole under uniaxial loading for $\lambda = 1.5$ in deformed configuration: (a) x- directions, and (b) y-direction. (left: peridynamic and right: ANSYS)

left   right

(a)

left   right

(b)
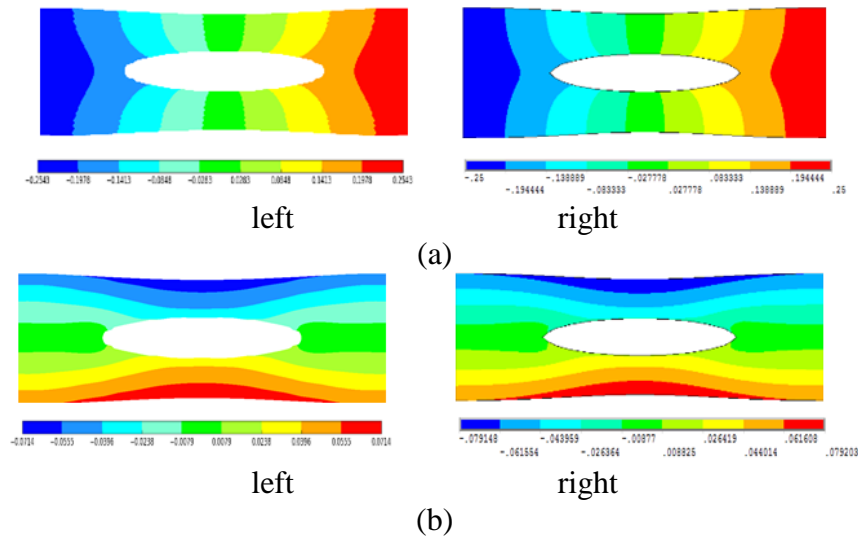
Figure 5.46. Displacement contours of membrane with a hole under uniaxial loading for $\lambda = 2.0$ in deformed configuration: (a) x- directions, and (b) y-direction. (left: peridynamic and right: ANSYS)

left — right

(a)

left — right

(b)
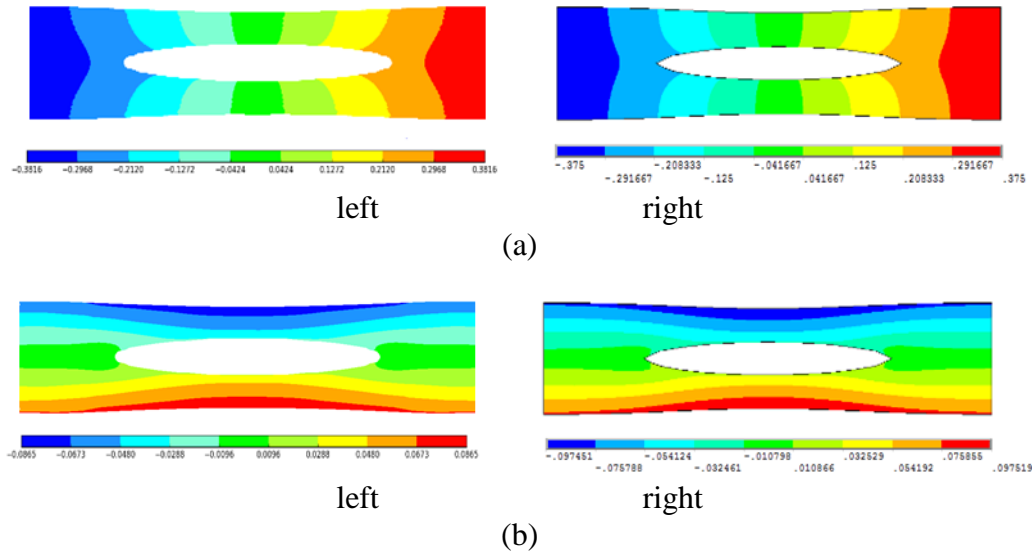
Figure 5.47. Displacement contours of membrane with a hole under uniaxial loading for $\lambda = 2.5$ in deformed configuration: (a) x- directions, and (b) y-direction. (left: peridynamic and right: ANSYS)

left — right

(a)

left — right

(b)

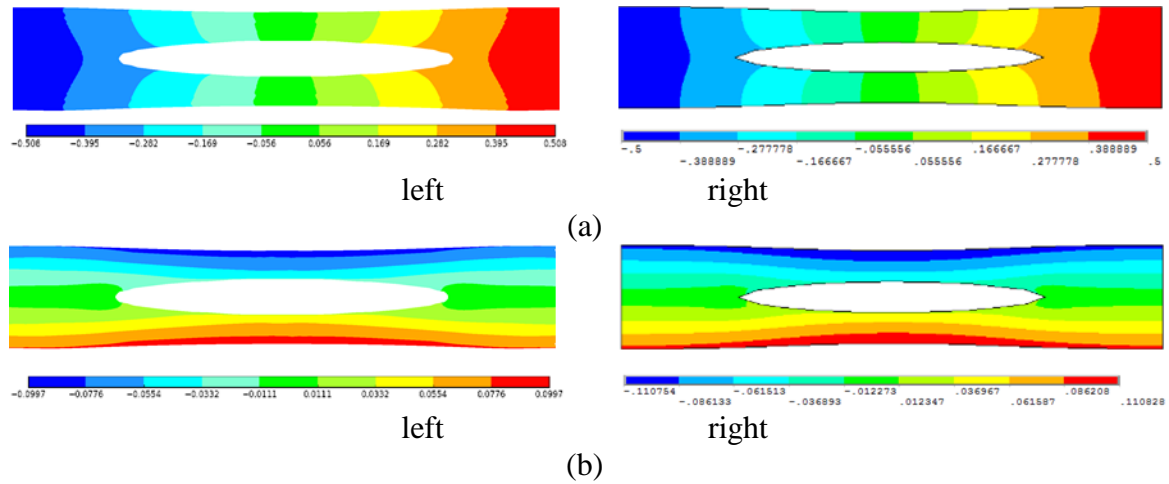**Figure 5.48.** Displacement contours of membrane with a hole under uniaxial loading for $\lambda = 3.0$ in deformed configuration: (a) x- directions, and (b) y-direction. (left: peridynamic and right: ANSYS)

5.3.2 Membrane with a Crack

The deformation contour plots are shown for each stretch values of $\lambda = 1.5$, 2.0, 2.5 and 3.0 in Fig. 5.51- 5.54. Similar to the deformation with a hole, the membrane increases in length, and decrease in width and thickness. As expected, the crack becomes circular in shape, and elliptical for increasing stretch values. As shown in Figs. 5.51 - 5.54, both PD and ANSYS predictions capture such deformation, and they are in good agreement.

Figure 5.49. Geometric and loading with a crack for uniaxial loading

Figure 5.50. Undeformed membrane with a crack

left   right

(a)

left   right

(b)
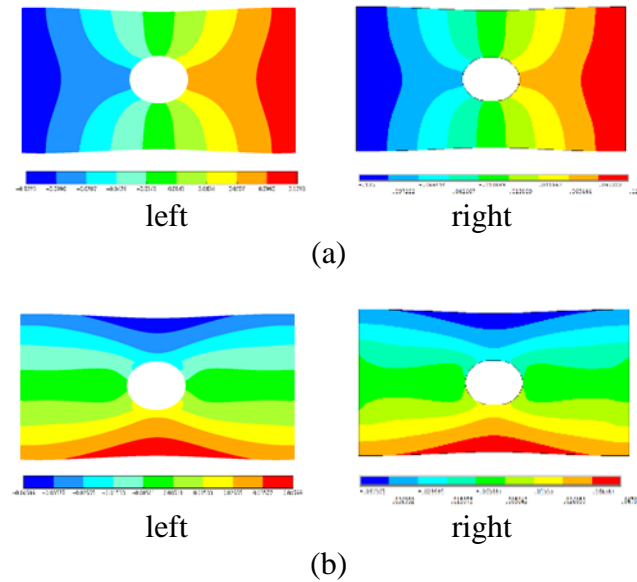
Figure 5.51. Displacement contours of membrane with a crack under uniaxial loading for $\lambda = 1.5$ in deformed configuration: (a) x- directions, and (b) y-direction. (left: peridynamic and right: ANSYS)
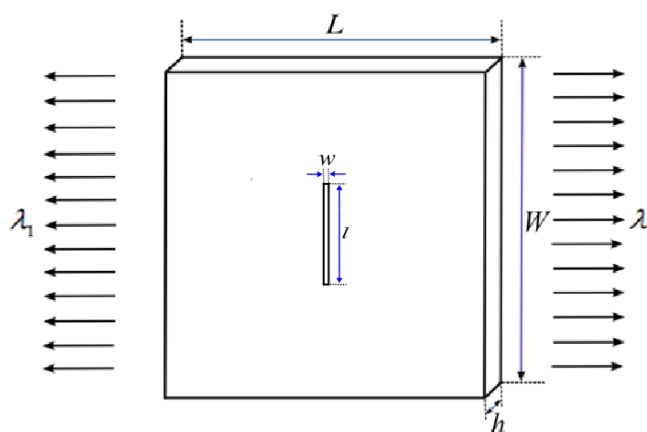

left   right

(a)

(b)
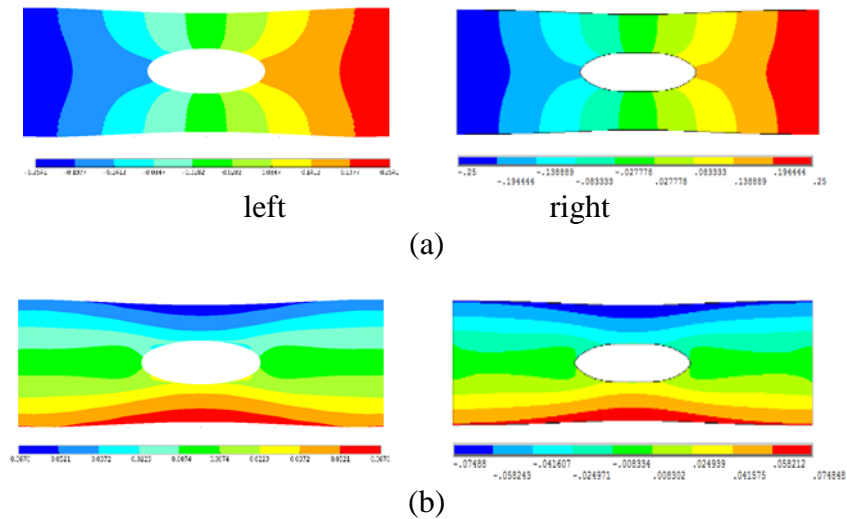
Figure 5.52. Displacement contours of membrane with a crack under uniaxial loading for $\lambda = 2.0$ in deformed configuration: (a) x- directions, and (b) y-direction. (left: peridynamic and right: ANSYS)
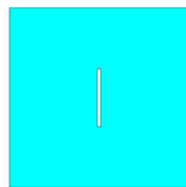
left　　　　　　right

(a)

(b)
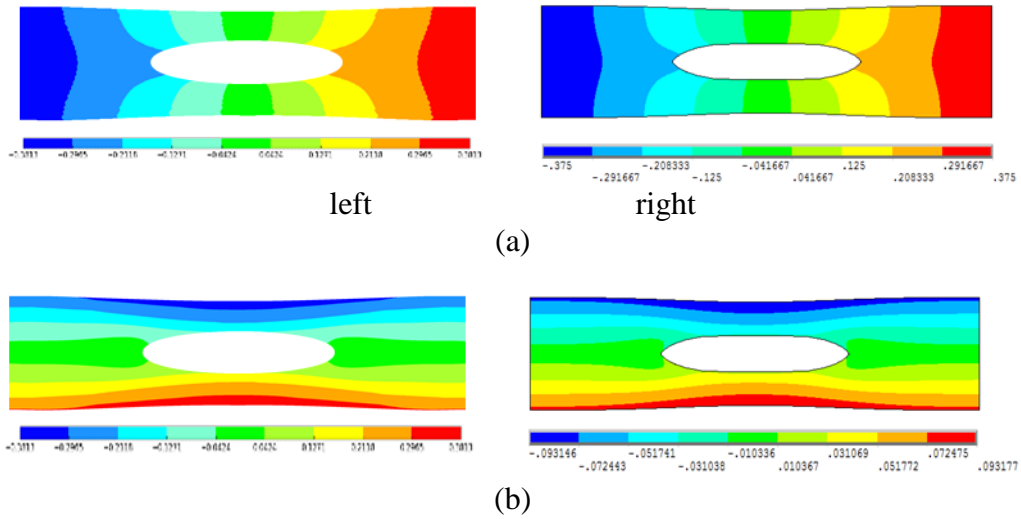
Figure 5.53. Displacement contours of membrane with a crack under uniaxial loading for $\lambda = 2.5$ in deformed configuration: (a) x- directions, and (b) y-direction. (left: peridynamic and right: ANSYS)

left　　　　　　right

(a)

(b)
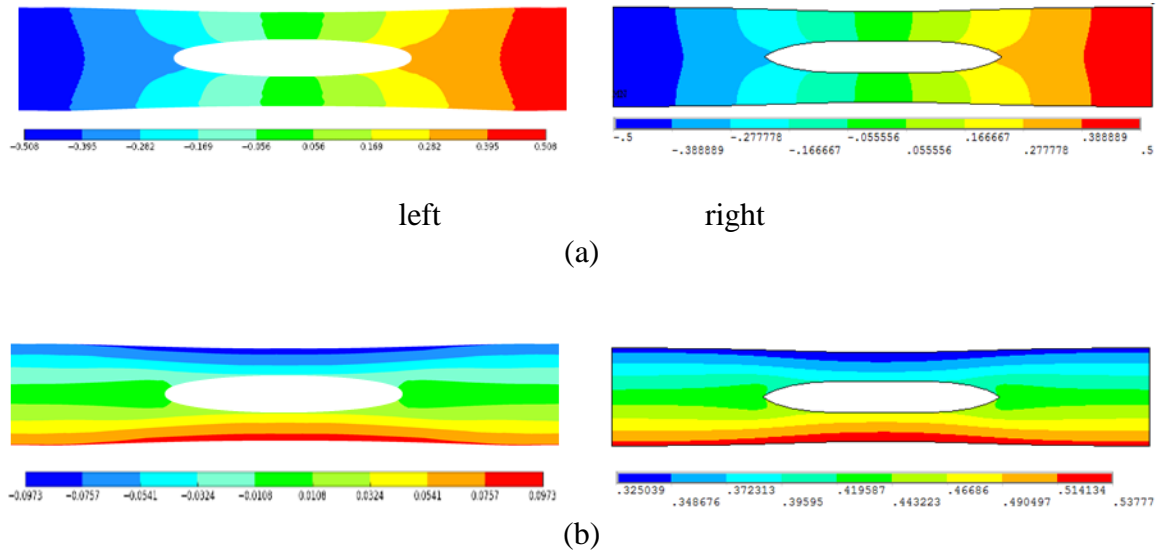
Figure 5.54. Displacement contours of membrane with a crack under uniaxial loading for $\lambda = 3.0$ in deformed configuration: (a) x- directions, and (b) y-direction. (left: peridynamic and right: ANSYS)

5.3.3 Membrane with a Solid Inclusion

The deformation contour plots are achieved for stretch values of $\lambda = 1.5,\ 2.0,\ 2.5$ and 3.0 as shown in Fig. 5.57 - 5.60. Similar to the previous cases of uniaxial loading, the length of the membrane elongates and the width and thickness contract. However, the membrane away from the edges contract more than the middle part due to the rigid inclusion. The comparison of PD and ANSYS prediction indicate good agreement, and captures the presence of the rigid inclusion.


Figure 5.55. Geometric and loading with a solid inclusion for uniaxial loading
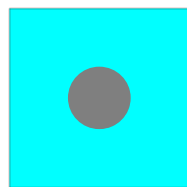
Figure 5.56. Undeformed membrane with a solid inclusion

left right

(a)

(b)
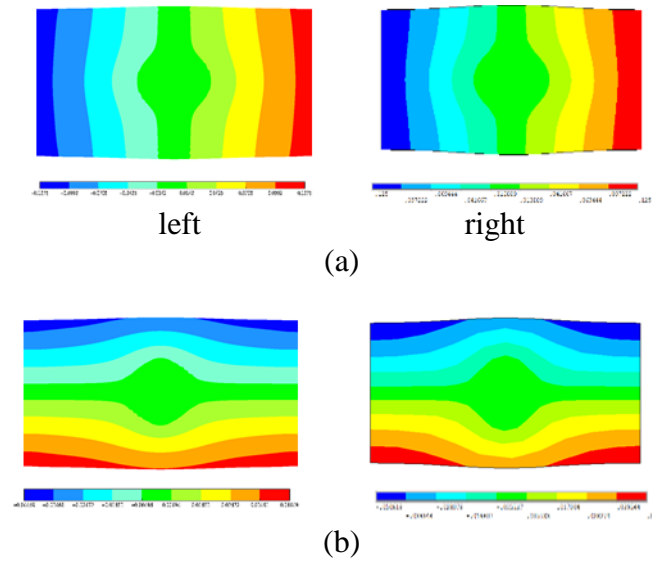
Figure 5.57. Displacement contours of membrane with a rigid inclusion under uniaxial loading for $\lambda = 1.5$ in deformed configuration: (a) x- directions, and (b) y-direction. (left: peridynamic and right: ANSYS)

left right

(a)

(b)
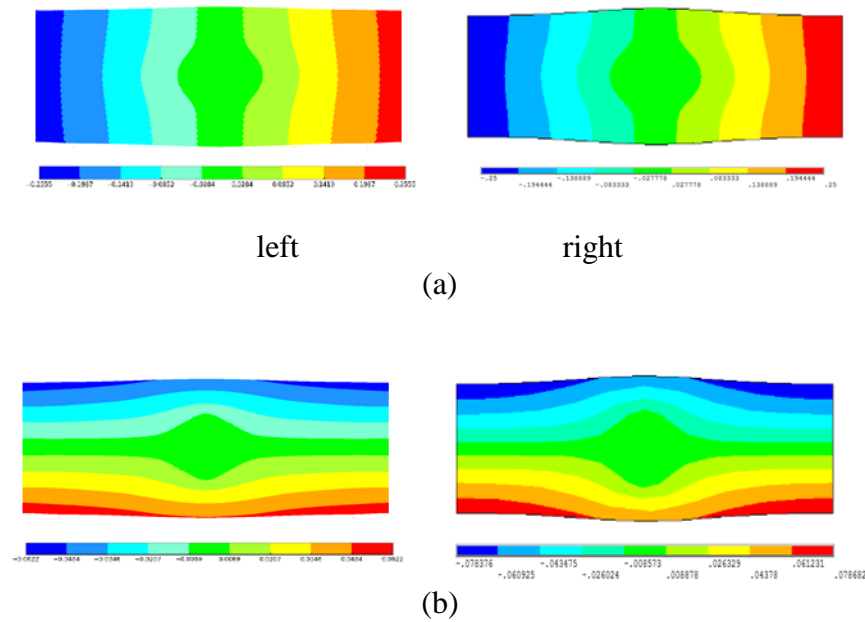
Figure 5.58. Displacement contours of membrane with a rigid inclusion under uniaxial loading for $\lambda = 2.0$ in deformed configuration: (a) x- directions, and (b) y-direction. (left: peridynamic and right: ANSYS)
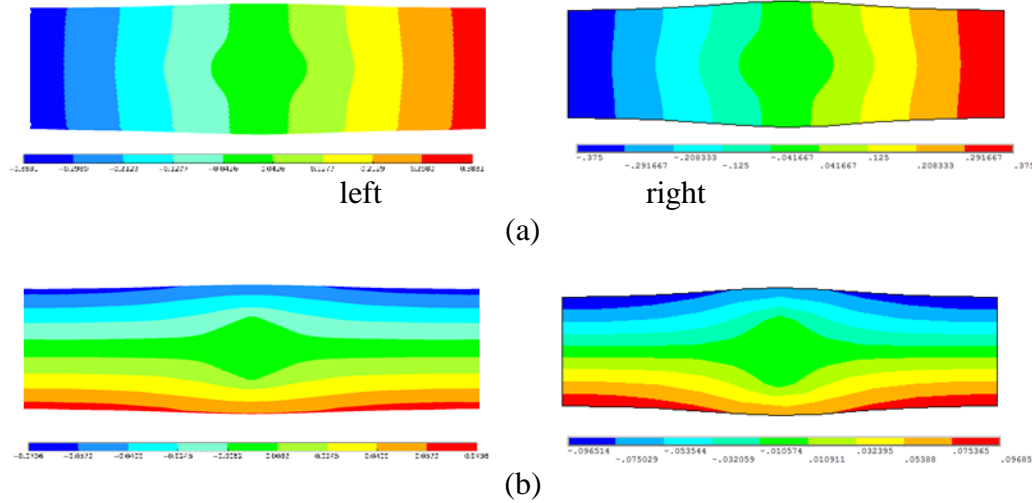
Figure 5.59. Displacement contours of membrane with a rigid inclusion under uniaxial loading for $\lambda = 2.5$ in deformed configuration: (a) x- directions, and (b) y-direction. (left: peridynamic and right: ANSYS)
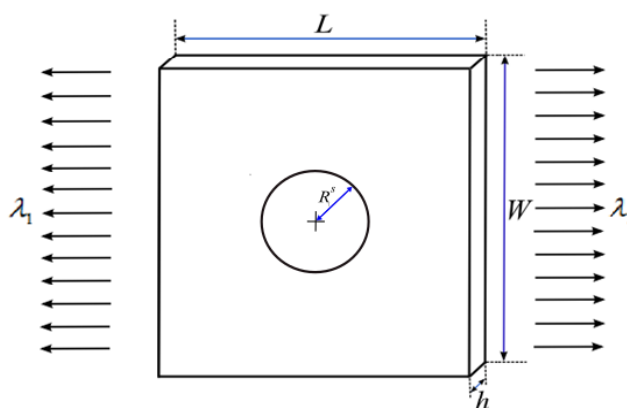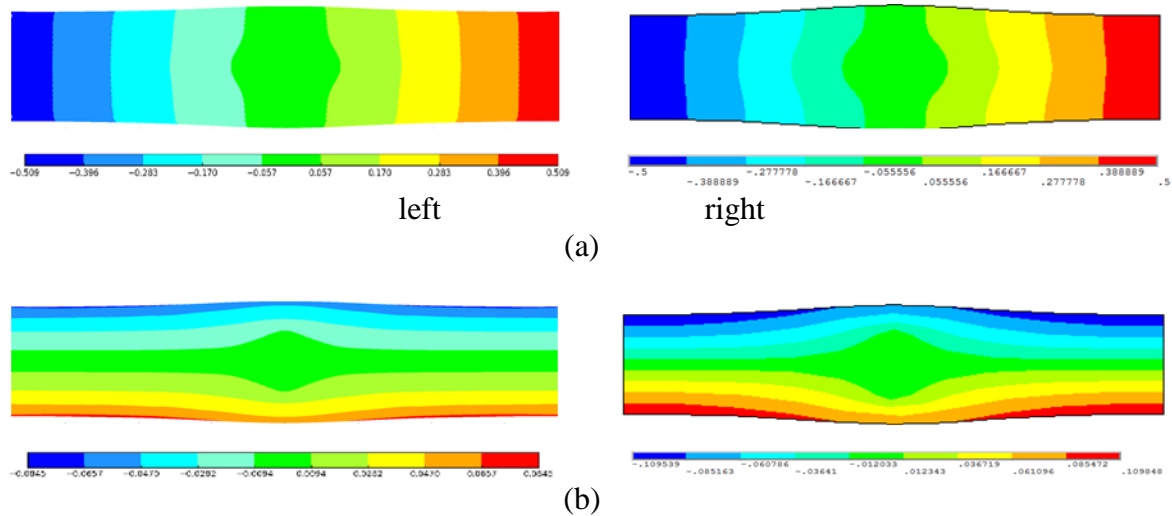

Figure 5.60. Displacement contours of membrane with a rigid inclusion under uniaxial loading for $\lambda = 3.0$ in deformed configuration: (a) x- directions, and (b) y-direction. (left: peridynamic and right: ANSYS)

As part of a convergence rate study, the discretizations of (200x200), (150x150), (100x100) and (50x50) are considered for equibiaxial, planar and uniaxial loading cases. However, the resulting force for each loading case, and the deformed shapes with defects are almost

identical for each discretization. Therefore, the selection of the number of material points is only dependent upon the computational time. In the equibiaxial and planar loading, only elongation occurs, and the horizon size, $\delta = 3.015\Delta x$ is sufficient. In the uniaxial loading, both elongation and contraction occur simultaneously, and the horizon size of $\delta = 9.015\Delta x$ is necessary. However, it causes longer computational time; for this reason, the small number of material points, (50x50) is selected for uniaxial loading, and 100 by 100 is selected for equibiaxial and planar loading. On the other hand, in FE models, (40x40), (50x50) and (15x15) are used as number of nodes for equibiaxial, planar and uniaxial loadings, respectively. There are two reasons for these selections. First, the finite element solution does not converge in the presence of a crack with any discretization. Hence, the acceptable discretization is established for convergence while considering the computational time.

6. SUMMARY AND FUTURE WORK

One of the major contributions of this study is to develop the bond-based peridynamic constitutive relations for modeling rubbery materials. It specifically concerns Neo-Hookean type membrane under equibiaxial, planar and uniaxial loading conditions. The Neo-Hookean material model has one independent constant. The strain energy density function is expressed in terms of the principal stretches, $\lambda_1, \lambda_2, \lambda_3$ while satisfying the incompressibility condition. The material parameters for each loading are determined by equating the peridynamic strain energy to those of the classical continuum mechanics. Also, the surface correction is performed by comparing the PD strain energy density with

that of the classical continuum mechanics. After determining the explicit form of the strain energy density function for each loading condition, the PD equation of motion is constructed in general form in terms of the force density vector. PD equation of motion is based on the Neo-Hookean model. The numerical results concerning the deformation without and with defects, a hole, crack and a rigid inclusion are verified by comparing them with ANSYS prediction.

The solutions of the PD equation of motion subject to the specified the boundary conditions are achieved by using techniques already available the literature such as the adaptive dynamic relaxation. The numerical results concern primarily verification of the PD force density – stretch relations for each loading case. The PD numerical predictions for deformation without and with defects in the form of a hole, crack and a rigid inclusion are compared with ANSYS predictions for all loading cases.

As a future work, crack growth behavior can be investigated under equibiaxial, planar and uniaxial loading conditions. Also, this approach can be extended to construct the strain energy density function for Neo-Hookean type rubbery material under three dimensional loading conditions.

REFERENCES

[1] Mooney M (1940) A theory of large elastic deformation. *Journal of Applied Physics* Vol. 11, pp. 582-592

[2] Rivlin RS (1948) Large elastic deformations of isotropic materials: I. Fundamental concepts. II. Some uniqueness theorem for pure homogeneous deformation. *Philosophical Transactions of the Royal Society of London. Series A* Vol. 240, pp. 459-508

[3] Treloar LRG (1943) *Trans. Faraday Soc* Vol. 39, pp. 241

[4] Ogden RW (1972) Large deformation isotropic elasticity - On the correlation of theory and experiment for incompressible rubberlike solids. *Proceedings of the Royal Society of London. Series A* Vol. 326, pp. 565-584

[5] Yeoh OH (1993) Some forms of strain energy function for rubber. *Rubber Chemistry and Technology* Vol. 66, pp. 754-771

[6] Boyce MC, Arruda EM (2000) Constitutive models of rubber elasticity: A review. *Rubber Chemistry and Technology* Vol. 81, pp. 837-848

[7] Gent AN (1996) A new constitutive relation for rubber. *Rubber Chemistry and Technology* Vol. 69, pp. 59-61

[8] Amin AFMS, Alam MS, Okui Y (2002) An improved hyperelasticity relation in odeling visco-elasticity response of natural and high damping rubbers in compression: Experiments, parameter identification and numerical verification. *Mechanics of Materials* Vol. 34, pp. 75-95

[9] Podnos E, Becker E, Klawitter J, Strzepa P (2006) FEA analysis of silicone MCP implant. *Journal of Biomechanics* Vol. 39, pp. 1217-1226

[10] Montella G, Calabrese A, Serino G (2014) Mechanical characterization of a tire derived material: Experiments, hyperelastic modeling and numerical validation. *Construction and Building Materials* Vol. 66, pp. 336-347

[11] Duncan BC, Crocker LE, Urquhart JM (2000) Evaluation of hyperelastic finite element models for flexible adhesive joints. *National Physical Laboratory*

[12] Vavourakis V, Kazakidi A, Tsakiris D, Ekaterinaris J (2011) A finite element method for nonlinear hyperelasticity applied for the simulation of octopus arm motions. *The fourth International Conference on computational Methods for Coupled Problems in Science and Engineering.*

[13] Gagnon M, Hubert P, Semler C, Païdoussis M, Vézina M, Lavoie D (2006) Hyperelastic modeling of rubber in commercial finite element software (ANSYSTM), *McGill University, Department of Mechanical Engineering*

[14] Samad MSA, Aidy Ali, Sidhu RS (2011) Durability of automotive jounce bumper. *Materials and Design* Vol. 32, pp. 1001-1005

[15] Ramachandran T, Padmanaban KP, Nesamani P (2012) Modeling and analysis of IC engine rubber mount using finite element method and RSM. *Procedia Engineering* Vol. 38, pp. 1683-1692

[16] Guo Z, Sluys LJ (2008) Constitutive modelling of hyperelastic rubber-like materials. Heron Vol. 53, pp. 109-132

[17] Kyriacou SK, Schwab C, Humphrey JD (1996) Finite element analysis of nonlinear orthotropic hyperelastic membranes. *Computational Mechanics* Vol. 18, pp. 269-278

[18] Daly S, Prendergast PJ, Dolan F, Lee TC (2000) Use of finite element analysis to simulate the hyperelastic behavior of cardiovascular tissue. *Proceedings of the 12th Conference of the European Society of Biomechanics*, Dublin, Royal Academy of Medicine in Ireland, 252.

[19] Dolbow J, Moes N, Belytschko T (2001) An extended finite element method for modeling crack growth with frictional contact. *Computer Methods in Applied Mechanics and Engineering* Vol. 190, pp. 6825-6846

[20] Karoui A, Mansouri K, Renard Y, Arfaoui M (2014) The extended finite element method for cracked hyperelastic materials: a convergence study. *International Journal for Numerical Methods in Engineering* Vol. 100, pp. 222-242

[21] Melenk JM, Babuska I (1996) The partition of unity finite element method: Basic theory and applications. *Computer Methods in Applied Mechanics and Engineering* Vol. 139, pp. 289-314

[22] Liu WK, Chang H, Chen JS, Belytschko T, Zhang YF (1988) Arbitrary Lagrangian-Eulerian Petrov–Galerkin finite elements for nonlinear continua. *Computer Methods in Applied Mechanics and Engineering* Vol. 68, pp. 259-310

[23] Khoei AR, Azami AR, Anahid M, Lewis RW (2006) A three-invariant hardening plasticity for numerical simulation of powder forming processes via the arbitrary Lagrangian-Eulerian FE model. *International Journal for Numerical Methods in Engineering* Vol. 66, pp. 843-877

[24] Rodriguez-Ferran A, Casadei F, Huerta A (1998) ALE stress update for transient and quasistatic processes. *International Journal for Numerical Methods in Engineering* Vol. 43, pp. 241-262

[25] Yamada T, Kikuchi F (1993) An arbitrary Lagrangian-Eulerian finite element method for incompressible hyperelasticity. *Computer Methods in Applied Mechanics and Engineering* Vol. 102, pp. 149-177

[26] Bayoumi HN, Gadala MS (2004) A complete finite element treatment for the fully coupled implicit ALE formulation. *Computational Mechanics* Vol. 33, pp. 435-452

[27] Gu YT, Wang QX, Lam KY (2007) A meshless local Kriging method for large deformation analyses. *Computer Methods in Applied Mechanics and Engineering* Vol. 196, pp. 1673-1684

[28] Hardee E, Chang KH, Grindeanu I, Yoon S, Kaneko M, Chen JS (1999) A Structural Nonlinear Analysis Workspace (SNAW) based on meshless methods. *Advances in Engineering Software* Vol. 30, pp. 153-175

[29] Grindeanu I, Choi KK, Chen JS (1999) Shape design optimization of hyperelastic structures using a meshless method. *The American institute of aeronautics and astronautics* Vol. 37, pp. 990-997

[30] Choi KK, Santos JLT (1987) Design sensitivity analysis of nonlinear structural systems Part I: Theory. *International Journal for Numerical Methods in Engineering*. Vol. 24, pp. 2039–2055

[31] Tanner C, Carter T, Hawkes D (2006) 3D rezoning for finite element modelling of large breast deformations. *In Proceedings of European modelling symposium*. pp. 51-53

[32] Watari R, Hashimoto G, Okuda H (2013) mesh coarsening method based on multi-point constraints for large deformation finite element analysis of almost incompressible hyperelastic material. *International Conference on Simulation Technology*

[33] Trapper P, Volokh KY (2008) Cracks in rubber. *International Journal of Solids and Structures* Vol. 45, pp. 6034-6044

[34] Mediavilla J, Peerlings RHJ, Geers MGD (2006) A robust and consistent remeshing-transfer operator for ductile fracture simulations. *Computers and Structures* Vol. 84, pp. 604-623

[35] Bouchard PO, Bay F, Chastel Y, Tovena I (2000) Crack propagation modelling using an advanced remeshing technique. *Journal of Applied Mechanical Engineering* Vol. 189, pp. 723-742

[36] Rashid M, The arbitrary local mesh replacement method: An alternative to remeshing for crack propagation analysis (1998). *Computer Methods in Applied Mechanics and Engineering* Vol. 154, pp. 133-150

[37] Silling SA (2000) Reformulation of elasticity theory for discontinuities and long-range forces. *Journal of the Mechanics and Physics of Solids* Vol. 48, pp. 175-209

[38] Silling SA, Epton M, Weckner O, Xu J, Askari E (2007) Peridynamic states and constitutive modeling. *Journal of Elasticity* Vol. 88, pp. 151-184

[39] Silling SA, Bobaru F (2005) Peridynamic modeling of membranes and fibers. *International Journal of Non-Linear Mechanics* Vol. 40, pp. 395-409

[40] Oterkus E, Madenci E (2014) Peridynamic theory and its applications. New York, Springer.

[41] Kilic B, Madenci E (2010) An adaptive dynamic relaxation method for quasi-static simulations using the peridynamic theory. *Theoretical and Applied Fracture Mechechanics* Vol. 53, pp. 194-201

[42] Silling SA, Askari E (2005) A meshfree method based on the peridynamic model of solid mechanics. *Computers & Structures* Vol. 83, pp. 1526-1535

[43] Underwood P (1983) Dynamic relaxation. Computational Methods for Transient Analysis, pp. 245-265

[44] Lovie TG, Metzger DR (1999) Lumped mass tensor formulation for dynamic relaxation. *In:Hulbert GM (ed) Computer Technology, ASME. Boston* Vol. 385, pp. 255-260

[45] Suave RG, Metzger DR (1995) Advances in dynamic relaxation techniques for nonlinear finite element analysis. *Journal of Pressure Vessel Technology* Vol. 117, pp. 170-176

[46] Macek RW, Silling SA (2007) Peridynamics via finite element analysis. *Finite Element in Analysis and Design* Vol. 43, pp. 1169-1178

[47] Madenci E, Oterkus S (2016) Ordinary state-based peridynamics for plastic deformation according to von Mises Yield Criteria with isotropic hardening. *Journal of the Mechanics and Physics of Solids* Vol. 86, pp. 192-219